University of Leoben

Dissertation

Investigation of Residual Stress Profiles and Fracture Properties of Thin Films

Stefan Massl

Leoben, July 2008

This work was financially supported by the Austrian Science Fund (FWF) through project AP26043501.

Erich Schmid Institute of Materials Science
Austrian Academy of Sciences
Jahnstrasse 12
A-8700 Leoben
http://www.oeaw.ac.at/esi

This doctoral thesis was typeset by the use of KOMA-Script and LaTeX 2_ε.
The template was modified by Dr. Weinhandl and Dr. Vorhauer.

To my family

Affidavit

I declare in lieu and oath, that I wrote this thesis and performed the associated research myself, using only literature cited in this volume.

Leoben, July 2008

Acknowledgements

I would like to thank a number of persons who made this doctoral thesis possible, inspired my work and supported me during the last three years.

First of all, I would like to express my gratitude to my supervisor Reinhard Pippan and my project leader Jozef Keckes for giving me the opportunity to work in this interesting field, for their guidance and the numerous interesting discussions. I want to thank especially Reinhard for his incredible talent to motivate me when the experiments did not work as I hoped.

Thanks to my friends and colleagues from the Erich Schmid Institute for their support, helpfulness and the interesting scientific and non-scientific discussions. Special thanks to Griselda Guidoni, Peter Gruber, Walther Heinz, Christoph Kirchlechner, Klaus Jürgen Martinschitz, Martin Rester, Stephan Scheriau and Wolfgang Philipp Thomma. Furthermore, I want to mention the outstanding friendly and productive atmosphere at this institute, which is not least because of Gerhard Dehm, the head of the Department Materials Physics and the Erich Schmid Institute.

Last but not least I want to give my special thanks to my parents and my sister for supporting me under all circumstances.

Abstract

A method for the determination of residual stress distributions in near-surface structures and a technique for evaluating the fracture properties of thin films are developed.

The new technique for the determination of residual stress profiles called ion beam layer removal method (ILR method) is based on the fabrication of a micro-cantilever and the subsequent gradual reduction of the film thickness using a focused ion beam workstation (FIB). The deflection as a function of film thickness is used as a basis for the calculation of the stress distribution in the thin film. The method is presented by investigating the depth profile of residual stresses in a $840nm$ thick Ni film deposited on (100) Si. The result shows an in-plane stress in the Ni film growing continuously from $169 \pm 37MPa$ at the surface to $792 \pm 103MPa$ at the interface. The mean stress of $460 \pm 60MPa$ is compared with the result obtained by means of the wafer curvature method, which leads to an average stress of $(581 \pm 58MPa)$. The method developed can be applied to crystalline as well as amorphous materials and features a depth resolution on a nanoscale.

The influence of experimental errors and parameters is investigated by means of a $1.16\mu m$ thick TiN film on (100) Si and four model stress distributions representing four types of depth profiles of residual stresses. The statistical errors are described by the normal distribution, which allows a detailed analysis of the interactions between the individual errors. The most important measures to assure small errors are the choice of adequate cantilever substrate thicknesses to avoid fracture or plastic deformation and the gradual reduction of the film thickness in small steps in order to reproduce the stress profiles well.

A further development of the ILR method is the 3D-ILR method, which allows the determination of spatial stress profiles in near-surface structures. This technique is presented by investigating the lateral and depth distribution of residual stresses in and around the plastic zone induced by a scratch with a ball-shaped indenter in a $840nm$ thick Ni film on (100) Si. The result shows that the stress profile changes significantly with the lateral position. Far away from the plastic zone, the Ni film exhibits residual stresses growing from $169 \pm 37MPa$ at the surface to $792 \pm 103MPa$ at the interface and an average stress of $460 \pm 60MPa$. This gradient decreases with decreasing distance from the centre of the scratch. Directly in the centre of the plastic zone, no stress gradient is observed and a mean stress of $-478 \pm 91MPa$ is determined. As shown in this example, 3D-ILR method features a depth resolution on a nanoscale and a lateral resolution in the micron range.

Abstract

The method used for the determination of fracture properties of thin films is based on the determination of the depth profile of residual stresses followed by the fabrication of a microcantilever by means of a FIB workstation and the subsequent testing with an in-situ cube corner indenter. The strength and mode I fracture toughness are evaluated by superimposing the residual stresses and the stresses induced by the loading. The investigations of a magnetron-sputtered $1.1\mu m$ thick TiN film shows a fracture toughness of $2.8 \pm 0.3 MPa\sqrt{m}$ and a fracture strength of $4.4 \pm 0.7 GPa$. SEM-images of the fracture surface reveal that the crack propagates mainly along the grain boundaries, which leads to the conclusion that besides compressive residual stresses, the high grain boundary strength contributes significantly to structural integrity of such coated systems.

Non quia difficilia sunt non audemus, sed quia non audemus difficilia sunt.

It is not because things are difficult that we do not dare; it is because we do not dare that they are difficult.

Lucius Annaeus Seneca (4 B.C. – 65 A.D.)

Contents

1 Introduction

1.1 Why Coatings?

Surfaces of mechanical components and devices are often exposed to enviromental influences like heat, wear, or corrosion, and they interact with electrical and magnetic fields, for example. In many cases, the desired properties of the surface are different to the properties of the bulk material like hardness and fracture toughness, corrosion resistance and low material costs.

This problem can be solved by choosing an adequate coating in order to achieve the desired surface properties. A classical example for coated substrates are cutting tools, which usually consist of a softer metal core for the required toughness and a hard ceramic coating for wear resistance.[19] Sometimes, interlayers are used to enhance the adhesion between the substrate and the coating or to decrease possible gradients of material properties. Soft coatings are often used to provide corrosion resistance of the bulk material or effective lifetime lubrication of rolling bearings, for example.[18]

According to literature, films or coatings, respectively, are divided into thin and thick films. This classification does not depend on the geometrical thickness of the film as the denomination suggests, although sometimes the value of $1\mu m$ is mentioned. In fact, the change from thick to thin films is characterized by significant changes in the material properties and microstructures. While thick films have similar properties to the corresponding bulk materials, thin films show a very different behavior, which can be deduced from the increasing surfact-to-volume ratio and the fine microstructure that affects the mechanical properties.[19] High hardnesses for wear resistant coatings, for example, can be achieved by high defect densities and submicron or nanocrystalline grain sizes, which depend on the production process and the deposition parameters. Owing to the importance of the fabrication processes, first a short overview is given and then the two most important techniques – physical vapor deposition and chemical vapor deposition – are described briefly.

1.2 Fabrication Processes of Thin Films

In general, fabrication methods of thin films can be divided into wet processes and dry processes.

Wet processes are characterized by the growth of the coating in a liquid solution. Popular examples are electroplating and anodic oxidation, which make use of electrolytic processes, and sol-gel deposition methods, where chemical reactions first lead to colloidal particles (sol) and then to an inorganic continuous network containing a liquid phase (gel), which has to be dried and sintered in order to obtain a solid film.

Here we want to focus on dry processes. The two most important representatives are the chemical vapor deposition (CVD) and the physical vapor deposition (PVD), which will be discussed in detail.[35]

Chemical vapor deposition is used to produce solid layered structures on substrates for the semiconductor industry or for cutting tools. Here, one or more gaseous precursors react usually at high temperatures on the substrate surface to produce a nonvotatile solid that deposits atomistically on the substrate (Fig.1.1). The remaining exhaust gases are often acidic or toxic and therefore have to be collected and neutralized.

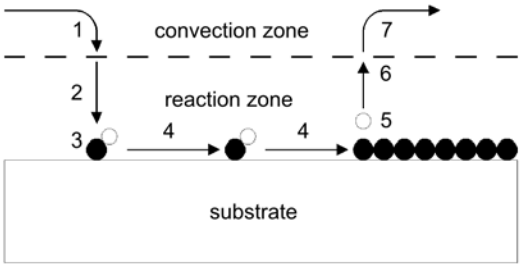

Figure 1.1: Schematic description of the formation of the thin film in a typical CVD process: transportation of the precursors through the convection zone by forced convection (1). Diffusion of the reactants through the reaction zone to the substrate surface (2). Adsorption of the precursors on the substrate (3). Formation of the thin film by reaction of the precursors at the surface and production of byproducts (4). Diffusion of the byproducts through the reaction zone (5). Removal of the byproducts by forced convection (6).[36]

A typical example for a chemical reaction of a CVD process is the deposition of Titanium Nitride from Titaniumchloride, Hydrogen and Nitrogen (Eq. (1.1)). The chemical reaction for the neutralization of the acidic exhaust gas is described in Eq. (1.2).

$$4H_2 + 2TiCl_4 + N_2 \rightarrow 2TiN + 8HCl \tag{1.1}$$

$$HCl + NaOH \rightarrow NaCl + H_2O \tag{1.2}$$

A number of CVD processes has been developed to account for different thin film-substrate systems and desired film properties. CVD processes can be classified according to the precursor used, the process pressure, or the type of heating source. Some examples of popular types of CVD processes are

- conventional (thermal) CVD, which is operated between $800°C$ and $1200°C$ and is usually used for mass products like coated tungsten carbides.
- MOCVD (Metal-Organic CVD), where metal-organic precursors are used and low temperatures can be achieved.
- LPCVD (low pressure CVD), which is widely used in semiconductor device processing and allows high deposition rates, improved uniformity of the film thickness and the possibility of coating large numbers of wafers at a time.[37] A schematic description of a typical LPCVD process is depicted in Fig.1.2.
- PACVD (Plasma Assisted CVD), which is often used for coating high speed steels and allows low process temperatures owing to plasma-supported chemical reactions.

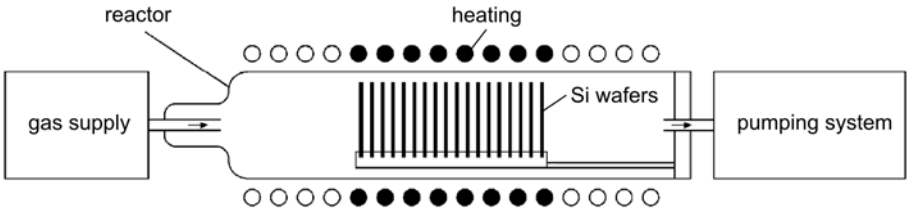

Figure 1.2: Schematic description of a LPCVD process. This process allows large output, excellent film quality and is mainly used for semiconductor device fabrication.[36]

CVD-produced films are used in many applications like semiconductor devices, tribological coatings, insulating thin films, decorative and optical films, for example. Owing to the nondirectional deposition procedure, CVD techniques are capable of depositing thin films of homogeneous thicknesses even on three dimensional concave substrates. On the other hand, the deposition temperatures are usually relatively high, which leads to large thermal stresses at room temperature. Furthermore, it is essential to control the process parameters exactly in order to assure the desired chemical reactions and as a result constant coating qualities.

Physical vapor deposition is a process in which the film is fabricated by condensing the coating material from the gas phase in an evacuated chamber. Here, the substrate and the target are located in an evacuated chamber. The target material is evaporated by means of laser light, accelerated ions or electric arcs and moves towards the substrate where it condensates and forms the thin film.

PVD processes can be divided into three steps. First, the target material is transformed from a condensed phase to vapor. Then, the vapor moves from the target towards the substrate. In case of reactive PVD, the vaporized target material reacts chemically with a reactive gas in order to obtain the desired composition. Finally, the material condensates on the substrate surface and the film grows.

The PVD processes can be classified according to the method the target material is transformed from the condensed into the vapor phase:

- Sputtering is a process in which predominantly atoms are ejected from the solid target material as a result of bias voltage-accelerated ions of the working gas plasma

that impinge on the target surface. Depending on the nature of the voltage, the sputtering processes are divided into direct current (DC) sputtering, radio frequency (RF) sputtering, and magnetron sputtering. In case of using gases like N_2, O_2 or CO_2 to react chemically with the atomized target material, the process is called reactive sputtering. An example of a reactive RF-PVD process is depicted in Fig.1.3.

- Another way of ejecting atoms from the target is evaporation. Techniques like thermal evaporation, electron beam evaporation, pulsed laser evaporation, or arc evaporation are often used for the production of thermal barrier coatings.
- Ion plating is a combination of sputtering and evaporation processes.

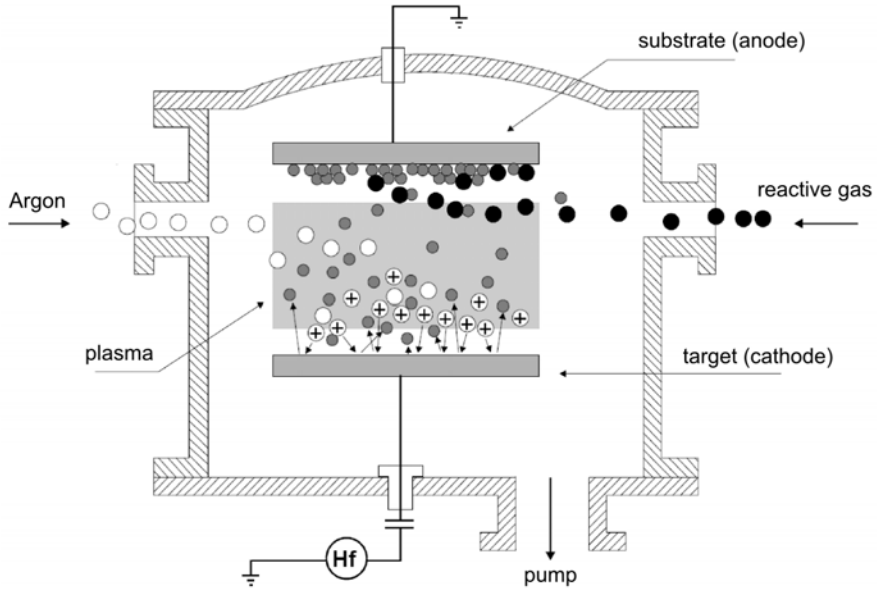

Figure 1.3: Schematic description of a reactive radio frequency (RF) sputtering process. When the voltage at the target is negative, the Ar^+ ions of the plasma (white) are accelerated towards the target, impinge on the surface and eject atoms (grey) from the target. Owing to the kinetic energy obtained from the sputtering process, these atoms cross the plasma, react with the reactive gas (black) and adhere on the substrate surface where they form the thin film. In contrast to direct current (DC) sputtering, RF sputtering can be used with non-conductive targets.[36]

PVD-fabricated thin films are used mainly for cutting tools, microelectronic devices and packagings. Compared with CVD, PVD is more flexible because it allows to adjust the sputtering rates and to deposit a large number of different materials. The PVD process is easier to model and it is not necessary to maintain a complicated equilibrium of chemical reactions to obtain high quality coatings. Yet, the directional impact of the target atoms on the substrate surface leads to shadowing effects at edges which causes problems when films of homogeneous thicknesses are deposited on uneven surfaces.

What all processes have in common is the evolution of more or less pronounced residual stresses. The origin of such stresses as well as the importance for thin films and coated

components are discussed subsequently.

1.3 Origin of Residual Stresses

Residual stresses can be required for proper functioning of the component, but can also lead to fracture or delamination. Compressive stresses will reduce the risk of tensile failure and increase the risk of buckling, whereas tensile stress will have the opposite effect.[18] Hard coatings with good interfacial adhesion are usually subjected to compressive stresses, which prevents cracks from nucleating and propagating.

Residual stresses can be classified into internal and external residual stresses. Here, the intrinsic stresses -also called growth stresses- and two of the most important external stresses -thermal and deformation induced stresses- are discussed. Furthermore, the evolution of surface-near stresses induced by ion implantation is reviewed briefly.

1.3.1 Growth Stresses

Coatings exhibit internal residual stress owing to the growth process of the film on the substrate. Stresses in epitaxial films arise usually as a result of the constraint of the substrate on the film material dictated by the requirement of coherency.[1] Here, we want to focus on the growth stresses in polycrystalline thin films because this kind of films is investigated in this thesis.

For most film-substrate material combinations, films grow non-epitaxially in the Volmer-Weber mode, which leads to a polycrystalline microstructure. Although the connection between film growth, stress and microstructure is not yet fully understood, the growth of polycrystalline films at deposition temperature can be classified into a sequence of stages, and some general trends in behaviour can be identified[1] (Fig.1.4).

In stage 1, the material deposited forms discrete clusters or islands on the substrate surface. These islands are usually subjected to compressive stress, which is attributed to the action of surface and/or interface stress that reduces the lattice spacing in a very small isolated crystallite compared with the spacing in a bulk crystal of the same material. In stage 2, island growth leads to island-to-island contact and the formation of grain boundaries, which is the cause of tensile stress that arises in the film. An interesting approach introduced by Nix and Clemens[3] describes the island coalescence as a reverse elastic fracture mechanism in which the grain boundary is considered as a crack; the system can lower its free energy by closing this crack and replacing the high surface energy by the lower interfacial energy. By closing up the crack or grain boundary, respectively, the film material is subjected to tensile stresses, which most of the material accommodates elastically. In stage 3, the growth stress in polycrystalline materials decreases, which often leads to compressive film stress at deposition temperature that cannot be explained merely by relaxation of tensile stresses. A possible explanation for this experimentally observed change from tensile to compressive stresses with increasing film thickness is the migration of surface atoms into the grain boundaries. Investigations have shown that only a small number of excess atoms is necessary to induce such compressive stresses.[1,4]

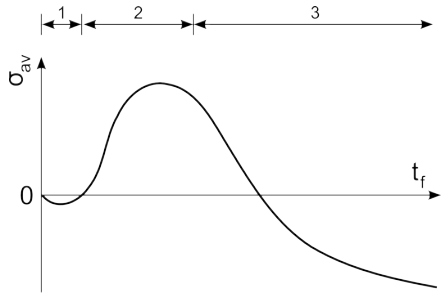

Figure 1.4: Typical evolution of average film stress σ_{av} as a function of film thickness t_f during the deposition procedure. The curve describes the three stages of film growth (compressive - tensile - compressive stress) for vapor deposited polycrystalline films at deposition temperature. In-situ monitoring of the average stresses during deposition shows that the film thickness at which the change from tensile to compressive stresses occurs (between stages 2 and 3) depends strongly on the materials involved and can lie between a few nanometers and a few hundred nanometers.[1]

It has to be emphasised that this curve describes the average film stresses at deposition temperature and that the stresses at room temperature are superimposed by the thermal stresses that arise owing to the difference of the coefficients of thermal expansion of the substrate and the coating.

1.3.2 Thermal Stresses

Thermal stress is an important issue in coated and uncoated components and can arise during fabrication and in service. Components or semi-finished parts are usually fabricated at elevated temperatures to obtain the desired material properties or simply because it is required by the fabrication process. In terms of massive parts, residual stresses can be introduced when cooling the material with a high cooling rate, which can produce stresses as high as the yield stress between the shell and the core, especially if the material exhibits a low yield strength and a low thermal conductivity. This effect can be amplified or weakened when the material undergoes one or more phase transformations during this treatment.[10]

Regarding coated components, it does not require high heating or cooling rates to produce thermal residual stresses because often the coating and the substrate material exhibit different coefficients of thermal expansion (CTE). Depending on the relative magnitude of the CTEs and the corresponding Young's moduli, such stresses can reach the yield stress of the film, which can lead to fracture in case of tensile stresses in the coating or delamination of the coating from the substrate material in case of high compressive stresses and insufficient adhesion. An estimation of the order of magnitude of thermal stresses is demonstrated by means of a simple example. We consider a cutting tool consisting of a 2μm thick CrN film deposited on a steel substrate by means of a conventional CVD process at a typical deposition temperature of $800°C$. The thermal stresses in the coating induced by cooling down the system to room temperature reach about 3GPa compression according to the difference in the CTEs of steel ($\approx 13 \cdot 10^{-6} K^{-1}$)[16] and CrN ($6 \cdot 10^{-6} K^{-1}$).[17]

1.3.3 Friction and Wear

Friction arises when two surfaces are brought into contact and are then moved relatively to each other. In the initial stage, the approach of the surfaces leads to plastic deformation of the asperities, which results in an increase of the contact area. The approach ends when the contact area has grown to a sufficient size to support the load elastically. In sliding contact, the frictional energy is dissipated mainly by breaking interfacial bonds and plastic deformation.[18] Besides the mode of deformation, friction depends on the hardnesses and the elastic moduli of the asperities of the surfaces.

Friction-induced surface-near residual stresses in uncoated components arise during machining of the surface, for example. Depending on the material, the machining process, the lubrication and the condition of the working tool, the residual stresses can be compressive, tensile or a mixture of both.[10] Uncoated components, which have to sustain friction, are usually surface-modified in order to enhance the friction resistance of the surface. This modification is often provided by coating the component with a wear-resistant thin film that improves the tribological properties. Depending on the film thickness, the properties are determined either mainly by the coating (in case of thick films) or the substrate (in case of very thin films). Between these extremes, the behaviour is a function of the properties of both the film and the substrate materials.

In terms of hard coatings, neither plastic deformation nor interfacial bonding are common, which leads to the conclusion that friction is not an important factor in such ceramic films and that the residual stresses are not affected significantly. However, friction is an issue in soft coatings that are in contact with a hard counterface. Here, the ratio between the film thickness and the contact area determines whether the friction properties are governed by the coating or the substrate. Anyway, in case of soft coatings on hard substrates, the residual stresses and their distribution are affected by frictional load. The stresses introduced additionally depend strongly on the normal force, the ratio between the film thickness and the contact area, and the materials involved.[18]

Wear can be defined as the loss of surface-near material owing to fracture processes caused by the interaction of two surfaces.[18] Different types of wear can be classified according to their origin: adhesive wear, fatigue wear, abrasive wear, erosive wear, fretting wear, etc.[20] In most cases, the fracture process, which leads to failure of the component, is caused by mechanical load that induces the stresses in the coating or in the surface-near area in uncoated components.

1.3.4 Ion implantation

The structures and material properties of surface-near zones or thin films can be modified by implanting ions. Ion implantation is primarily used for doping semiconductors, but also for modifying the mechanical properties of functional components such as dies and surgical protheses. Yet, in some cases, implantation of ions is not wanted and should be minimized. When working with a Gallium-operated focused ion beam workstation (FIB), surfaces are unintentionally doped with Gallium ions. Since FIBs are becoming

more and more popular for small-scale sample preparation, the influence of Ga^+ ions on various materials has been analyzed intensively.

Investigations have shown that the amount of surface modification or surface damage generally depends on the materials and ions involved, the ion energy at impact, which is determined by the acceleration voltage, the impact angle, the sample temperature and the ion flux. Such surface damage can include amorphisation, compositional and structural changes, grain boundary embrittlement, film densification in case of coated surfaces, and changes of the residual stresses in surface-near zones.[37–39]

As one would expect, the stresses induced by ion bombardment are usually compressive owing to the implantation of Gallium as interstitials.[40,41] Nevertheless, in some cases, the residual stresses induced are tensile. Plastic deformation of the damaged zone and a temperature gradient owing to high energetic ions as well as the excessive production of vacancies has been proposed as reasons for tensile stresses due to ion implantation.[40,42]

1.4 Methods for Film Stress Measurement

The characterization of stresses in thin films is essential for random quality checks of coated components as well as for the development of new coatings and fabrication methods. Therefore, great effort was put into the development of stress measurement techniques for thin films. In general, these methods can be divided into methods, which determine the average stresses over relatively large areas or volumes, respectively, and more sophisticated techniques, which allow the determination of depth profiles and/or lateral distributions of residual stresses with high resolution.

1.4.1 Methods for Average Film Stress Measurement

The determination of mean values of residual stresses in thin films is sufficient for many applications. The techniques developed are predominantly technically mature and are usually relatively simple to apply. Such methods for mean stress measurement are based either on the measurement of the curvature of a coated substrate, or on the detection of the lattice strain by means of X-rays.

Determination of Film Stress from Substrate Curvature

A number of methods has been developed to determine the average stresses in thin films by measuring the curvature κ of the substrate and calculating the film stress σ_f by means of Stoney's equation

$$\sigma_f = \frac{\kappa E_{b,sub} t_{sub}^2}{6 t_f} \tag{1.3}$$

where $E_{b,sub}$ is the biaxial Young's modulus of the substrate calculated from $E_b = E/(1-\nu)$ and t_f and t_{sub} are the thicknesses of the film and the substrate, respectively.[1] It has to be taken into account that this equation only leads to useful results when the film is thin compared to the substrate. On the other hand, the substrate must not be too thick in order to lead to a measurable curvature. Therefore, the substrate thickness

is usually adapted to the thickness of the thin film and the expected stresses to allow wafer curvature measurements for scientific purposes.

Optical wafer curvature techniques can be applied to crystalline as well as amorphous materials with reflective surfaces. Subsequently, four optical methods are presented briefly.

Laser scanning methods are commonly used for rapid in-situ as well as ex-situ determination of average film stresses because the principle of this technique is very simple. A laser beam is scanned over the surface of the coated specimen and the curvature is calculated from the deviation of the reflected beam at the detector and the geometry of the experimental set-up (Fig.1.5). Such laser scanning devices are very sensitive and capable of detecting small curvatures or large radii of curvature, respectively.[2] On the other hand, serial scanning devices are sensitive to mechanical vibrations, which led to the development of multi-beam sensors described below.

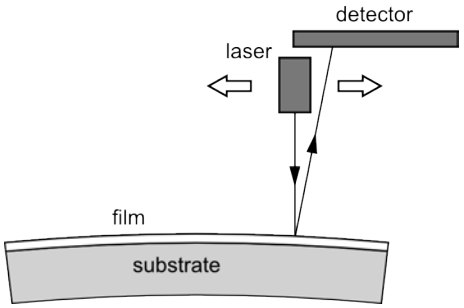

Figure 1.5: Principle of the wafer curvature method. The laser beam is scanned over the reflective surface of the coated system, which leads to a deviation of the reflected beam that is correlated with the curvature.

The more sophisticated **multi-beam optical stress sensor method**[5] works with a Helium Neon laser beam, which is split up by a highly reflective etalon and projected onto the sample. The laser light is reflected from the specimen surface onto a CCD camera, where the positions of the reflections are detected (Fig.1.6). As in case of the basic wafer curvature method, the curvature is determined from the experimental set-up and the stresses in the film are calculated from Stoney's equation. Compared with the basic laser scanning method, this technique has the advantage of being less sensitive to vibrations because the reflected beams are detected simultaneously.

The **grid reflection method**[6] detects the reflection of a periodic grid projected onto the sample. The shape of this reflection detected by a CCD camera is distorted owing to the curved specimen and allows the exact determination of the sample curvature. This method is especially useful for measuring full-field, nonuniform curvature evolution over large wafers and flat panels where the out-of-plane deflection is greater than the substrate thickness.[1]

The **coherent gradient sensor (CGS) method**[7] is a method for determining substrate curvatures by optical interferometry. Here, a coherent collimated laser beam is directed to the specularly reflecting specimen surface by means of a beam splitter (Fig.1.7). The beam reflected from the specimen then passes through the beam splitter and is then incident upon a pair of identical high-density gratings. The diffracted orders from the two gratings are spatially filtered using a filtering lens to form distinct diffraction spots

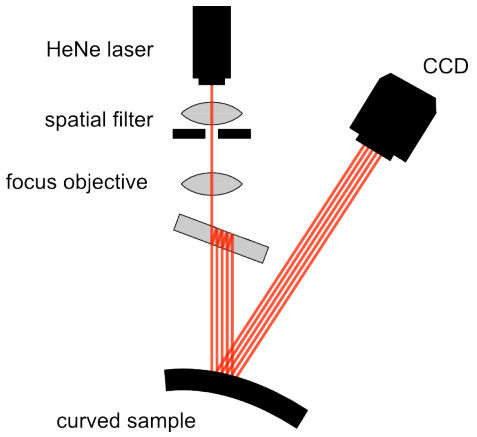

Figure 1.6: The multi-beam optical stress sensor method is a further development of the basic laser curvature method. Here, the deviation of a number of laser beams is detected simultaneously.[5]

on the filter plane. An aperture placed in this plane filters out the diffraction order of interest, which is then imaged onto the film plane. By moving the specimen in-plane, the interference pattern changes. Together with optical and geometrical parameters of the experimental set-up, this information is used to calculate the curvature of the coated specimen. The CGS method features a measurement area between a few and hundreds of millimeters, can be performed in-situ as well as ex-situ, and has a good accuracy. Nevertheless, it requires a detailed computer software package for the analysis of the fringe geometry and spacing.

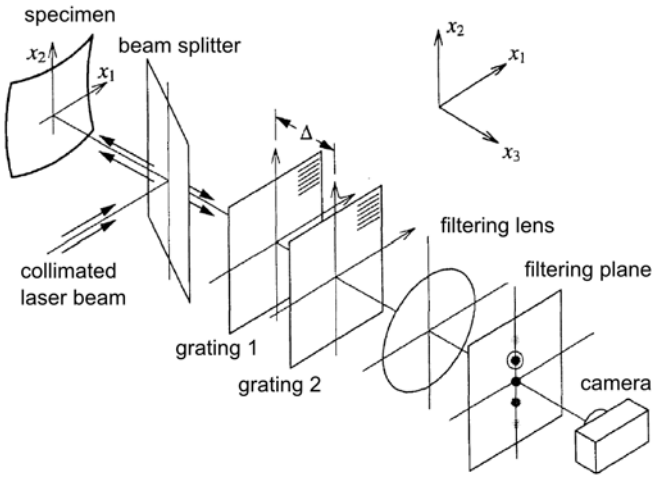

Figure 1.7: Schematic description of the coherent gradient sensor method.[7]

X-Ray diffraction can be used to determine the curvature of systems consisting of a thin film and a single crystalline substrate.[8,9] In principle, the X-ray diffraction technique is based on Bragg's law (Eq. (1.4)), which relates the normal spacing between crystallographic planes d_{hkl}, the angle of incidence and reflection Θ for a certain order n, and the wavelength λ.[1]

$$2d_{hkl}\Theta = n\lambda \tag{1.4}$$

The X-ray curvature technique works similarly to the conventional laser scanning method described above. An X-ray beam is scanned over the sample and is diffracted by the substrate's lattice planes (Fig.1.8). One peak is selected, the position of this peak as a function of the beam position on the sample is detected and correlated with the curvature of the coated substrate. Then, the film stress is calculated by means of Stoney's equation (Eq. (B.1)). Compared with the laser scanning method, the X-ray curvature technique provides much better resolution and accuracy, which permits the exact determination even of very small curvatures.

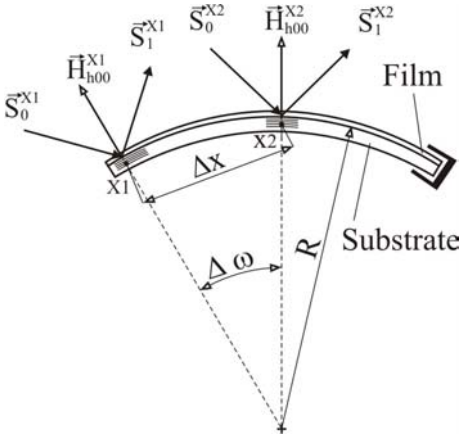

Figure 1.8: Principle of the X-ray curvature technique.[9] At position $X1$, the primary beam $\vec{S}_0^{X1}$ is diffracted by the lattice planes with the normal vector $\vec{H}_{h00}^{X1}$. The position of the secondary (diffracted) beam $\vec{S}_1^{X1}$ is detected. Then, the beam is moved by ΔX to position $X2$, where the position of the diffracted beam $\vec{S}_1^{X2}$ is determined. The radius of curvature R is calculated from the shift of the diffracted beams as a function of the positions of the primary beams on the sample.

Determination of Surface-Near Stresses from X-Ray Diffraction Measurement

X-ray diffraction can be used to determine the average stresses from the strain of the lattice planes of the thin film or the surface-near area directly, without considering the bulk or substrate material. This has the advantage that the stressed layer does not necessarily has to induce a measurable substrate curvature. On the other hand, it might be difficult to find reliable values for the X-ray elastic constants of the material investigated and it is not possible to determine the stresses of amorphous thin films.

The information about the lattice strain is averaged over a certain volume, which is a function of the beam diameter and the penetration depth of the X-rays. The penetration depth depends on the material investigated, the wavelength and the incident angle, but a depth of few ten micrometers can be considered as a useful estimated value. Therefore, X-ray diffraction experiments give true mean values of the stresses in case of thin films. The stresses in surface-treated bulk materials are not easy to evaluate, since the actual penetration depth of the X-rays has to be considered.

This non-destructive method can be applied to many crystalline materials. In contrast to curvature-measurement based techniques, this method allows the determination of residual stresses even on very thick substrates with virtually no curvature. Regarding thin films, the defect density in the thin film should not be too high because many defects lead to poorly defined and broad peaks, which can make the determination of the stress-induced peak shift and therefore the calculation of the strain impossible.[10]

1.4.2 Methods for the Determination of Depth Profiles of Residual Stresses

In most cases, information about the film stresses is averaged across the film thickness and large areas, which is sufficient to estimate the quality of a coated component or a thin film. Nevertheless, since thin film and multilayer systems become more sophisticated and surface-near structural elements smaller, often more detailed information is necessary. Especially when large gradients of residual stresses are expected, the knowledge of depth profiles or lateral distributions of residual stresses can help to understand the mechanics of such complicated coated systems and to prevent failure.

One of the major challenges is the optimization of the resolution of stress profiles in thin films, which is the reason for the limited number of methods available. Subsequently, two groups of established techniques, based on X-ray diffraction and Raman spectroscopy, respectively, are described briefly.

Grazing Incidence X-Ray Scattering

Grazing incidence X-ray scattering is a special application of the X-ray diffraction method, whereby the incident X-ray beams are made to impinge on the film surface at a very low angle of incidence, which leads to a reflection out of the film rather than into the film. By varying the grazing angle and therefore the penetration depth, strain as a function of penetration depth is calculated. The corresponding stress with a possible depth resolution on the nanometer scale is determined by means of fit functions and the X-ray elastic constants.[1] The lateral resolution usually lies in the millimeter range and depends on the beam diameter, the incident angle and the penetration depth of the X-rays.

Nevertheless, this method has to deal with a number of limitations like the restriction to crystalline materials, the difficulty of determining complex depth profiles of residual stresses, and the pronounced sensitivity on fit functions used in the evaluation procedure.[11]

Raman Spectroscopy

Raman spectroscopy is a non-destructive method used to determine spatial stress profiles. This method is based on the Raman effect, which can occur when light interacts with a molecule or a crystal. In such a case, there is a small possibility of transmitting energy from the photon to the material or vice versa, which results in a shift of the frequency of the inelastically scattered light. Depending on the shift (towards lower or higher frequencies), this effect is called Stokes Raman-scattering or Anti-Stokes Raman-scattering, respectively. The presence of lattice strain affects the presence of the spectral lines, the frequencies and the intensities. These relationships are complicated because the observed

spectrum depends on the crystal structure, the polarisation and propagation vectors of the incident and scattered light with respect to the crystal axes and the geometrical state of the local strain field. Therefore, there is no unique general relationship between the Raman spectrum parameters and the stress. Such relationships can only be deduced for special simple cases.[15]

One type of Raman spectroscopy is the so-called micro-Raman spectroscopy that is becoming more widely used to study stress distributions in solids. Here, the incident laser beam is focused to a micron size spot on the sample, which determines the lateral resolution. By varying the position of the focal plane, the stress as a function of distance from the surface can be determined. The depth resolution can vary from tens of nanometers to several millimeters, depending mainly on the material investigated and the wavelength of the laser. The principle of this technique is depicted in Fig.1.9.

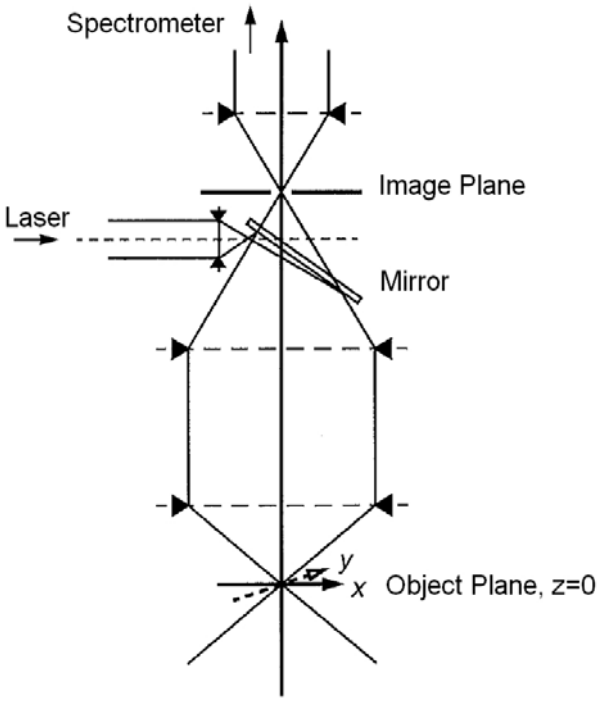

Figure 1.9: Schematic sketch of a micro-Raman spectrometer. The semi-transparent mirror reflects the laser light into the optical system, which focuses the light in the focal point $x = y = z = 0$. The light scattered back from the sample in the object plane is focused to the image plane and then enters the spectrometer.[13]

Micro-Raman spectroscopy can be applied to crystalline as well as to amorphous material as long as the Raman peak is well defined and the stresses in the surface-near region do not vary significantly. Especially in larger depths, pronounced stress gradients are difficult to measure because the incident and the scattered light beams are absorbed as they travel into and out of the specimen. Only some of the scattered light is collected by the microprobe optical system and reaches the detector to contribute to the observed spectrum. As a result, the Raman spectrum is collected from a relatively small, but fairly ill-defined region of the specimen.

Another challenge when applying this technique can be the calculation procedure,

which is not straightforward when applied to complex stress profiles. It requires the calculation of the expected spectra from an assumed or calculated stress distribution, which is then compared with the measured spectra. The assumed stress profile is then modified until its spectrum corresponds to the measured one. The analysis of stress profiles can even become more complicated because of contributions from the microscopic stress fields of crystal defects such as dislocations. Furthermore, the experiment can be affected by external parameters such as temperature stability of the detector and roughness of the sample. Anyway, the micro-Raman technique is becoming more widely used to study stress distributions in solids, particularly in micro electronics because of its potential for high spatial resolution.[12–15]

1.5 Fracture Mechanics of Thin Films

Fracture toughness of thin films is a topic of great interest. Particularly in the fields of microelectronics, where the film/substrate systems are usually subjected to thermal and growth stresses, and hard coatings, where additionally friction often contributes to the stress profiles, the investigation of crack nucleation and propagation is an important issue both for academic research and industry. Here we want to focus mainly on hard coatings and therefore concentrate on ideal brittle fracture.

What makes the investigation of fracture properties of coated systems interesting and challenging is the strong influence of the intrinsic residual stresses. Depending on the system and the deposition process, the film stresses can be either tensile or compressive, and often exhibit a more or less pronounced stress gradient, which has a significant effect on the fracture properties of the system.[21] Concerning hard tribological coatings on metal substrates, interface roughness often leads to high stress concentrations, which may lead to delamination resulting in failure of the coated component.[22] In order to improve the lifetime of coated components, it is essential to understand the fracture mechanisms and to obtain reliable data for the material combinations required as well as their dependence on deposition parameters. Subsequently, an overview over the fracture mechanical concepts used is given and methods for determining fracture properties of thin films are reviewed briefly.

1.5.1 Basic Fracture Mechanical Concepts

The Griffith theory is a common concept to describe pre-cracked brittle solids. It is a purely energetic approach that relates the stored elastic energy $U_{el} = \int \sigma d\epsilon$, the work of the external forces $U_w = \int F dx$, and the surface energy $U_s = \int \gamma d\Gamma$. Griffith states that the total potential energy of the specimen investigated decreases in case of instable crack growth (Eq. (1.5)).

$$\frac{dU}{da} = \frac{d(U_{el} + U_s - U_w)}{da} \leq 0 \tag{1.5}$$

Eq. (1.5) can be rewritten:

$$-\frac{d(U_{el} - U_w)}{da} \geq \frac{dU_s}{da} \tag{1.6}$$

The left part of Eq. (1.6) represents the energy provided for crack growth and is denominated energy release rate described by the variable G. The right part describes the energy necessary to produce new surface during crack growth and is called critical energy release rate G_c or crack resistance R. This criterion for instable crack growth can be used for mode I, mode II, mode III (Fig.1.10), and mixed mode loading and can be rewritten as

$$G \geq R. \tag{1.7}$$

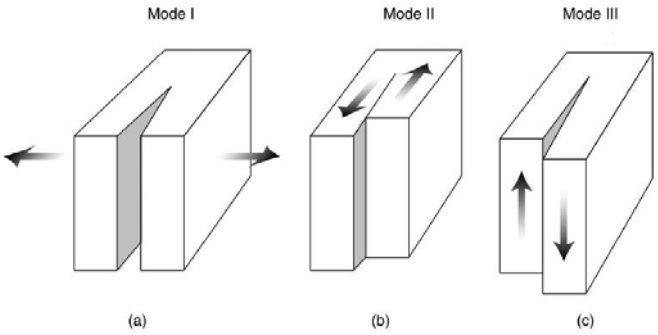

Figure 1.10: Classification of cracks according to the loading direction into mode I (a), mode II (b) and mode III (c).

Another way to describe fracture was introduced by Irwin. It describes the stress field near a crack tip of a linear elastic material taking into account a small crack in a large sample as depicted in Fig.1.11(a) for mode I loading. As depicted in Fig.1.11(b), the stresses near the crack tip are described by means of a function, which depends on the angle θ, the factor $1/\sqrt{r}$ with r representing the distance from the crack tip, and a scaling factor K called the stress intensity factor (Eq. (1.8)).

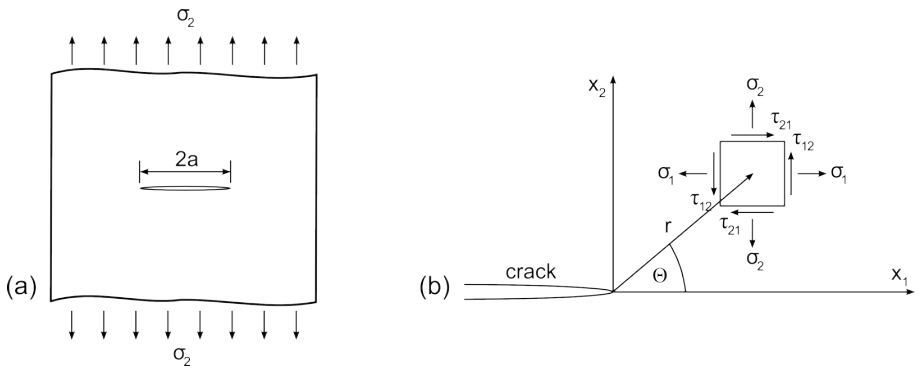

Figure 1.11: Cracked specimen under mode I loading (a). Stresss in an arbitrary element near the crack tip (b).

$$\lim_{r \to 0} \sigma_{ij} = \frac{K}{\sqrt{2\pi r}} f_{ij}(\theta) \tag{1.8}$$

Like the Griffith criterion, Irwin's concept can be used for mode I, mode II, mode III, and mixed mode loading. In simple cases, the stress intensity at the crack tip ($\theta = 0$ and $r \to 0$) is expressed by the applied stress σ_2 (Eq. (1.9)).

$$K = \sigma_2 \sqrt{\pi a} \tag{1.9}$$

The value of K at which the crack starts to grow instably is called critical stress intensity factor K_c and usually referred to when talking about fracture toughness of a material. K_c depends on the mode of loading, which is why it has to be distinguished between K_{Ic}, K_{IIc} and K_{IIIc}.

Although Griffith's and Irwin's criteria use different approaches to describe brittle fracture, the loading parameters G and K as well as the material parameters K_c and R or G_c, respectively, can be converted into each other. In case of plane stress, the energy release rate can be expressed as

$$G = \frac{K^2}{E}, \tag{1.10}$$

whereas in case of plane strain G is given by

$$G = \frac{K^2}{E} \left(1 - \nu^2\right). \tag{1.11}$$

The standards for the determination of the fracture toughness are derived from testing procedures used for bulk materials. It has to be mentioned that in general, toughness measurement for thin films is difficult due to the small dimension in thickness. Furthermore, the different elastic, plastic and fracture properties of the thin film and the substrate can complicate the evaluation significantly. Additionally, the fabrication of a pre-crack of defined dimensions is sometimes difficult or impossible. This leads to problems when determining the fracture toughness, which is defined as the ability of a material to resist the growth of a pre-existing crack. Therefore, in many cases, actually the toughness, which includes additionally the energy necessary to form a sharp crack, is determined.

Among other difficulties, this is why unlike for bulk materials, there is neither a standard testing procedure nor an accepted methodology to follow. Nevertheless, the most common methods developed for determination of fracture properties are subsequently presented briefly.[30]

1.5.2 Methods for Determining Fracture Properties

A number of techniques has been developed to determine fracture mechanical properties of thin films and thin film/substrate systems. These methods can be classified according to the fracture process, where it has to be distinguished between interfacial fracture (delamination) and the crack propagating in the actual coating, either parallel or normal to the surface. Common techniques to measure interfacial fracture are nanoindentation normal to the surface[24] and on the cross section,[25] scratch techniques,[26] and mechanical delamination tests.[27] In this thesis, the focus is put rather on the fracture of the actual thin films than on interfacial fracture properties, therefore a more detailed review of such testing methods is given.

Cantilever Beam Deflection Method

A cantilever beam deflection method for the determination of mechanical properties of thin films was presented among others by Ljungcrantz et al.[21] by means of a Ti film deposited on Si. For this technique, microscale cantilevers (about $170\mu m$ long, $130\mu m$ wide and 12 μm thick) are etched out of a bulk single crystalline Si wafer prior to film deposition. Then, a $1\mu m$ thick Ti film is deposited onto the substrate by means of a magnetron sputter process. The fracture experiments are performed in-situ in an SEM by applying a normal force at the free end of the beam by means of a diamond stylus positioned at the end of a lever. The fracture properties are calculated from the force-versus-deflection curve recorded, the elastic properties of the materials involved and the dimensions.

Free-Standing Thin Film Cantilever Method

This method developed by Matoy[43] is similar to the cantilever beam deflection method. Here, a series of cantilevers is pre-fabricated by photolithography at the edge of an already coated silicon substrate. Then, the Si substrate is etched in order to remove the substrate from the cantilevers, which leads to free standing $10\mu m$ long and about $2\mu m$ wide beams. Owing to this process, the shapes of the cantilevers are not well defined, which requires additional FIB milling to obtain the desired dimensions. The FIB is also used to introduce a defined pre-crack as depicted in Fig.1.12. The actual fracture experiment is performed by loading the tip of the cantilever with a nanoindenter. The geometry parameter of the pre-crack is determined and the fracture toughness of the film is calculated by means of a finite element simulation.

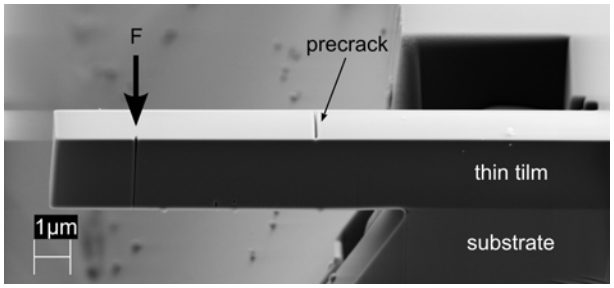

Figure 1.12: SEM image of a pre-cracked cantilever consisting of the thin film prepared for the free-standing thin film cantilever method. The pre-crack as well as the marks at the front of the cantilever, which are necessary for finding the correct loading position with the nanoindenter, are fabricated with a FIB workstation with low ion currents.[43]

Nanoindentation

Nanoindentation is a simple method to determine fracture properties of thin films. Here, a diamond indenter (Vickers, cube corner, spherical or Berkovich) is pushed into the surface under continuous measurement of the applied load and the resulting penetration depth. Crack formation and propagation in the thin film leads to discontinuities in the load-displacement curve. The mode of crack propagation depends on the materials involved, the film thickness, and the indenter type.[28,29] Although this method is widely

used for thin films, it has to be mentioned that the substrate properties influence the behavior of the system significantly and that the existence of a crack formation threshold and the exact determination of the crack length often leads to difficulties in the precise determination of fracture properties.[30]

Microtensile Fracture Tests

Jonnalagadda et al.[23] investigated mode I fracture toughness of amorphous diamond-like carbon films by means of a micro tensile test. First, the thin film is fabricated by pulsed laser deposition followed by the preparation of a dog-bone shaped specimen on the substrate by conventional photolithographic techniques as depicted in Fig.1.13a. A pre-crack is introduced by indenting the surrounding substrate material (Fig.1.13b). Then, the substrate is removed by wet etching the sacrificial layer (Fig.1.13c). The fracture test is performed with a custom-built microtension tester[31] as depicted in Fig.1.13d. In case of thin films with homogeneous stress profiles, this method is a good choice to investigate mode I fracture toughness in a reliable way. Things get more complicated when the films exhibit a stress gradient and the dog-bone specimen is curved. In that case, finite element analysis is necessary to estimate the influence of the curvature on the determined K_{Ic} value. What still has to be investigated is the influence of the etchant on the crack tip in the thin film material and the resulting effect on the fracture properties.

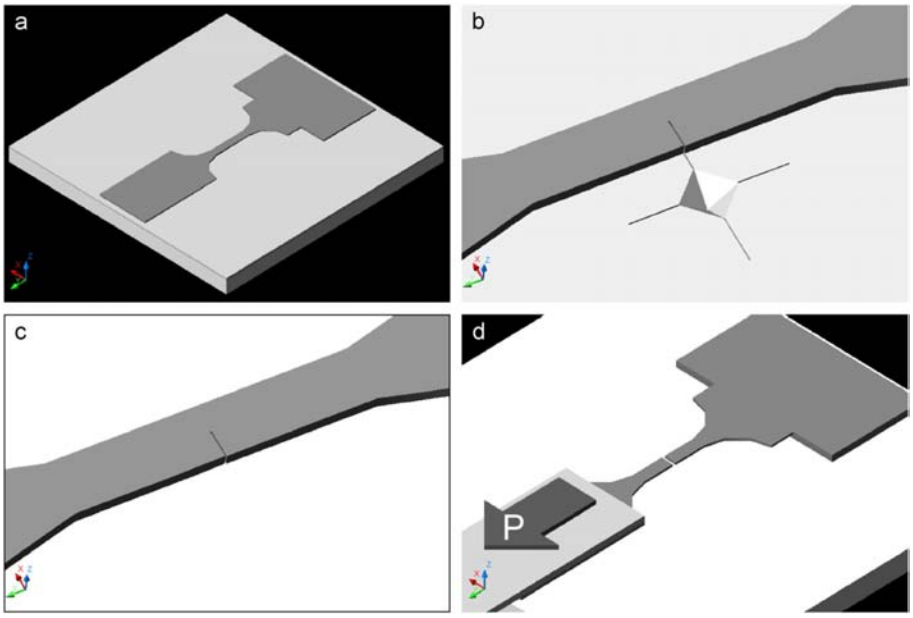

Figure 1.13: Microtensile fracture specimen preparation and testing: (a) dog-bone specimen on substrate, (b) specimen with pre-crack after indentation, (c) freestanding specimen with pre-crack after substrate removal, (d) testing procedure.[23]

Microbridge Method

The microbridge testing method and the corresponding analytical calculation procedure developed by Zhang et al.[32,33] allows the determination of the Young's modulus, the

average residual stress and the bending fracture strength of single-layer films deposited on Si substrates. The microbridge is fabricated by combined pattern and etching processes in order to fabricate a free standing thin film of a few ten microns length and a about $15\mu m$ width. The actual testing method depicted in Fig.1.14 is similar to the three-point bending test and is carried out with a load-displacement nanoindenter system equipped with a microwedge probe. With some assumptions and restrictions, this method can also be employed for the determination of mechanical properties of multilayer films as used in micro-electro-mechanical systems (MEMS). However, FEM simulations are necessary to determine the influence of the silicon edges supporting the free standing bridge, and the method is limited to Si substrates due to the etching process.

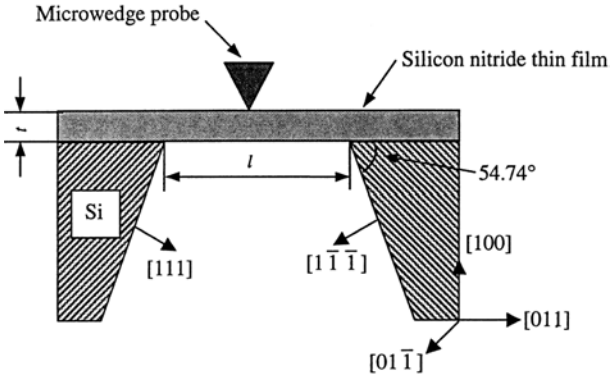

Figure 1.14: Schematic description of the microbridge test for a single layer. The base support (here 54.74°) results from the etching during sample preparation.[32]

Four-Point Bending Method

Four-point bending tests allow the determination of fracture properties of thin films, especially of hard coatings; a possible experimental set up is proposed by Jaeger et al.[34] A sharp crack is introduced into the bulk steel substrate by means of fatigue so that a certain portion of substrate remains crack-free. A side view of such a specimen having a bore hole instead of the crack tip is depicted in Fig.1.15. Then, the fatigue crack is closed, the side faces are shot blasted, and the hard coating is deposited by means of CVD on the side faces of the pre-cracked steel substrate. The four-point bending test is carried out in two cycles. During the first cycle, the film ruptures and the load-displacement curve of the crack advancing in the thin film is measured. The second cycle is necessary to obtain the substrate influence of the coated specimen, which allows the determination of the film properties in the first loading cycle. The fracture properties are calculated from the load and the corresponding compliance change during successive crack growth on the sides.

This method is suitable for the determination of fracture properties of thin films on metallic substrates, but the probable influence of the pre-crack on the subsequent film growth is not clear yet.

1

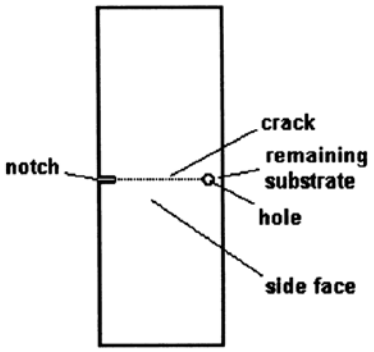

Figure 1.15: Side view on the four-point bending steel specimen. First, a pre-crack is introduced in the uncoated specimen. Then, the specimen is shot blasted and coated by means of a CVD process. The specimen is tested and the load-deflection curve of the film and the substrate is recorded. Then, after cracking the film, the compliance of the substrate is determined by loading the specimen a second time. Both curves are necessary to obtain the fracture properties of the film.[34]

Bibliography

[1] Freund LB, Suresh S. Thin Film Materials. Cambridge: Cambridge University Press; 2003. p. 90.

[2] Nix WD. Metall Trans A 1989;20A:2217.

[3] Nix WD, Clemens BM. J Mater Res 1999;14:3467.

[4] Spaepen F. Acta Mater 2000; 48:31.

[5] Floro JA, Chason E, Lee SR. Mat Res Soc Symp Proc 1996;406:491.

[6] Finot M, Blech IA, Suresh S, Fujimoto H. J Appl Phys 1997;81:3457.

[7] Rosakis AJ, Singh RP, Tsuji y, Kolawa E, Moore Jr NR. Thin Solid Films 1998;325:42.

[8] Keckes J, Eiper E, Martinschitz KJ, Köstenbauer H, Daniel R, Mitterer C. Rev Sci Instrum 2007;78:036103.

[9] Eiper E, Martinschitz KJ, Keckes J. Powder Diffr 2006;21:25.

[10] Noyan IC, Cohen JB. Residual Stress. New York: Springer; 1987.

[11] Genzek C. Mater Sci Technol 2005;21:10.

[12] Grabner L. J Appl Phys 1978;49:580.

[13] Dietrich B, Dombrowski KF. J Raman Spectr 1999;30:893.

[14] De Wolf I. J Raman Spectr 1999;30:877.

[15] Atkinson A, Jain SC. J Raman Spectr 1999;30:885.

[16] Smithells CJ, Brandes EA. Metals Reference Book, 5th edition. Butterworths; 1976.

[17] Martinschitz KJ, Daniel R, Mitterer C, Keckes J. Thin Solid Films 2008;512:1972.

[18] Arnell RD. Surf Coat Technol 1990;43/44:674.

[19] Eisenmenger-Sittner C. Vorlesung "'Technologie dünner Schichten"' 2007. Technische Universität Wien.

[20] Stachowiak GW, Batchelor AW. Engineering Tribology. Butterworth-Heinemann; 2001.

[21] Ljungcrantz H, Hultman L, Sundgren JE, Johansson S, Kristensen N, Schweitz JA, Shute CJ. J Vac Sci Technol A 1993;11:543.

[22] Wiklund U, Gunnars J, Hogmark S. Wear 1999; 232:262.

[23] Jonnalagadda K, Cho SW, Chasiotis I, Friedmann T, Sullivan J. J Mech Phys Solids 2008;56:388.

[24] Volinsky AA, Vella JB, Gerberich WW. Thin Solid Films 2003;429:201.

[25] Li XF. Surf Coat Technol 2006;200:5003.

[26] Kriese MD, Boismier DA, Moody NR, Gerberich WW. Eng Fract Mech 1998;61:1.

[27] Kitamura T, Hirakata H, Itsuji T. Eng Fract Mech 2003;70:2089.

[28] Weppelmann E, Swain MV. Thin Solid Films 1996;286:111.

[29] Morasch KR, Bahr DF. Thin Solid Films 2007;515:3298.

[30] Zhang S, Sun D, Fu Y, Du H. Surf Coat Technol 2005;198:74.

[31] Cho SW, Chasiotis I, Friedman TA, Sullivan J. J Micromech Microeng 2005;15:728.

[32] Zhang TY, Su YS, Qian CF, Zhao MH, Chen LQ. Acta Mater 2000;48:2843.

[33] Zhang TY, Wang X, Huang B. Mat Sci Eng A 2005;409:329.

[34] Jaeger G, Endler I, Heilmaier M, Bartsch K, Leobhardt A. Thin Solid Films 2000;377:382.

[35] Mayrhofer P. Vorlesung "'Basics of Deposition and Materials Science of Hard Coatings"' 2007. Montanuniversität Leoben.

[36] Zengerle R. Vorlesung "'Dünnschichttechnik"' 2007. Albert-Ludwigs-Universität Freiburg.

[37] Ohring M. Materials Science of Thin Films. Second Edition: Academic Press; 2002.

[38] Kiener D, Motz C, Rester M, Jenko M, Dehm G. Mater Sci Eng A 2007;459:262.

[39] Halitim F, Ikhlef N, Boudoukha L, Fantozzi G. Thin Solid Films 1997;300:197.

[40] Chan WL, Chason E, Iamsumang C. Nucl Instr and Meth B 2007;257:428.

[41] Kalyanasundaram N, Wood M, Freund JB, Johnson HT. Mech Res Commun 2008;35:50.

[42] Marques MJ, Pina J, Dias AM, Lebrun JL, Feugeas J. Surf Coat Technol 2005;195:8.

[43] Matoy K, Schönherr H, Detzel T, Schöberl T, Pippan R, Motz C, Dehm G. submitted to Thin Solid Films

1

Aim of the Dissertation

The aim of this work is to develop a FIB-based cantilever method that allows the determination of residual stress profiles in near-surface structures on a nanoscale. Furthermore, special attention is paid to the effect of residual stresses and their distribution on the fracture properties of thin films.

The determination of distributions of residual stresses in thin films is an issue of great importance owing to their significant influence on the lifetime of coated components. Most of the methods available measure the mean values, which can lead to a significant over- or underestimation of the stresses when the coating exhibits a pronounced stress gradient. Two types of techniques, based on Raman spectroscopy and X-Ray diffraction, respectively, allow the determination of depth profiles of residual stresses, but the materials investigated need to be either Raman active or crystalline and the complex calculation procedures sometimes involve sophisticated simulations. The method developed in this dissertation can be applied to a broad range of materials and allows the precise determination of depth as well as spatial stress profiles.

Along with the residual stresses, the actual fracture properties are of great importance for the structural integrity of coated systems. Compared with bulk materials, the determination of strength and fracture toughness of thin films is not a straightforward task. The main challenges are the small dimensions of thin films and the complicated stress state in the material as a result of superimposing the residual stresses and the stresses induced by the loading. The technique presented in this work is based on the determination of the depth profile of residual stresses and the subsequent testing of FIB-fabricated microcantilevers with a microindenter. The information about the stress profile as well as the simple specimen- and loading geometry allow a precise and reproducible determination of strength and fracture toughness.

1

Summary

The main task of this dissertation is to develop a method –named **i**on beam **l**ayer **r**emoval (ILR) method– that allows the determination of profiles of residual stresses on a nanoscale and to evaluate the influence of experimental errors and parameters.

This method presented in **paper A** is based on the fabrication of a cantilever by means of a focused ion beam workstation (FIB) in the vicinity of the specimen edge. In the presented example, a Zeiss XB1540 crossbeam FIB, which combines a Gallium-operated 30kV FIB and a high-resolution scanning electron microscope (SEM) equipped with a field emission gun, is used to fabricate the cantilever from a system consisting of a $840nm$ thick Ni film separated from the single crystalline (100) Si substrate by a SiO_x/SiN_x diffusion barrier. The cantilever beam is about $100\mu m$ long, consists of the thin film and the $3\mu m$ thick substrate and bends owing to the residual stresses, similar to a bimetallic strip. The deflection of the free end of the cantilever is measured with the SEM at high magnification. By simple geometrical considerations, the curvature is calculated from the deflection measured. Now the thin film is removed gradually in a part of the cantilever denominated section A with the ion beam aligned parallel to the sample surface, which leads to a change of the curvature in this section owing to the removal of the stressed material as depicted in Fig.1.16 for a TiN film on Si.

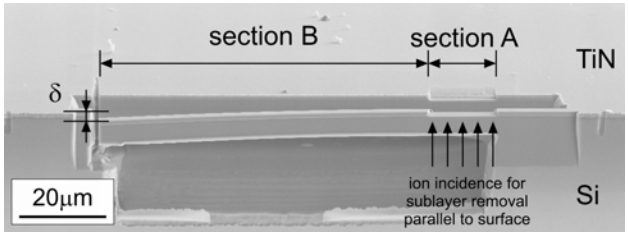

Figure 1.16: An example of a FIB-fabricated cantilever deflecting owing to residual stresses (inclined view). The thin film is removed gradually in section A with the ion beam aligned parallel to the surface leading to a change of the curvature of section A, which is amplified by section B that acts as a curved indicator.

The thin material slices removed from the film in each step are called sublayers; the thickness of the individual sublayers is determined from the difference of the film thicknesses between two consecutive steps. The change in curvature is amplified by the rest of the cantilever, section B, which still has the curvature of the original cantilever and acts as a curved indicator. The measured deflection as a function of film thickness is the basis for the calculation procedure that leads to the stress profile in the cantilever and finally to the depth profile of residual stresses in the initial system.

The calculation procedure of the stress profile in the cantilever is based on the stepwise superposition of the previously removed sublayers in section A taking into account the force and moment balances. Besides the curve that describes the deflection as a function of film thickness, the procedure requires the dimensions of the cantilever and the elastic constants of the materials involved. The Young's moduli and the Poisson's ratios are necessary to calculate the biaxial Young's moduli in order to account for the two dimensional (cross sectional) consideration of an actually three dimensional problem.

The resulting depth profile of residual stresses in the cantilever is described by a step function with step widths that correspond to the thicknesses of the individual sublayers. As a result of the calculation procedure, the stresses in each of the sublayers are distributed homogeneously across the sublayer thickness and can be approximated well by the mean stresses. The stress profile in the cantilever can be converted into the corresponding stress distribution in the thin film of the initial system assuming linear elastic material behaviour. The depth profile obtained shows a gradient of residual stresses in the Ni film growing from the surface towards the interface, reaching a maximum value of $792 \pm 103 MPa$ and dropping to $620 \pm 110 MPa$ in the diffusion barrier. The average stress in the Ni film, not taking into account the diffusion barrier, is $460 \pm 60 MPa$. The result is compared with wafer curvature measurements performed approximately one year prior to this experiment taking into account the stress relaxation of Ni at room temperature ($581 \pm 58 MPa$).

Although the average stresses of the ILR method and the wafer curvature technique correspond well, additional effort was made to check the reliability of the result obtained. Possible sources of error could be plastic relaxation of the material during the experiment and ion-beam induced stresses. Therefore, a second cantilever experiment was performed. This time, the cantilever thickness in section A was not reduced by removing the thin film gradually, but by removing thin sublayers from the substrate material in this section. This also affects the stresses in section A, but leads to different stress states. The unavoidable ion damage is now mainly concentrated on the Si substrate. As before, the change of the deflection as a function of substrate thickness in section A is measured. Now the depth profile of residual stresses in the Ni film obtained in the first cantilever experiment is used to simulate the change of the deflection of the second experiment. The excellent correlation of the experimentally determined and the calculated curve indicate that neither plastic deformation nor significant ion damage influenced the result.

In order to investigate the influence of experimental errors and parameters on the depth profile of residual stresses determined, the possible sources of error are analyzed and discussed in **paper B** by means of a stress profile determined in a $1.16 \mu m$ thick TiN film on a single crystalline (100) Si substrate and four model stress distributions representing possible stress profiles. The errors that influence the result obtained by means of the ILR method are classified into errors resulting from ion damage, the accuracy in measuring the dimensions of the cantilever, the limited number of sublayers the thin film is divided into, as well as the uncertainty of the input material parameters.

Ion damage cannot be avoided when working with a FIB. A fast and simple way to estimate roughly the implantation depth of the ions is to perform a SRIM (The stopping range of ions in matter*) simulation, which takes into account the ions and materials

*Ziegler JF, Biersack JP, Littmark U. The Stopping Range of Ions in Matter. New York: Pergamon

involved, the incident angle, the ion current and the ion energy or acceleration voltage, respectively. Additionally, it is necessary to check the literature if the ions and materials involved lead to grain boundary embrittlement, for example, as it is the case for Ga ions and Al. In this case, the material cannot be investigated in a Ga-operated FIB.

Concerning the accuracy in measuring the dimensions of the cantilever and the individual sublayers, it has to be distinguished between systematic and statistical errors. Systematic errors, which usually result from insufficient calibration, lead to a general over or underestimation of measured lengths. In this case, statistical analysis is not generally useful to quantify such errors. Therefore, a careful calibration of the SEM prior to the experiment by means of a calibration device of defined length is essential. Statistical errors are fluctuations in observations which yield results that differ from measurement to measurement and can be approximated well by the normal distribution. This distribution is used to describe the errors in the dimensions and the elastic constants, which can be obtained from literature or determined experimentally.

An important measure to avoid errors is to divide the thin film into a large number of sublayers. A high number of thin sublayers is necessary to reproduce the details of the stress variations well by the step function when a jagged stress profile is expected. On the other hand, an increase in the number of sublayers leads to a decrease in the mean sublayer thickness and therefore to larger relative errors in the thickness measurement. Therefore, an increase of the error of the calculated stresses is expected when the error of the thickness measurement increases. Anyway, a homogeneous stress profile cannot be assured prior to the experiment and therefore, the division of the film into many thin sublayers usually leads to more accurate results as shown by means of the four model stress distributions.

The cantilever dimensions have to be chosen carefully in order to obtain useful deflections and to avoid fracture or plastic deformation during the experiment. In principle, section B that acts as curved indicator, should be as long as possible in order to amplify the deflection changes in section A significantly, but the fabrication of a long indicator requires long FIB milling times. Therefore, a compromise between useful amplification of the curvature change and milling time has to be made. The experiments performed show that lengths of section B between $50\mu m$ and $100\mu m$ usually lead to convenient results. The length of section A, where the material is removed gradually, depends on the corresponding curvature in this section. On one hand, section A should be as long as possible in order to lead to pronounced curvature changes. On the other hand, it has to be short enough to allow being considered straight despite being actually curved. Here, lengths of section A of about $15\mu m$ are usually a good compromise. The most important measure is the selection of a convenient substrate thickness because it influences the stresses in the cantilever directly and can lead to plastic deformation or fracture. Owing to the difference of the systems that can be investigated, no general advice about useful substrate thicknesses can be given. An easy and reliable way to estimate the stresses roughly is to measure the mean stresses in the initial system by means of the common wafer curvature technique, for example, and then calculate the stresses that appear during the experiment for various substrate thicknesses.

The stress profile in the $1.16\mu m$ thick TiN film investigated features two main charac-

Press;1985, p. 321.

teristics. Firstly, the stresses grow nearly exponentially from $-0.81GPa$ at the surface to $-3.39GPa$ at the interface. Secondly, the corresponding errors of the stresses in the individual sublayers or the standard deviations, respectively, range from $0.11GPa$ at the surface to $0.87GPa$ at the interface, which can be explained analyzing the deflection as a function of film thickness. The deflection does not change significantly with the film thickness in the region near the surface, but it shows a strong gradient near the interface. Here, the change in the magnitude of the errors in the sublayers is caused by the uncertainty in measuring the film or sublayer thickness, respectively because the influence of this error is much smaller near the surface than in the vicinity of the interface owing to the shape of the deflection versus film thickness curve.

A further development of the ILR method is the three dimensional ion beam layer removal (3D-ILR) method presented in **paper C**. This technique allows the determination of spatial residual stress profiles in near-surface structures and is presented by investigating the residual stress field in and around the plastic zone resulting from a shallow scratch in the Ni film investigated in paper A.

The 3D-ILR method provides two dimensional stress profiles from a number of parallel cross sectional cuts through a spatial stress profile. In each experiment, the stress component along the cantilever fabricated parallel to the edge is determined. The stresses perpendicular to the cantilever relax partially, depending on the cantilever width; a determination of these stresses would require the fabrication of another cantilever perpendicular to the specimen edge. The experimental and calculation procedure for the two-dimensional stress profiles is similar to the procedure of the basic ILR method.

The experimental procedure starts with FIB cut performed at the edge of the specimen to obtain a plane view on the cross section of the scratched system. This cross section is divided into a number of a few microns wide sections. A cantilever is fabricated from this cross section in a way that it is located far away from the plastic zone and the ILR method is performed to obtain the depth profile of residual stresses. Now the cantilever is elongated by removing the substrate material in the section next to the cantilever, which leads to a change in the deflection. Then, the film thickness is reduced gradually in this new section and the stress distribution is calculated. This procedure of elongating the cantilever by the length of the adjacent section, removing the thin film gradually and measuring the corresponding deflection is repeated until the center of the scratch is reached.

The calculated depth profiles of residual stresses as a function of the lateral position normal to the scratch shows a general trend: far away from the scratch, the depth profile of residual stresses exhibits a gradient growing from the surface towards the interface as described in paper A and an average stress of $460 \pm 60MPa$. This stress gradient decreases moving towards the center of the scratch, where finally the residual stresses are homogeneously distributed over the film thickness at a mean stress of $-478 \pm 91MPa$. This example presents the ability of the 3D-ILR method to determine spatial stress profiles with a depth resolution on a nanoscale and a lateral resolution in the micron range.

Besides the residual stress profiles, fracture toughness and strength of thin films are essential for the structural integrity and the lifetime of coated components. In **paper D**,

a new method that allows the straightforward and reliable determination of the fracture properties of thin films is presented by means of a $1.1\mu m$ thick magnetron-sputtered TiN film on single crystalline (100) Si.

The method is based on the determination of the depth profile of residual stresses in the thin film and the subsequent testing of FIB-fabricated cantilevers of different substrate thicknesses by means of an in-situ microindenter mounted in an SEM. The variation of substrate thicknesses leads to different film stresses and allows therefore the investigation of the fracture properties as a function of these stresses. In total, eight cantilevers are investigated. Four cantilever beams used for the determination of strength are tested in the as-fabricated state, whereas the remaining four are provided with a 200nm deep FIB-fabricated notch at the origin of the beam in order to investigate the fracture toughness.

The depth profile of residual stresses is determined by means of the ILR method and shows a homogeneous stress distribution in the TiN film with an average stress of $-1.5GPa$. The cantilevers for the actual fracture experiments are fabricated by means of the FIB and are about $50\mu m$ long. The substrate thicknesses range from $2\mu m$ to $10\mu m$, which leads to different deflections resulting from the residual stresses. Now the cantilevers are loaded with the in-situ cube corner indenter until fracture. The load-deflection curves determined show perfect linear behaviour of all cantilevers tested. The fracture toughness and the strength of the TiN film are calculated in principle from the load at fracture, the loading geometry and the cantilever dimensions by superimposing the residual stresses and the stresses resulting from the loading. The values obtained of $2.8 \pm 0.3MPa\sqrt{m}$ for the fracture toughness and $4.4 \pm 0.7GPa$ for the strength are compared with the material parameters found in the literature for comparable thin films. The fracture toughness corresponds well to results obtained by Kamiya et al.[†], whereas the strength lies between the values found in literature, which range from $2.6GPa$[‡] to $7GPa$[§].

The results show that the TiN film investigated exhibits reasonable fracture toughness and can sustain significant tensile stresses. SEM pictures of the fracture surfaces reveal that intergranular cleavage is the predominant fracture mechanism, which has been reported repeatedly in literature. In combination with the high strength determined from the cantilevers without pre-crack, this leads to the conclusion that the strength of the grain boundaries is remarkably high. Therefore, compressive residual stresses in such films are important, but definitely not the single most important factor for the mechanical stability of coated systems.

The basic equations necessary for the description of residual stresses in coated systems are derived in **paper E**. This paper will not be published in a journal, but this summary of the equations is very useful and therefore listed in this dissertation.

First, a model system consisting of a thin film and a substrate with different coefficients of thermal expansion containing residual stresses produced by applying $\Delta T \neq 0$ is introduced. A sign convention is suggested in order to obtain a uniform description of such systems. An important point is the description of the conversion procedure between the system used for the calculations, which is straightened by external forces or

[†]Kamiya S, Nagasawa H, Yamanobe K, Saka M. Thin Solid Film 2005;473:123.
[‡]Kamiya S, Hanyu H, Amaki S, Yanase H. Surf Coat Technol 2007;202:1154.
[§]Qin M, Ju DY, Wu YN, Sun C, Li JB. Mater Charact 2006;56:208.

the corresponding bending moments, respectively, and the relaxed system, which curves owing to the internal residual stresses. Then, the equations derived are used to calculate the depth profile of residual stresses of a model system consisting of a thin film and a thick substrate. Finally, the result is compared with Stoney's equation[¶].

In summary, the layer removal method presented allows the determination of residual stress profiles in near-surface structures with a depth resolution on a nanoscale and a lateral resolution in the micron range. It can be used to investigate depth- and spatial stress distributions in crystalline as well as amorphous materials. The cantilever bending technique developed allows the determination of strength and fracture toughness of thin films. Owing to the simple specimen and loading geometry, this method provides a very precise and reliable way for the investigation of such fracture properties.

[¶]Nix WD. Metall Trans A 1989;20A:2217.

2 List of appended papers

Paper A
S. Massl, J. Keckes and R. Pippan
A Direct Method of Determining Complex Depth Profiles of Residual Stresses in Thin Films on a Nanoscale
Acta Materialia 55 (2007) 4835–4844

Paper B
S. Massl, H. Köstenbauer, J. Keckes and R. Pippan
Stress Measurement in Thin Films with the Ion Beam Layer Removal Method: Influence of Experimental Errors and Parameters
Thin Solid Films, accepted for publication

Paper C
S. Massl, J. Keckes and R. Pippan
A New Cantilever Technique Reveals Spatial Distributions of Residual Stresses in Near-Surface Structures
Scripta Materialia, accepted for publication

Paper D
S. Massl, W. Thomma, J. Keckes and R. Pippan
Investigation of Fracture Properties of Magnetron-Sputtered TiN Films by Means of a New FIB-Based Cantilever Bending Technique
Acta Materialia, under preparation

Paper E
S. Massl, J. Keckes and R. Pippan
Mechanics of Residually Stressed Coated Systems: Derivation of Basic Equations
not published

A

A Direct Method of Determining Complex Depth Profiles of Residual Stresses in Thin Films on a Nanoscale

S. Massl[a], J. Keckes[b] and R. Pippan[a]

[a] Erich Schmid Institute of Materials Science, Austrian Academy of Sciences, A–8700 Leoben, Austria
[b] Department Materials Physics, University of Leoben, A–8700 Leoben, Austria

Abstract

A cantilever method of determining complex depth profiles of residual stresses is presented by means of a $840nm$ thin Ni film on a Si substrate. The technique developed is based on the fabrication of a microcantilever and the subsequent gradual reduction of film thickness using a focused ion beam workstation. The deflection as a function of film thickness is measured directly from SEM images, and the stress distribution in the thin film is determined by means of a straightforward calculation procedure. The method can be applied to crystalline as well as amorphous materials and permits stress profiles on a nanoscale to be determined.

A.1 Introduction

Most thin films and structural elements on surfaces are residually stressed as a result of thermal mismatch, the fabrication process or the applied load. Residual stresses and their distribution are essential for the mechanical performance, structural integrity and lifetime of the components.

A number of methods have been developed for quantifying residual stresses. Most of these methods determine the mean stresses in relatively large volumes or relatively large areas in thin layers. They give useful results when the residual stresses are distributed uniformly and a significant stress gradient is not expected. The mean stress is determined either directly, by measuring the curvature of a residually stressed coated system,[1–3] or indirectly, by calculating the stress from the measured lattice strain and the elastic constants of the material analyzed.[1,4]

In many cases, residual stresses are not distributed uniformly over the film thickness or the investigated volume. Complex stress distributions can be produced during the growth process of films, for example. Such depth profiles of residual stresses can be determined by grazing incidence X-ray techniques,[5] which achieve depth resolution on a nanoscale, but can only be applied to crystalline materials and do not measure the stresses directly. Depending on the material and the film thickness, the lateral resolution is limited to values $> 10\mu m$ owing to the grazing incidence of the X-rays.

A new method –the ion beam layer removal method (ILR method)– is presented. It permits the local determination of residual stress distributions in planar surface-near structures on a nanoscale directly by measuring the deflection of a focused ion beam (FIB) fabricated microcantilever as a function of gradually reduced cantilever thickness. The method is presented on a Ni/Si model system, the evaluation procedure is described and the advantages as well as the limitations are discussed.

A.2 Principle of the ILR Method

A cantilever of adequate dimensions is fabricated from the initial Ni/Si system with a FIB workstation. It consists of the substrate and the thin film, and deflects owing to residual stresses. The thickness of the cantilever is reduced step by step by removing the thin film gradually top-down with the ion beam. This affects the stress distribution and therefore, the deflection of the cantilever. The mean stress that acts in the removed sublayer is determined for each step from the actual deflection that is measured from SEM images, the biaxial Young's moduli and the dimensions of the cantilever. The stress profile in the cantilever is determined by superimposing the previously removed sublayers and establishing the force and moment balances by means of the calculation procedure developed. Finally, the stress distribution in the initial system is calculated from the stress profile of the cantilever.

A.3 Experimental

The ILR method is presented by means of a Ni/Si system. It consists of a $210\mu m$ thick monocrystalline pure (001) Si substrate coated with a $100nm$ diffusion barrier and a

840nm PVD-deposited Ni film. The diffusion barrier should consist ideally of 50nm thermally grown SiO_x and 50nm CVD-deposited SiN_x, but the SEM micrograph shows significant discontinuities in the barrier (Fig.A.1).

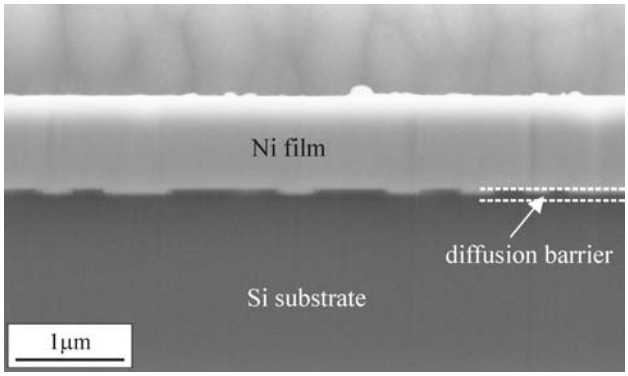

Figure A.1: SEM image of the interface. The Ni film (bright) is separated from the Si substrate (grey) by the imperfectly structured diffusion barrier (dark grey).

The system was annealed at 600°C for 15 min in UHV to reduce the defect density in the Ni film and to enhance a (111) texture.[6]

The cantilever is fabricated in the vicinity of the specimen edge with a Zeiss 1540XB focused ion beam workstation that combines a FIB column and an ultra-high-resolution SEM column with a field emission gun. The raw cantilever is produced with a current of 10nA and an acceleration voltage of 30kV. First, the front- and back are milled, then the specimen is tilted about 90° and the bottom side of the cantilever is fabricated. The resulting raw structure is similar to a microbridge consisting of the substrate and the thin film (Fig.A.2).

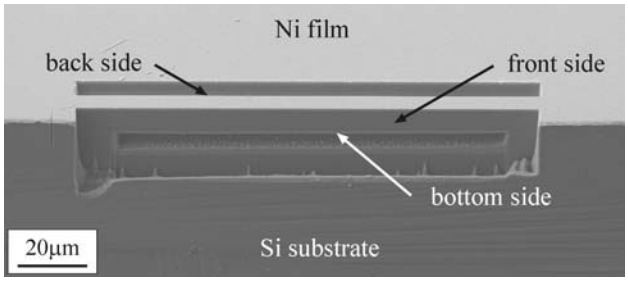

Figure A.2: SEM image of a FIB-fabricated microbridge at the edge of the specimen (inclined view). First the front and back sides are milled, then the bottom side is fabricated.

The cantilever obtains its final dimensions by milling with an ion current of 500pA and an acceleration voltage of 30kV to ensure a smooth surface, well defined dimensions and to minimize ion damage. The thickness of the cantilever must be adjusted to the expected residual stress distribution to ensure small, but measurable deformations. In the present example, the mean stress in the thin film of the initial system is obtained from a wafer curvature experiment and serves as an estimation for the real stress distribution. The corresponding mean stress and the deflection of the cantilever are calculated for various substrate thicknesses, as described in section A.4.4., until an appropriate thickness is

found. In the present case, a useful substrate thickness of $3\mu m$ leads to deflections between $2\mu m$ and $3\mu m$ for a cantilever length of about $100\mu m$. The fabricated cantilever is $3\mu m$ wide.

The cantilever is cut free at one end and deflects owing to the residual stresses (Fig.A.3(a)). The deflection is measured with the high-resolution SEM of the Crossbeam FIB workstation at high magnification. Therefore, the stage is tilted so that the electron beam is parallel to the thin film surface and the deflection can be determined directly. For FIB milling, the stage is tilted back into the cutting position. Now the thin film is removed sublayer by sublayer in the indicated section, denominated section A, with a current of $50pA$ (Fig.A.3(b)). In the present example, the length of section A is $17\mu m$, and the thin film is divided into eight sublayers. Owing to the reduction of the cantilever thickness, the stress distribution and the curvature in section A changes. The rest of the cantilever, denominated section B, acts as a curved indicator that amplifies the curvature of section A. The deflection as a function of the cantilever thickness is depicted for the present example in Fig.A.4.

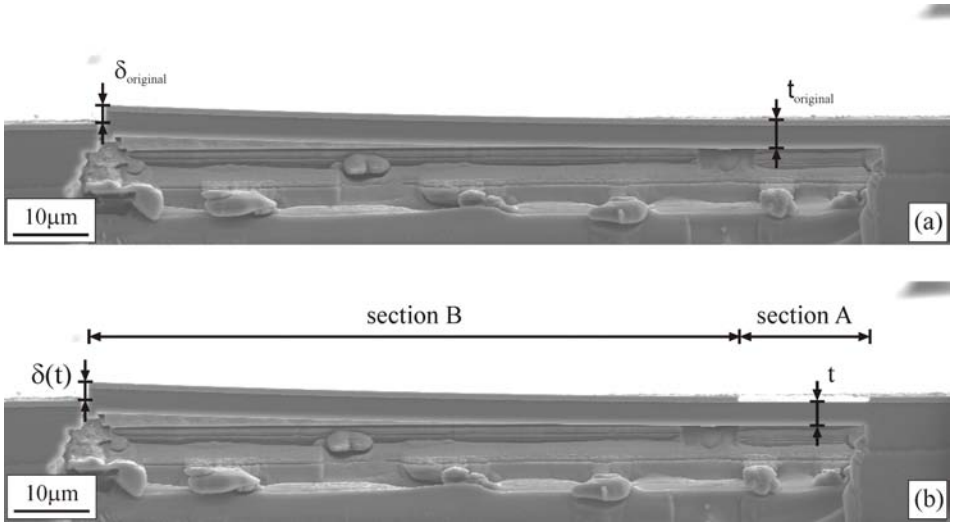

Figure A.3: (a) The original cantilever deflects due to residual stresses. (b) The cantilever thickness t is reduced gradually top-down in section A and the corresponding deflections $\delta(t)$ are measured from high-magnification SEM images of the cantilever tip region.

A.4 Calculation Procedure and Results

A.4.1 General Description of Residual Stress Distributions in Coated Systems

Residually stressed coated systems can be described in two equivalent ways. To explain the two descriptions, the cross sections of two simple bimaterial systems –system (a) and system (b)– are considered. The lateral dimensions of both systems are much bigger than the thickness, therefore, the biaxial Young's moduli of the thin film $E_{b,f}$ and the substrate $E_{b,s}$ are used in the calculation procedure. The 2D approach has to be taken into account for the calculation in terms of the dimensions of the forces, moments etc.

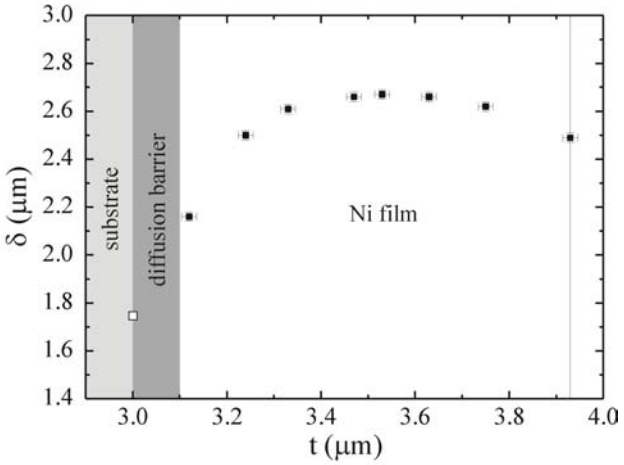

Figure A.4: Deflections measured from SEM images δ (■) as a function of cantilever thickness t in section A. Additionally, the predicted deflection (□) for the completely removed thin film and diffusion barrier in section A is drawn in.

System (a) is initially separated (Fig.A.5(a)). Balanced external forces are applied on the thin film and the substrate to compensate for the difference in length that can be caused by thermal mismatch, for example. Now that the substrate and the thin film are joined, the external forces stay applied (Fig.A.5(α)). The position of the neutral plane depends on the distribution of the biaxial Young's moduli in the system. The external forces or the corresponding moment, respectively, produce the same stress distribution as in (a) and prevent the system from bending. Therefore system (α) is called "straightened system". This is the preferred description in terms of the calculation procedure.

System (b) consists of the same materials and has the same dimensions as system (α) (Fig.A.5(b)). Initially when the substrate and thin film are joined, external forces are not applied. System (b) is therefore stress free and plane. The position of the neutral plane is the same as in (α). Now external forces with the same magnitude but opposite sense as in (a) and (α) are applied as depicted in Fig.A.5(β). This pair of forces or the corresponding bending moment, respectively, bend the system about the neutral plane and produce a characteristic stress distribution σ_β, which is calculated from the biaxial Young's moduli E_b and the curvature κ as a function of z (Eq. (A.1)):

$$\sigma_\beta = -E_b \kappa z \tag{A.1}$$

Coated systems that bend owing to internal residual stresses, such as the cantilever or the initial system, are described by superimposing the forces and stresses of systems (α) and (β) (Fig. 5(γ)). The external forces of (α) and (β) cancel each other out, and the stresses are added. Because in this case bending is not inhibited by external forces, this system is denominated a "relaxed system". Identical curvature and stress distribution are obtained when system (b) is subjected to the same temperature that caused the length difference in system (a).

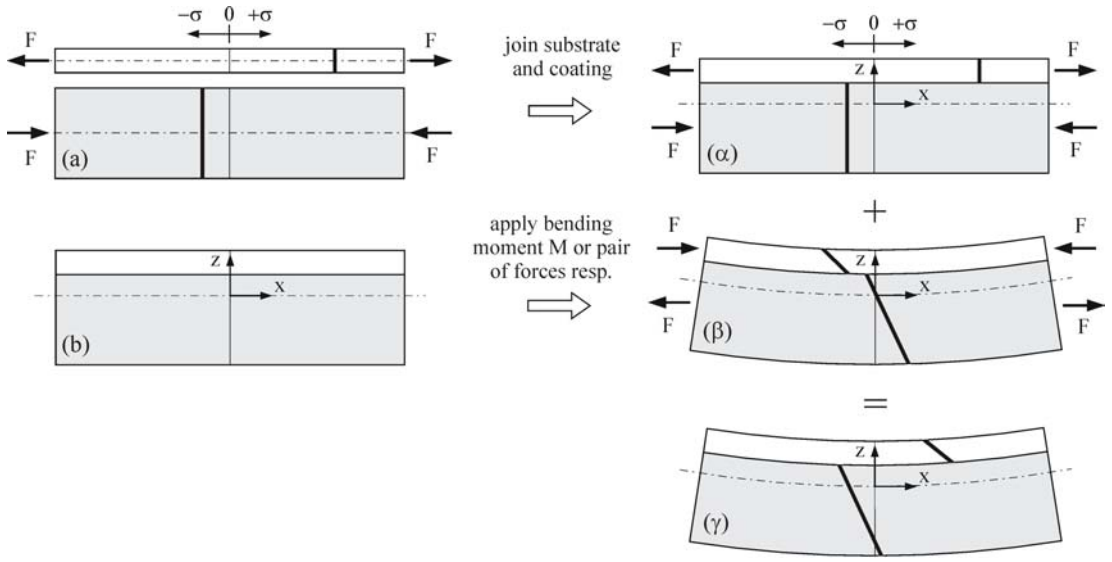

Figure A.5: System (a): Balanced external forces are applied on the separated coating and substrate to produce a certain stress distribution. To obtain the "straightened system" (α), substrate and coating are joined, the external forces stay applied. System (b) is initially stress free. External forces are applied to bend system (β). The superposition of the stresses and forces of (α) and (β) leads to the "relaxed system" (γ).

A.4.2 Calculation of the Curvature in Section A as a Function of Cantilever Thickness

First the curvature of section B κ_b which acts as a curved indicator that amplifies the curvature of section A, is determined. It is calculated from the lengths of the sections A and B (l_A and l_B) and the deflection of the original cantilever $\delta_{original}$ by solving Eq. (A.2) numerically for κ_B:

$$\delta_{original} = \frac{1}{\kappa_b}\left[1 - \cos\left(\left(l_A + l_B\right)\kappa_B\right)\right] \tag{A.2}$$

Now the curvature of section A κ_A is determined as a function of the actual cantilever thickness t. It is calculated from the actual deflection $\delta\,(t)$ (Fig.A.4), the lengths of the sections A and B and the determined κ_B. To obtain the curvature of section A, Eq. (A.3) is solved numerically for κ_A. Because the curvature of section A depends on the cantilever thickness, Eq. (A.3) must be solved for each step of the gradual thickness reduction:

$$\delta = \frac{1}{\kappa_A}\left[1 - \cos\left(l_A\kappa_A\right)\right] + \sin\left(l_A\kappa_A + \frac{l_B\kappa_B}{2}\right)\frac{2}{\kappa_B}\sin\left(\frac{l_B\kappa_B}{2}\right) \tag{A.3}$$

For the present example, the resulting curvature of section A as a function of the actual cantilever thickness is depicted in Fig.A.6.

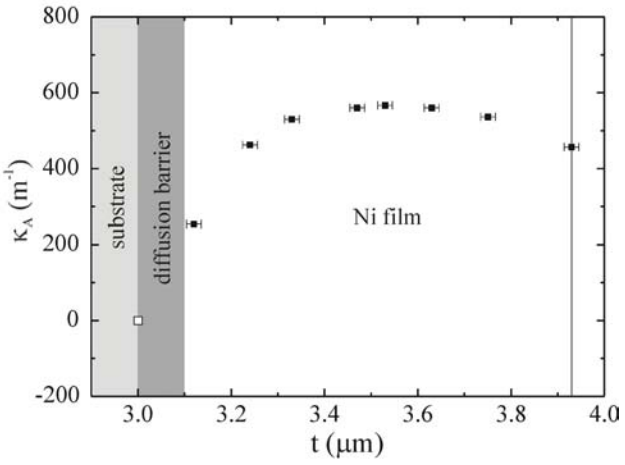

Figure A.6: Curvature of section A κ_A as a function of the cantilever thickness t. The experimentally determined curvatures (■) and the predicted curvature for the uncoated plane substrate (□) are drawn in.

A.4.3 Calculation of the Stress Distribution in Section A of the Cantilever

The stress distribution in section A is determined by superimposing the previously removed sublayers step by step and correlating the actual mean stresses in the sublayers with the corresponding curvatures. There are different ways to calculate the stresses in the removed volumes; a relatively simple one is presented here. For the subsequent calculations, straightened section A is considered.

First, the use of subscripts of the variables is explained, as the stresses, forces, moments and dimensions refer to either one individual sublayer or to more than one superimposed sublayers.

A force, that is applied to one individual sublayer, for example, is described by means of a variable with the subscript i written in square brackets, $F_{[i]}$, where $[i]$ indicates the position of the individual sublayer. The numeration starts with the substrate ($[i] = 0$), the first superimposed sublayer has the subscript $[i] = 1$, etc.

A force that is applied to a composite consisting of a certain number of superimposed sublayers, for example, is described by means of a variable with a subscript without brackets , F_i. In this case, the force acts in the cross section from the substrate ($i = 0$) up to sublayer i.

The necessary in-plane biaxial Young's moduli E_b of Si⟨100⟩, sublayer 1 and the Ni film are listed in Table A.1. E_b is calculated from the bulk Young's modulus E by means of the equation $E_b = E/(1-\nu)$ with $\nu = 0.3$. Owing to the discontinuous structure of the diffusion barrier, sublayer 1 (consisting ideally of the $100nm$ thin diffusion barrier and $20nm$ Ni) is regarded as a composite with one biaxial Young's modulus $E_{b,[1]}$. It takes into account the biaxial moduli of Ni, SiO_x, SiN_x, and nickel silicides.

Table A.1: Biaxial Young's moduli of Si⟨100⟩, sublayer 1 and Ni$\langle 2\overline{11}\rangle$, which is the cristallographic direction parallel to the Ni film surface.

$E_{b,Si\langle 100\rangle}$ (GPa)	$E_{b,[1]}$ (GPa)	$E_{b,Ni\langle 2\overline{11}\rangle}$ (GPa)
180.6[7]	150	334[8,9]

Step $i = 0$: Uncoated Substrate

The calculation starts with the uncoated substrate, denominated sublayer i (Fig.A.7(a)). It consists of pure single crystalline Si, is stress free and plane. This corresponds to the curvature $\kappa_{[i]} = 0$, the bending moment $M_{[i]} = 0$ and the uniform stress distribution $\sigma_{[i]}(z) = 0$. The coordinate system is chosen so that $z = 0$ in the neutral plane. The neutral plane is located in the middle of the cross-section of the substrate.

Step $i = 1$: Substrate and Sublayer 1

Now sublayer i (thickness $t_{[i]}$) is superimposed on the substrate (Fig.A.7(b)). In the present example, it consists of a composite material with the biaxial Young's modulus $E_{b,[1]} = 150GPa$. Owing to the superposition of sublayer i, the position of the neutral plane changes. It depends on the arrangement, thicknesses and biaxial Young's moduli of the substrate and sublayer i. The distance of the neutral plane from the bottom of the cantilever h_i is calculated from Eq. (A.4) under the condition that $z = 0$ in the neutral plane:

$$\int E_b(z)\, z dz = 0 \tag{A.4}$$

The curvature that corresponds to the thickness of the actual relaxed system κ_i is caused by the bending moment M_i calculated from Eq. (A.5) in consideration of the current position of the neutral axis. κ_i is taken from the experimentally determined values (Fig.A.6):

$$M_i = \kappa_i \int E_b(z)\, z^2 dz \tag{A.5}$$

For convenience, the bending moment M_i is divided into two parts (Eq. (A.6)):

$$M_i = M_{i-1} + M_{i-1,i} \tag{A.6}$$

M_{i-1} is produced by the stress distribution σ_{i-1} (Eq. (A.7)):

$$M = \int \sigma(z)\, z dz \tag{A.7}$$

In the actual example, $M_{i-1} = 0$ as described in the previous step (Fig.A.7(a)). $M_{i-1,i}$ is calculated from Eq. (A.6)). It is caused by the additional stress distribution $\sigma_{i-1,i}$, which consists of the stresses in the superimposed sublayer and the corresponding balanced stress in the system $i - 1$ (Fig.A.7(c)). Those homogeneously distributed stresses in the individual sublayers are produced by the external forces $F_{[i-1,i]}$ and $-F_{[i-1,i]}$. In

the present example, system $i-1$ consists of Si and exhibits compressive stress caused by $-F_{[i-1,i]}$. Sublayer i consists of the diffusion barrier and Ni and is subjected to tensile stress caused by $F_{[i-1,i]}$. The stress distribution $\sigma_{i-1,i}$ consists of two parts: the stress in sublayer i, $\sigma_{i-1,i} = F_{[i-1,i]}/t_{[i]}$, and the stress in system $i-1$, $\sigma_{i-1,i} = -F_{[i-1,i]}/t_{[i-1]}$. $\sigma_{i-1,i}$ is calculated from Eq. (A.7) with regard to $M_{i-1,i}$ and the current position of the neutral plane.

The total stress distribution σ_i in the actual system is calculated by adding σ_{i-1} and $\sigma_{i-1,i}$. The resulting stress profile as well as the applied bending moment that compensates for σ_i and straightens the system $M_{i,s} = -M_i$ are depicted schematically in Fig.A.7(d).

Subsequent Steps

The calculation procedure for the following steps ($i = 2-8$) is similar to the procedure described in the previous step ($i = 1$). First, sublayer i with thickness $t_{[i]}$ is superimposed on the system $i-1$. In the present example, sublayers $i = 2-8$ consist of pure Ni. The position of the neutral plane changes to h_i according to the thicknesses of the superimposed sublayers and the corresponding biaxial Young's moduli (Eq. (A.4)). The current system is depicted for $i = 2$ in Fig.A.7(e).

The curvature that corresponds to the thickness of the actual relaxed system κ_i is taken from Fig.A.6. It is caused by the bending moment M_i calculated from Eq. (A.5) with regard to the actual position of the neutral plane. M_i is divided into two parts (Eq. (A.6)).

M_{i-1} is produced by the already calculated stress distribution σ_{i-1} (Eq. (A.7)). $M_{i-1,i}$ is determined from Eq. (A.6). The stress distribution $\sigma_{i-1,i}$ or the corresponding forces, respectively, are calculated from Eq. (A.7) with regard to $M_{i-1,i}$, and the actual position of the neutral plane in consideration of the following assumptions:

1. $M_{i-1,i}$ is caused by the additional stress distribution $\sigma_{i-1,i}$ which consists of the stresses in the superimposed sublayer i and the corresponding balanced stress in system $i-1$. These stresses are produced by the external forces $F_{[i-1,i]}$ (sublayer i) and $-F_{[i-1,i]}$ (system $i-1$), respectively. The forces induce uniform strain distributions in sublayer i and system $i-1$.

2. The biaxial composite Young's modulus that is necessary for the calculation of the uniform strain in the system $i-1$, $E_{b,c,i-1}$, is calculated from Eq. (A.8). In the present example, system $i-1$ consists of the Si substrate and the composite sublayer for $i = 2$ and of the Si substrate, the composite sublayer 1 and the Ni sublayer(s) for $i > 2$:

$$E_{b,c,i-1} = \sum_{j=0}^{i-1} \frac{t_{[j]} E_{b,[j]}}{\sum_{j=0}^{i-1} t_{[j]}} \tag{A.8}$$

3. The corresponding stresses in sublayer i and system $i-1$ are calculated from Hooke's Law with the biaxial Young's moduli of the particular sublayers.

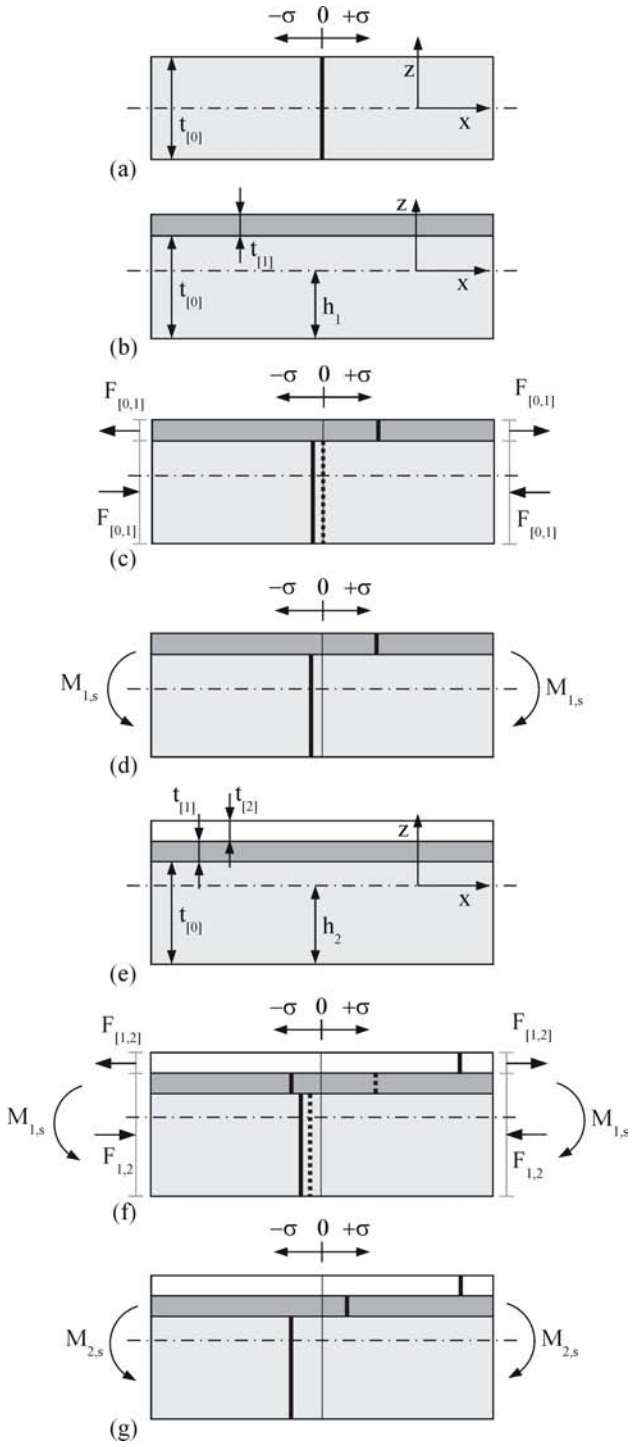

Figure A.7: Schematic description of the calculation procedure. (a) $i = 0$: Uncoated stress free substrate, $\sigma_{[i]} = 0$ (black line). (b) $i = 1$: the superposition of sublayer i shifts the neutral plane. (c) $i = 1$: σ_{i-1} (dashed line) corresponds to the stresses in the system $i - 1$. $\sigma_{i-1,i}$ (black line) is produced by the external forces. (d) $i = 1$: addition of σ_{i-1} and $\sigma_{i-1,i}$. The actual system is straightened by the moment $M_{i,s}$, which compensates for σ_i. (e) $i = 2$: superposition of sublayer i. (f) $i = 2$: σ_{i-1} (dashed line) is produced by $M_{i-1,s}$ and corresponds to the stresses in system $i - 1$. $\sigma_{i-1,i}$ (black line) is produced by the balanced external forces $+F_{[i-1,i]}$ and $-F_{[i-1,i]}$. (g) $i = 2$: addition of σ_{i-1} and $\sigma_{i-1,i}$. The actual system is straightened by the bending moment $M_{i,s}$, which compensates for σ_i.

The actual stress distributions σ_{i-1} and $\sigma_{i-1,i}$ are depicted in Fig.A.7(f). The total stress distribution in the actual straightened system σ_i is calculated by adding σ_{i-1} and $\sigma_{i-1,i}$. The resulting stress profile as well as the moment that compensates for σ_i and straightens the system $M_{i,s} = -M_i$ are depicted schematically for $i = 2$ in Fig.A.7(g).

The calculation procedure is repeated until all sublayers are superimposed and the cantilever has attained its original thickness. The resulting stress profile in the straightened original cantilever is shown in Fig.A.8.

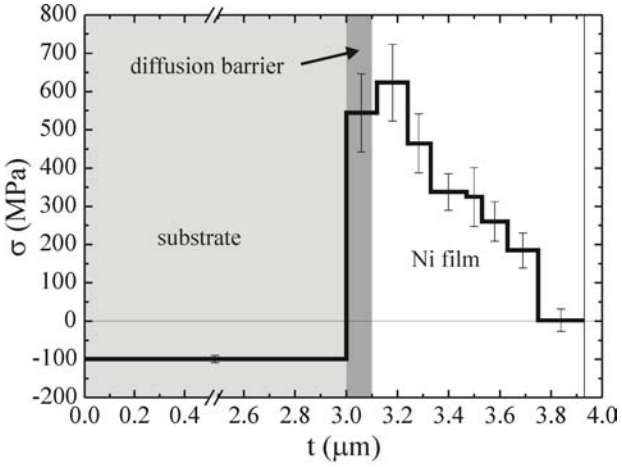

Figure A.8: Stress profile in the straightened cantilever as a function of the cantilever thickness.

A.4.4 Determination of the Stress Distribution in the Initial System

The stress profiles in the initial system and the straightened cantilever are different, but they can be converted into each other. The stress profile in the initial system is calculated from the stress distribution and the thickness of the straightened cantilever and the substrate thickness of the initial system.

First, the straightened cantilever is considered (Fig.A.9(a)). Then the eight sublayers and the substrate are separated (Fig.A.9(b)), and the bending moment that straightens the system $M_{8,s}$ is substituted by nine external forces $F_{[i]}$, with $0 < i < 8$, calculated from the thicknesses $t_{[i]}$ and the stresses in the single sublayers of the straightened cantilever $\sigma_{[i,sc]}$ (Eq. (A.9):

$$F_{[i]} = \sigma_{[i],sc} t_{[i]} \tag{A.9}$$

These balanced forces serve two purposes. They ensure that the lengths of the separated parts are the same as in the straightened cantilever l_{sc}, and induce the same stress distribution as the moment $M_{8,s}$.

Now the external forces are removed and the sublayers as well as the substrate extend or contract until they are stress free (Fig.A.9(c)). The lengths of the separated parts $l_{[i],stressfree}$ depend on the length of the straightened cantilever, the biaxial Young's moduli and the magnitude of the removed external forces or stresses, respectively (Eq. (A.10)):

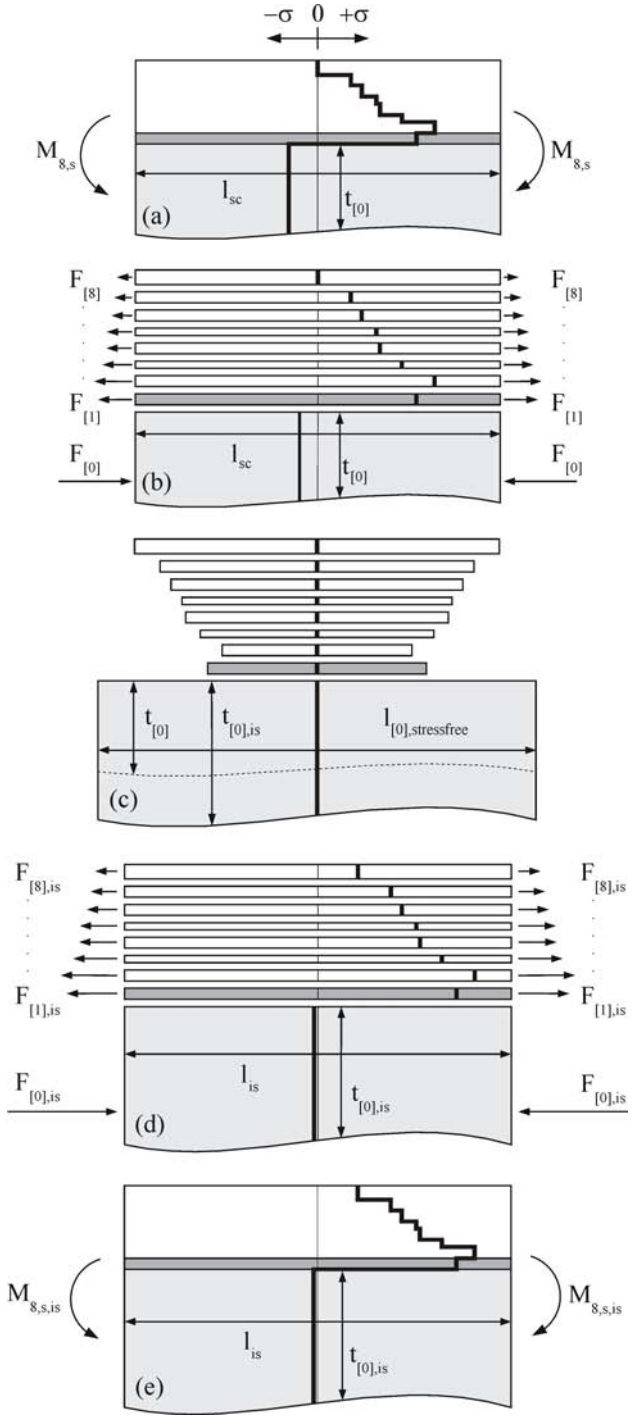

Figure A.9: (a) Stress distribution in the straightened cantilever. (b) The sublayers and the substrate are separated and external forces are applied. (c) The external forces are removed and the separated parts expand or contract. The substrate is set to the thickness of the initial system. (d) External forces are applied to adjust the lengths of the separated parts and produce the actual stress distribution. (e) The parts are joined and the external forces are substituted by the corresponding bending moment which straightens the system. This leads to the stress distribution in the straightened initial system.

$$l_{[i],stressfree} = \frac{l_{sc}}{\frac{\sigma_{[i],sc}}{E_{b,[i]}} + 1} \tag{A.10}$$

Now the substrate thickness is set to the thickness of the initial system $t_{[0],is}$ (Fig.A.9(c)). External forces $F_{[i],is}$ are applied on the separated parts of the initial system (Fig.A.9(d)). These balanced forces adjust the dimensions of the separated parts of the initial system so that all parts have the same length l_{is}, the length of the initial system. In the present example, the nine external forces and the length are calculated by solving a system of equations that consists of nine Eq. (A.11), with $0 < i < 8$, and the equation for the force balance (Eq. (A.12)):

$$F_{[i],is} = t_{[i],is} E_{b,[i]} \frac{l_{is} - l_{[i],stressfree}}{l_{[i],stressfree}} \tag{A.11}$$

$$\sum_{i=0}^{i=8} F_{[i],is} = 0 \tag{A.12}$$

Now the separated parts are joined (Fig.A.9(e)). The calculated external forces are substituted by the bending moment $M_{8,s,is}$, which straightens the initial system and produces the corresponding stress profile. Finally, the bending moment is removed and the system relaxes. The resulting stress distribution in the relaxed initial system is depicted in Fig.A.10.

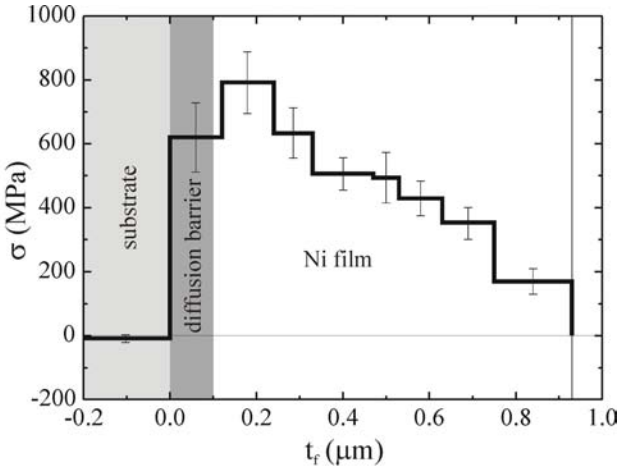

Figure A.10: Stress profile in the Ni film of the relaxed initial system. It is obtained by removing the moment $M_{8,s,is}$ from the straightened initial system.

A.5 Remarks on the Determined Stress Distribution

The stress distribution determined shows a large stress gradient in the Ni film. The stress increases towards the Ni-SiN_x interface, reaches a maximum value of $792 \pm 103 MPa$ and drops to an average stress of $620 \pm 110 MPa$ in the diffusion barrier. It must be pointed out that the actual stress in the diffusion barrier can differ significantly from the determined

mean stress owing to the discontinuous structure of the SiN_x and SiO_x layers and the simplification that this sublayer consists of one material with a mean Young's modulus. The average stress in the Ni film (the diffusion barriers are not taken into account) is $460 \pm 60MPa$. This value agrees well with wafer curvature experiments that show a mean stress of $581MPa \pm 10\%$.[6] It must be taken into account that those measurements were performed one year prior to the cantilever experiments and that the stresses in the Ni film relax at room temperature.

Although the average stresses match well, one would expect a constant residual stress caused by the annealing treatment after the fabrication from simple continuum plasto mechanics point of view. The reason for the observed gradient can be explained by considering two different dislocation arrangements.

In order to realize a constant stress distribution in the Ni film, the geometrically necessary dislocations, which produce the plastic relaxation during cooling from annealing to room temperature, should be located at the interface (Fig.A.11(a)). The determined stress distribution leads to the conclusion that this is not the case for the investigated system. A probable arrangement of geometrically necessary dislocations that produces the observed stress gradient in the thin film is depicted schematically in Fig.A.11(b).

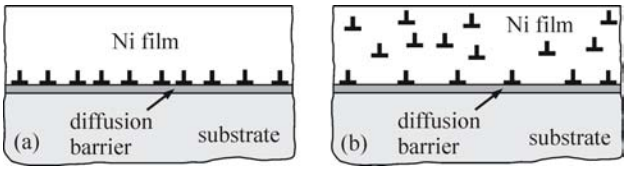

Figure A.11: A dislocation distribution as depicted in (a) leads to a uniform stress distribution. The experimentally determined stress gradient could be caused by a dislocation arrangement, as sketched in (b).

Concerning the correctness of the ILR method, it is essential to investigate whether the determined stress gradient is real or an artefact caused by ion damage, plastic deformation or relaxation of the thin film due to the fabrication process of the cantilever or the actual experiment. To verify the stress profile obtained, a modified cantilever experiment was performed.

First, a cantilever with the same dimensions as in the previously presented first experiment is fabricated. Subsequently, the cantilever thickness is reduced from bottom-up in section A, which affects the stress distribution in the cantilever, and the corresponding deflection is measured (Fig.A.12(a) and (b)). Calculations were performed to predict the deflection as a function of the bottom-up reduced cantilever thickness by assuming the previously determined stress distribution.

The comparison of the calculated and the experimentally measured deflections gives information about the degree of ion damage or plastic deformation (Fig.A.13).

The experimental values correlate well with the calculated deflections, which supports the determined stress distribution and leads to the conclusion that neither ion damage nor plastic deformation or relaxation affects the stress profile significantly. Nevertheless, the systematic and statistical errors as well as possible errors due to ion damage or plastification, which may influence the stress distribution in the investigated volume to a certain extent, are discussed.

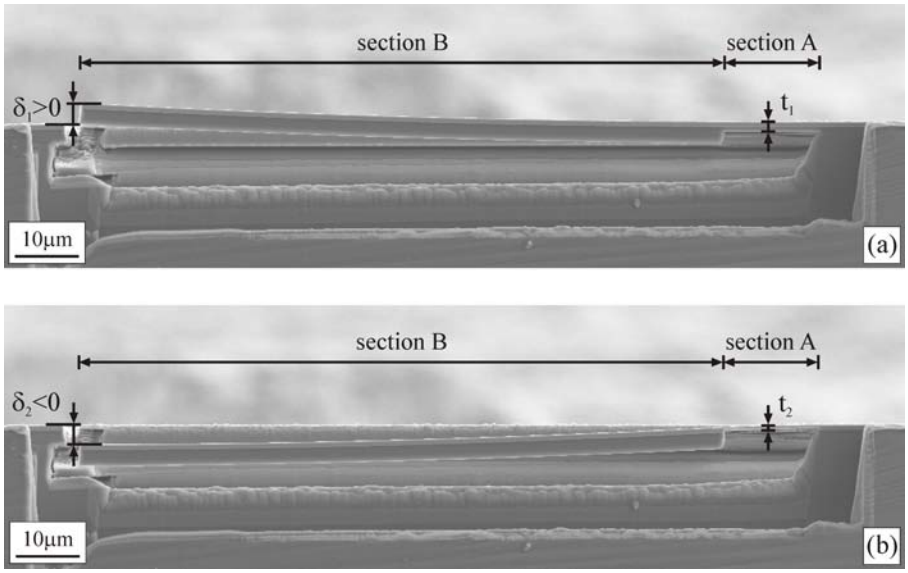

Figure A.12: SEM-images of the Ni-coated cantilever (front view). As depicted in (a), the partially removed substrate in section A leads to a positive deflection δ_1 of the cantilever. In (b) the whole substrate and parts of the Ni film are removed. This leads to a negative deflection δ_2.

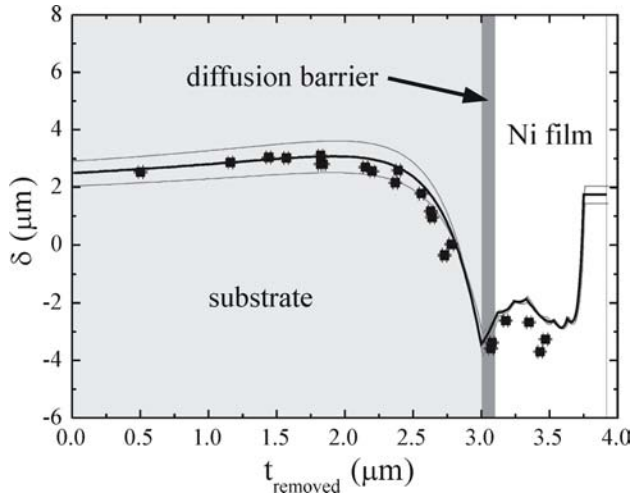

Figure A.13: Deflection of the cantilever δ as a function of the thickness of the bottom-up removed material in section A, $t_{removed}$. The experimentally determined deflections (■) are compared with the values calculated from the previously determined stress distribution (black line). The grey lines represent the upper and lower bound for the deflections, are calculated from the determined stress distribution plus/minus the standard deviation.

A.6 Discussion of Possible Sources of Error

A.6.1 Systematic and Statistical Errors

Systematic errors that can be caused by insufficient calibration of the SEM and statistical errors that are caused by inaccurate measurements or inappropriate choice of Young's moduli influence the accuracy of the result. In the present example, the systematic errors are neglected because the SEM was calibrated well and therefore, the statistical errors are dominant. For the calculation of errors of the stress distribution in the straightened cantilever and the initial system, the following values for the standard deviations ΔX of the input parameters X are assumed: $\Delta t_{[1-8]} = 15nm$ for the thickness of the individual sublayers; $\Delta t_{[0]} = 150nm$ for the thickness of the substrate; $\Delta \delta_{[0-8]} = 10nm$ for the measured deflections; $\Delta l_A = 200nm$ and $\Delta l_B = 300nm$ for the lengths of sections A and B; $\Delta E_{[0]} = 18GPa$ for the Young's modulus of the Si substrate; $\Delta E_{[1]} = 30GPa$ for the Young's modulus of sublayer 1; and $\Delta E_{[2-8]} = 40GPa$ for the Young's modulus of the Ni sublayers 2 - 8.

Here, the authors are considering only the errors for this special experiment. A more general analysis of the errors will be presented in a forthcoming paper. Generally, it must be pointed out that the statistical errors can be reduced by dividing the thin film into fewer sublayers, which improves the ratio $\frac{t_{sublayer}}{\Delta t_{sublayer}}$ at the expense of a reduction in the resolution of the stress profile. In other words, a decreasing spatial resolution leads to an increase in accuracy.

For the system presented, a mean sublayer thickness of about $120nm$ is a good compromise between resolution and accuracy.

A.6.2 Remarks to Ion Damage

Ion damage cannot be avoided when working with a focused ion beam workstation. Damage caused by implanted Ga ions is difficult to quantify, but it has a certain influence on the mechanical properties and the residual stress field in the affected volume. Investigations have shown that the ion implantation depth generally depends on the ions and materials involved, the acceleration voltage, the incident angle, and the ion current.[10]

Stopping and range of ions in matter (SRIM)[11] simulations were performed to estimate the implantation depth of the Ga ions. For an acceleration voltage of $30kV$ and ion incidence almost parallel to the surface, the simulations show maximum Ga penetration depths of about $20nm$ in Ni and $30nm$ in Si, which is small compared to the thickness of the individual sublayers. Additionally, it must be taken into account that ion damage occurs at the top as well as the bottom of the cantilever, and ion-induced compressive stresses may partially cancel each other out. The damage can be neglected, especially when similar materials are involved at the top and the bottom of the cantilever.

A.6.3 Remarks to Plastic Relaxation of the Ni Film During the Experiment

The calculation procedure assumes linear elastic behavior of the system. In case of plastic relaxation during the experiment, the developed calculation procedure usually leads to an underestimation of the residual stresses in the initial system. Therefore, it is essential

to take a closer look on the stresses in the thin film during the annealing process and the actual cantilever experiment.

The film was annealed at $600°C$ to obtain a nearly stress-free state. On cooling to room temperature, the thermal stress in the Ni film according to the coefficients of thermal expansion ($\alpha_{Si} = 2.6 \times 10^{-6}K^{-1}$ and $\alpha_{Ni} = 16 \times 10^{-6}K^{-1}$)[12,13] should be $1330MPa$, which is significantly greater than the experimentally determined mean stress. Those high stresses are reduced by plastic relaxation in the thin film, which leads to the determined stress distribution.

However, during the fabrication of the cantilever and the subsequent gradual reduction in the film thickness, the stress distribution in the thin film changes and additional plastic deformation could be the result.

A closer look at the stress distribution of the relaxed cantilever shows that the maximum stress of $620 \pm 87MPa$ appears during the reduction of the Ni film thickness when the majority of the thin film is removed (Fig.A.14). The minimum stress of about $-300 \pm 20MPa$ is found for a film thickness of about $650nm$. Although the maximum and minimum stresses that appear in the Ni film during the experiment are not negligible, they are lower than the maximum stress in the initial system ($792 \pm 103MPa$). Furthermore, the calculated and the measured deflections of the second cantilever experiment, in which the cantilever thickness is reduced bottom-up, would not correlate if notable plastic relaxation occurred. This leads to the conclusion that a significant change in the stress field due to plastic deformation does not take place during the experiments.

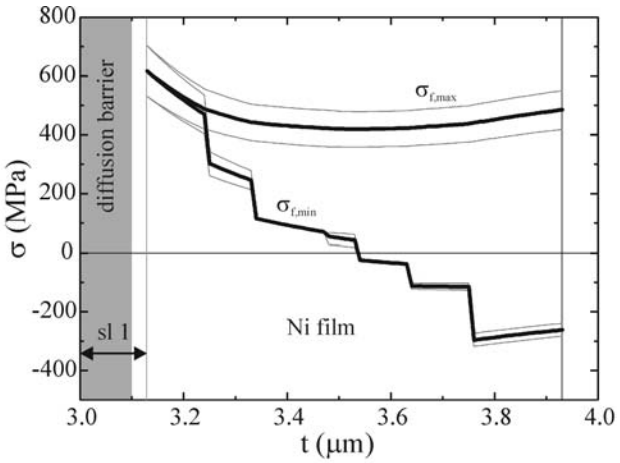

Figure A.14: Minimum and maximum stresses $\sigma_{f,min}$ and $\sigma_{f,max}$ (black lines) in the Ni film of the relaxed cantilever, which occur during the top-down removal of the sublayers, as a function of the cantilever thickness. The grey lines represent the upper and lower bound for the minimum and maximum stresses calculated from the determined stress distribution in the initial system plus/minus the standard deviation. The stresses in sublayer 1 (sl 1) are not evaluated, because it is regarded as a composite material with one biaxial Young's modulus.

Finally, it should be noted that in critical cases, the choice of an adequate cantilever thickness can be used to reduce the stresses in the thin film and avoid plastic relaxation.

A.7 Comparison of the ILR Method With Other Techniques

A large number of techniques, such as the wafer curvature method,[1–3] microcantilever techniques[14–17] and methods that are based on optical interferometry[18,19] have been developed to determine average stresses or simple stress gradients in thin films. Most methods use the original Stoney's equation or modifications to determine the residual stresses.

Besides the developed ILR method, the only existing technique that permits the determination of complex depth profiles of residual stresses on a nanoscale is the grazing incidence X-ray scattering (GIXS) method.[5] Although the GIXS method is non-destructive, the advantages of the ILR method are the lateral resolution of a few micrometers, the straight-forward calculation procedure and the possibility of investigating stress profiles in amorphous thin films.

The method developed by Kang et al.,[20] which detects the stress-induced relaxation of the film in the vicinity of a FIB-fabricated slot, allows the investigation of residual stresses in amorphous as well as crystalline thin films. Theoretically, this technique can be used to determine depth profiles of residual stresses, but this capability has yet to be demonstrated.

Similar methods, although on the micrometer or millimeter scale, respectively, are the hole drilling strain-gage and the incremental hole drilling method.[21,22]

A.8 Conclusion

The FIB-based ILR method is a useful tool for determining residual stress profiles in near-surface regions on a nanoscale. The calculation and experimental procedure developed can be used for arbitrary combinations of crystalline or amorphous layered materials. To ensure linear elastic behavior of the material(s), the thickness of the cantilever should be adapted to the actual materials and the estimated mean stresses. The influence of ion damage due to FIB fabrication and the plastic relaxation in the presented Ni/Si system was evaluated. This evaluation showed that the stress profile in the thin Ni film was not significantly affected.

A.9 Acknowledgements

The authors thank the Austrian Science Foundation FWF for supporting this work and G. Dehm, F.D. Fischer, T. Antretter, D. Kiener, W. Ecker and K.J. Martinschitz for helpful discussions.

Bibliography to paper A

[1] Eiper E, Martinschitz KJ, Keckes J. Powder Diffr 2006;21:25.

[2] Resnik D, Aljancic U, Vrtacnik D, Mozek M, Amon S. Vakuum 2005;80:236.

[3] Dieing T, Usher BF. Phys Rev B 2003;67:054108.

[4] Noyan IC, Cohen JB. Residual Stress. New York: Springer-Verlag;1987.

[5] Genzel C. Materials Science and Technology 2005;21:10.

[6] G Dehm. Private communication.

[7] Freund LB, Suresh S. Thin Film Materials. Cambridge University Press;2003, p.244.

[8] Stüwe HP. Mechanische Anisotropie. Vienna: Springer-Verlag;1974, p.44.

[9] Kittel C. Einfhrung in die Festkrperphysik. Munich: R. Oldenbourg-Verlag;1969, p.160.

[10] Kiener D, Motz C, Rester M, Jenko M, Dehm G. Mater Sci Eng A 2007;459:262.

[11] Ziegler JF, Biersack JP, Littmark U. The Stopping Range of Ions in Matter. New York: Pergamon Press;1985, p. 321.

[12] Hellwege KH. Landolt-Börnstein. Springer-Verlag;1982.NS III:17a, p. 62.

[13] Hellwege KH, Madelung O. Landolt-Börnstein. Springer-Verlag;1986.NS III:19a, p. 245.

[14] Baek CW, Kim YK, Ahn Y, Kim YH. Sens Actuators A Phys 2005;117:17.

[15] McCarthy J, Pei Z, Becker M, Atteridge D. Thin Solid Films 2000;358:146.

[16] Lemoine P, Zhao JF, Bell A, Maguire P, McLaughlin J. Diamond Relat Mater 2001;10:94.

[17] Cardinale GF, Howitt DG, Clift WM, McCarthy KF, Medlin DL, Mirkarimi PB, Moody NR. Thin Solid Films 1996;287:214.

[18] Tamulevicius S, Kopustinskas V, Meskinis S, Augulis L. Carbon 2004;42:1085.

[19] Tien CL, Lee CC, Tsai YL, Sun WS. Opt Commun 2001;198:325.

[20] Kang KJ, Yao N, He MY, Evans AG. Thin Solid Films 2003;443:71.

[21] Rendler NJ, Vigness I, Exp Mech 1966;6:577.

[22] Santana YY, La Barbera-Sosa JG, Staia MH, Lesage J, Puchi-Cabrera ES, Chicot D, Bemporad E. Surf Coat Technol 2006;201:2092.

B

Stress Measurement in Thin Films with the Ion Beam Layer Removal Method: Influence of Experimental Errors and Parameters

S. Massl[a], H. Köstenbauer[a,b], J. Keckes[c] and R. Pippan[a]

[a] Erich Schmid Institute of Materials Science, Austrian Academy of Sciences, A–8700 Leoben, Austria
[b] Department of Physical Metallurgy and Materials Testing, University of Leoben, A–8700 Leoben, Austria
[c] Department Materials Physics, University of Leoben, A–8700 Leoben, Austria

Abstract

The recently developed ion beam layer removal method[1] allows the precise determination of complex depth profiles of residual stresses in crystalline and in amorphous thin films on a nanoscale. Recipes and advice for optimal experimental design are given to minimize errors in the stress distributions calculated. The calculation procedure of this method is briefly introduced followed by the definition of any sources of error along with their influence on the resulting stress distribution. Finally, the errors as a function of experimental parameters are discussed by means of an example and four model stress distributions.

B.1 Introduction

Residual stresses and their distribution in thin films and structural elements in near-surface regions have been a field of intensive investigation because they are essential for the mechanical performance, the structural integrity and the lifetime of coated components. Such stresses are usually caused by thermal mismatch, the fabrication process or the applied load.

A number of methods have been developed for determining the average residual stresses in thin films. This is only useful when the residual stresses are distributed homogeneously. The mean stress is determined either directly by measuring the curvature of the coated system,[2–4] or indirectly by calculating the film stress from the lattice strain determined by means of X-ray diffraction and the elastic constants of the film material.[2,5] Often, residual stresses are not distributed uniformly across the film thickness as a consequence of the growth process, thermal loading or the mechanical treatment. Such depth profiles can be determined by grazing incidence X-ray techniques,[6] which achieve depth resolution on a nanoscale. However, these techniques can only be applied to crystalline materials and measure the stresses indirectly. Furthermore, the lateral resolution is limited to values $> 100\mu m$ owing to the grazing incidence of the X-rays and beam diameters of at least $1\mu m$.

Recently, a direct technique that allows the determination of complex depth profiles of residual stresses on a nanoscale called the ion beam layer removal method (ILR method), has been proposed.[1] It is based on measuring the deflection of a focused ion beam (FIB) workstation-fabricated micro cantilever beam as a function of the gradually reduced film thickness. This reproducible method can be applied to crystalline and amorphous materials.

Subsequently, ILR method is described briefly and the errors that influence the calculated stress distribution are then analyzed in detail. General guidelines for optimizing the experimental procedure are suggested and the advantages as well as limitations of the measures proposed for the minimization of errors are discussed.

B.2 Brief Description of the ILR Method

The ILR method allows the determination of depth profiles of residual stresses in crystalline and amorphous thin films. Such a residually stressed system induces a certain curvature depending on the stresses, the layer and substrate thicknesses, as well as the Young's moduli of the materials involved. Here, the ILR method is described with a $1.16\mu m$ TiN film on a $450\mu m$ thick (100) Si substrate. The thin film was deposited at $550°C$ by means of reactive sputtering from a Ti target in an $Ar + N_2$ atmosphere using an unbalanced DC magnetron sputtering system. The ILR method is based on the fabrication of a micro cantilever beam of adequate dimensions in $\langle 010 \rangle$ direction of the Si in the vicinity of the specimen edge by means of a dual beam FIB which combines an ion column and a scanning electron microscope (SEM). This cantilever consists of the a few microns thick substrate and the thin film and deflects owing to the redistributed residual stresses. In the presented example depicted in Fig.B.1, the cantilever deflects downwards due to the compressive stresses in the TiN film. In case of tensile stresses in the thin film, the cantilever would exhibit a positive (upward) deflection. The deflection is measured

from high magnification SEM images and corresponds to a certain curvature.

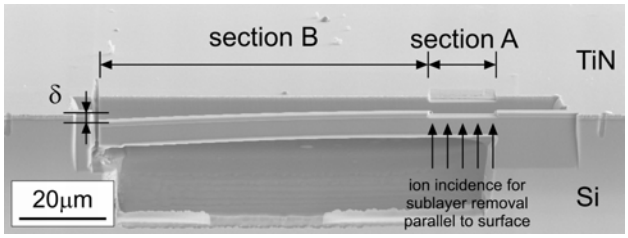

Figure B.1: Cantilever beam deflecting owing to compressive residual stresses in the thin film (inclined view). Then, the film is removed gradually in section A with the ion beam aligned parallel to the surface. This leads to a change of the curvature of section A amplified by section B, which acts as a curved indicator.

In order to measure the stress through the film, the thickness of the film thickness is reduced gradually from the top as with the ion beam aligned parallel to the sample surface as depicted in Fig.B.1. The thin material slices removed from the film in each step are called sublayers and the thickness of the individual sublayers is determined from the difference of the film thicknesses between two consecutive steps. The rest of the cantilever, section B, still has the curvature of the original cantilever and acts as a curved indicator that amplifies the curvature of section A. The reduction of the film thickness in section A affects the stress state in this part, leads to a shift of the neutral axis and changes the deflection of the cantilever. The curvature of section A as a function of cantilever thickness is calculated from the corresponding actual deflection and the curvature of the initial cantilever. The deflection and curvature as a function of film thickness depicted in Fig.B.2 is the basis for the calculation of the stress profile in the cantilever and the initial system.

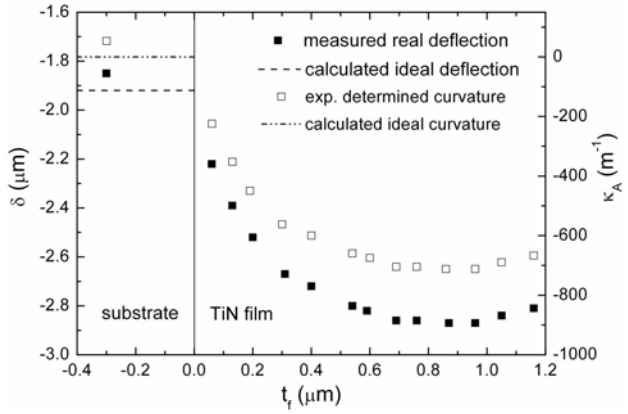

Figure B.2: Deflection of the cantilever obtained directly from SEM-images and calculated curvature of section A as a function of the actual film thickness. For comparison, the deflection and curvature calculated for the completely removed thin film ($t_f < 0$), which leads to a stress-free straight cantilever in section A, is drawn in.

The calculation procedure of the stress profile in the cantilever is based on the stepwise superposition of the previously removed sublayers in section A. To facilitate the evaluation procedure, the stresses of the actual straightened cantilever are used. This

eliminates the contribution of the curvature to the stress profile and leads to homogeneously distributed stresses in the substrate as well as in each of the superimposed sublayers.

The calculation procedure for the first two steps is depicted schematically in Fig.B.3. It starts with the uncoated substrate in section A, which is the last step of the of the sublayer removal procedure. At the beginning, the substrate is stress free and therefore straight as depicted in Fig.B.3(1a). When the first sublayer is superimposed, it leads to a shift of the neutral plane. At this point, the sublayer is not subjected to residual stresses and has no influence on the stress distribution in the substrate below (Fig.B.3(1b)). Now, system 1c is introduced. Having the same dimensions as system 1b, it is subjected to intrinsic residual stresses that consist of the stress in the sublayer and the corresponding balanced stress in the substrate. The magnitude of the residual stresses in 1c depends on the stresses in 1b and the curvature in 1d in a way that superimposing the systems 1b and 1c leads to the experimentally determined curvature of 1d. Step 2 starts with the system calculated in step 1d. The stress free sublayer 2 is superimposed, leading to a shift of the neutral axis as depicted in 2b. Then, system 2b is superimposed with system 2c, which is subjected to residual stresses in sublayer 2 and the corresponding balanced stresses in the system below consisting of the substrate and sublayer 1. As before, the superposition of 2b and 2c leads to the actual stress distribution 2d that results in the experimentally measured deflection or curvature, respectively.

The stress distribution in the initial cantilever is determined after superimposing the uppermost sublayer and completing the corresponding calculation procedure. The stress profile is described by a step function with step sizes corresponding to the thicknesses of the individual sublayers. Finally, the stress distribution in the initial system is calculated from the stress profile in the cantilever, since the stresses can be converted into each other as long as the materials involved exhibit linear elastic behaviour (Fig.B.4).

Possible explanations for such a depth profile of residual stresses could be a gradient of defects or a change in the microstructure. For comparison, the film stress was determined by means of the conventional wafer curvature technique and Stoney's equation, which lead to a mean film stress of $-1.21GPa$. This value is 21% smaller than the average stress obtained by means of the ILR method ($-1.53GPa$) and is considered as a fairly good agreement. It has to be taken into account that the biaxial Young's moduli $E_b = E/(1-\nu)$ have to be used in the calculation procedure of the ILR method to consider the 2D calculation procedure of a 3D problem. In the presented example, the bulk Young's moduli and Poisson's ratios of Si ($E_{Si(100)} = 130GPa \pm 5\%$, $\nu_{Si} = 0.28 \pm 0.01\%$) and TiN ($E_{TiN} = 309GPa \pm 24\%$, $\nu_{TiN} = 0.27 \pm 14\%$) are taken from literature.[7–22]

B.3 Discussion of Sources of Error

The stress distribution contains errors owing to ion damage, the finite accuracy in measuring the dimensions of the cantilever and the individual sublayers, the limited number of sublayers the thin film is divided into, as well as the uncertainty of the input material parameters. Additionally, an unfavourable choice of the cantilever thickness may lead to fracture or plastic relaxation of the layer or the substrate during the experiment which could lead to a wrong result and therefore has to be avoided. These sources of

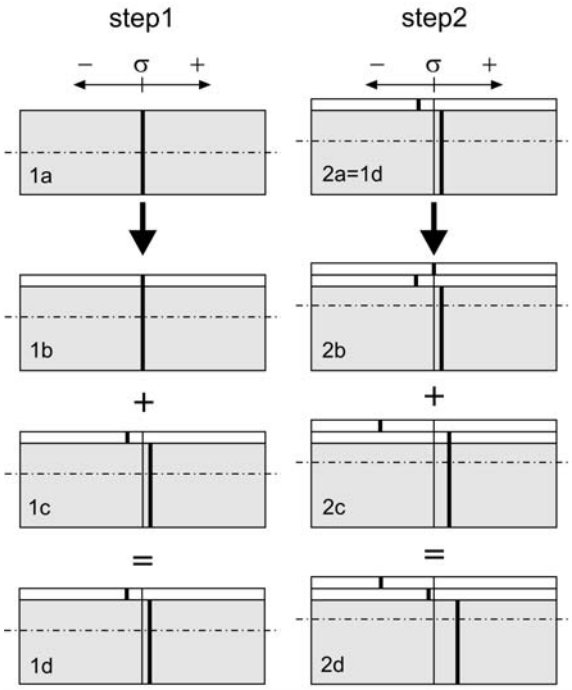

Figure B.3: The calculation procedure is described by means of the first two steps; each step starts with the balanced stress distribution of the previous step (a). Then, an unstressed sublayer is superimposed to obtain the composition of the current system (b). This leads to a shift of the neutral plane and a certain curvature. Now, an additional stress distribution (c) that consists of the stress in the superimposed sublayer and the corresponding balanced stress in the cantilever below is added. The stresses in (c) are chosen in such a way, that the addition of the stresses of (b) and (c) leads to the curvature and stress distribution of the current cantilever (d). The stress in each further sublayer superimposed is calculated in principle by the same procedure as applied in the second step.

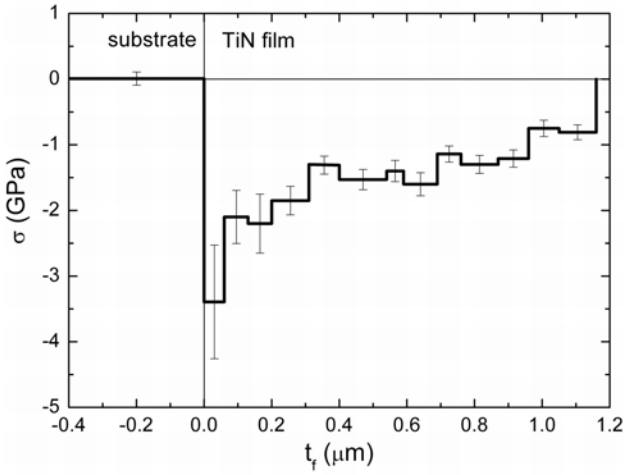

Figure B.4: Calculated stress distribution in the initial system. The thickness of each step of the step function corresponds to the thickness of the sublayers removed.

error and consequential general guidelines for a useful configuration of the experiment are discussed.

B.3.1 Ion Damage

Ion damage cannot be avoided when working with a FIB. Implanted ions change the mechanical properties of the material as well as the residual stress field as shown by Kim et al.,[23] and may therefore lead to notable errors. The amount of ion damage generally depends on the ions and materials involved, the acceleration voltage, the incident angle and the ion current.[24] The penetration depth can be estimated by means of a simple SRIM (the stopping and range of ions in matter)[25] simulation which takes into account the parameters mentioned above. The estimations show that for many ion-material combinations the implantation depth is between $10nm$ and $30nm$. This is small compared to the typical thickness of the individual sublayers and therefore, the ion induced changes of the stress distribution can usually be neglected. This assumption was confirmed by experimental findings, where cantilevers of different materials and thicknesses were irradiated with Gallium ions under various angles of incidence and with different ion currents. Measuring the deflections prior and after this experiment showed no measurable changes which leads to the conclusion that the ion beam-induced stresses can be disregarded in the materials investigated. Anyway, it is advisable to perform a SRIM simulation prior to the experiment. Additionally, it is necessary to check the literature if the ions and materials involved lead to grain boundary embrittlement, as it is the case for Ga ions and Al, for example, since such effects are not considered in the SRIM software.

A simple way to minimize ion damage is to use low ion currents and low ion energies for fine FIB cuts and to check the diameter and shape of the ion beam prior to cutting, since in case of insufficient calibration or outworn FIB apertures the beam dimensions are usually not well defined.

B.3.2 Real and Calculated Stresses in a Sublayer

The calculation procedure leads to a stress distribution in the thin film which is described by means of a step function as depicted in Fig.B.4. As a result of the calculation procedure, the stresses in each of the individual sublayers are constant and can be approximated well by the mean stresses in each sublayer as long as the curvature is not too large. The quality of the reproduction of the real stress profile by the step function depends among others on the shape of the real stress profile and the thicknesses of the individual sublayers the film is divided into.

In case of a relatively homogeneous stress distribution, the subdivision of the film into a few relatively thick sublayers will reproduce the real stress profile well. In case of a rugged stress distribution, it is not possible to reproduce the details by means of a few thick sublayers. Rather, a large number of thin sublayers ($\approx 80nm$) is favourable due to the increase in resolution of the stress profile. Nevertheless, it should be noted that the thickness of the individual sublayers can only be measured with finite accuracy. This leads to larger relative errors in thin sublayers and as a result to larger errors in the calculated sublayer stresses when thin sublayers are used. In other words, an increase of spatial resolution leads to an increase of errors of the stresses determined. This effect is explained in detail in section B.4 by means of four model stress distributions.

B.3.3 Accuracy of SEM Measurements

The SEM-measured dimensions, such as cantilever lengths, thicknesses and deflections contain certain errors due to technical and physical limitations of the microscope, systematic errors owing to insufficient calibration and unavoidable statistical errors.

Technical and physical limitations of the SEM lead to a decrease in image quality with increasing magnification. Generally, such limitations cannot be compensated, but optimal settings for the acceleration voltage, stigmation, working distance, magnification and the choice of an adequate aperture ensure best image quality possible. Systematic errors which result from insufficient calibration, lead to a general over or underestimation of measured lengths. They are not easy to detect and statistical analysis is not generally useful to quantify such errors. Therefore, a careful calibration of the SEM prior to the experiment by means of a calibration device of defined length is essential. Statistical errors are fluctuations in observations which yield results that differ from measurement to measurement and that require repeated experimentation to obtain precise results.[26] Such errors of repeated independent measurements of the same length can generally be approximated well by the normal distribution. The statistical errors can be reduced significantly if the SEM is calibrated well, as demonstrated in case of the presented example, where the deflections are measured with a field emission SEM at a magnification of 20000x with a standard deviation of only $10nm$.

These errors in the measurements of the lengths of section A and B, l_A and l_B, the deflection δ, as well as the thicknesses of the cantilever substrate and the sublayers, $t_{sub,c}$ and t_{sl}, affect the determined stresses in a complex way. In order to get an idea of the most important parameters and to ensure a proper design of the experiment, the influence of the errors on four model stress distributions is discussed in section B.4.

B.3.4 Reliability of the Values for the Young's Moduli

The Young's moduli of the system have a great influence on the magnitude of the stresses determined because they affect the position of the neutral plane and associate the measured strains with the corresponding stresses according to the Hooke's Law. The Young's moduli used in the calculation procedure can be determined by means of one of the methods available.[17–22] Alternatively, elastic moduli of the substrate and the thin film can be obtained from literature as it is the case in the presented example.

Depending on the materials and the testing procedure the values for the Young's moduli are more or less reliable. Especially for complex coating systems, it can be difficult to find useful values because the elastic properties depend strongly on the fabrication parameters which are often not well defined. Furthermore, the properties of the surface layer can be changed by the ion beam during the actual experiment. For most materials, usually only the first few nanometers are affected, which leads to the conclusion that the average Young's module of the thin film, and even the individual sublayers, is not shifted significantly. Often such errors have to be estimated because in many cases it is not possible to quantify them statistically. As with the errors of the SEM-measured dimensions, the influence of the errors of the Young's moduli will be investigated subsequently by means of four model stress distributions.

B.3.5 Fracture and Plastic Deformation

Fracture and plastic deformation of the substrate or the thin film has to be avoided during the experiment to ensure a linear elastic behaviour of the system. A simple way to prevent these effects is the choice of an adequate cantilever substrate thickness, which leads to convenient deflections and stresses, which are significantly smaller than the fracture stress or the yield stress. Useful cantilever dimensions can be estimated by assuming a stress distribution probable for the investigated system and calculating the minimum and maximum stresses that occur during the experiment for various cantilever substrate thicknesses. A cantilever substrate thickness that gives reasonable deflections and presumably does not lead to fracture or plastic deformation is chosen as a suitable dimension for the actual experiment.

A reliable way to assure after the experiment performed that the calculated stress distribution is not influenced by plastic deformation or fracture is to compare the determined mean stresses of the ILR method to another method, for example the wafer curvature method. Possible fracture or plastification during the experiment would lead to a remarkable difference between the two mean stresses and would therefore indicate the invalidity of the experiment.

B.4 Experimental Design to Minimize Errors in the Stress Distribution

The set-up as well as the actual experimental procedure can be optimized to minimize the errors mentioned above. Optimal cantilever dimensions to reduce the errors in the deflection measurement and to avoid fracture and plastic deformation are discussed along with comparing four model stress profiles with respect to the influence of the input errors like the SEM-measured dimensions and the Young's modulus of the film on the calculated result. The basic considerations and equations for the error analysis which is based on the Gaussian or normal error distribution are presented.

B.4.1 Useful Choice of Cantilever Dimensions

Since the mean stress and the stress distribution is unknown during the planning of the experiments, an expected mean stress or an expected stress distribution should be used to estimate the deflection and the changes in the stress distribution during the cutting and removal procedure.

For the example presented, a mean film stress in the initial system of $-1.21GPa$ was determined by means of the wafer curvature method. The initial deflections are calculated for cantilevers with different substrate thicknesses, section lengths of $l_A = 16\mu m$ and $l_B = 92\mu m$, and the elastic moduli of the system presented. The film thickness in section A is reduced gradually and the actual deflections as a function of film thicknesses for selected substrate thicknesses as depicted in Fig.B.5. In case of thick cantilevers, the deflection changes nearly linearly with the removed film thickness and the deflection as well as the change of the deflection is very small, which would complicate their exact measurement with the SEM. With decreasing substrate thickness, the initial deflections as well as the changes of the deflections increase and the shape of the curves become more

nonlinear, which makes the SEM readout of the deflections more accurate. However, large curvatures can result in plastic deformation or fracture of the involved structure or the substrate. Therefore, the dimensions of the cantilever have to be adjusted to the expected stresses, the thickness of the structure and the materials involved to avoid fracture or plastic deformation during the experiment and to achieve a convenient ratio between the error of the deflection measurement and the measured deflections $\Delta\delta/\delta$.

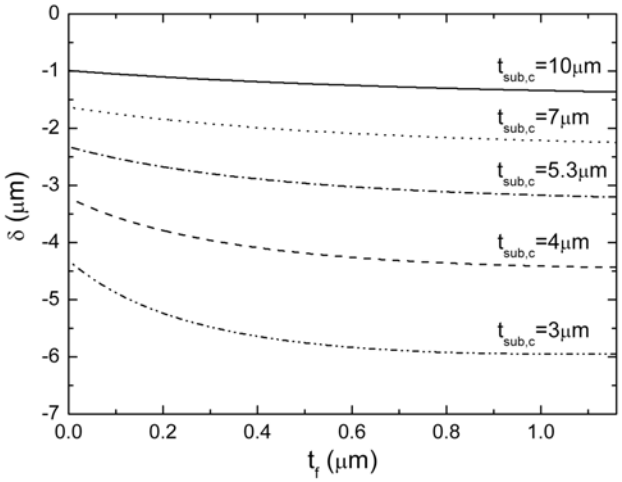

Figure B.5: Deflection of the cantilever as a function of film thickness calculated for various cantilever substrate thicknesses. The deflection is calculated for the $1.16\mu m$ TiN film ($E_{b,TiN} = 400GPa$) on $450\mu m$ Si substrate ($E_{b,Si(100)} = 180GPa$) and a mean film stress in the initial system of $\overline{\sigma}_f = -1.21GPa$. The deflections calculated for a substrate thickness of $5.3\mu m$ are similar to the measured deflections depicted in Fig.B.2

A useful initial deflection for a cantilever of $100\mu m$ in length, for example, would be $-3.5\mu m$ which corresponds to a curvature of $-700m^{-1}$. After the stepwise removal of the entire thin film in section A ($l_A = 15\mu m$) a deflection of $-2.5\mu m$, which comes solely from the curved indicator, remains. Such initial and final deflections are a good choice for film thicknesses between a few hundred nanometers and a few micrometers because much larger deflections can lead to fracture or plasticity and smaller deflections contain large relative errors when measured with the SEM.

Cantilever substrate thicknesses that lead to such useful deflections can be obtained from Fig.B.6 for various combinations of elastic moduli and film stresses. In order to include as many cases as possible, the film stresses are expressed by means of the constant curvatures of the initial systems. The curvature of this initial system has to be estimated or calculated from the film stress by means of Stoney's equation (B.1).[27]

$$\kappa = \frac{6\sigma_f t_f}{E_{b,sub} t_{sub,is}^2} \tag{B.1}$$

The estimations in Fig.B.6 refer to initial systems of $500\mu m$ substrate thickness. If the substrate of the initial system of interest is significantly thicker or thinner than $500\mu m$ (anyway, $t_{sub,is} >> t_f$ has to be valid), the curves plotted in Fig.B.6 cannot be used for the estimation. In this case, Eq. (B.2), which is derived from Stoney's equation, is used

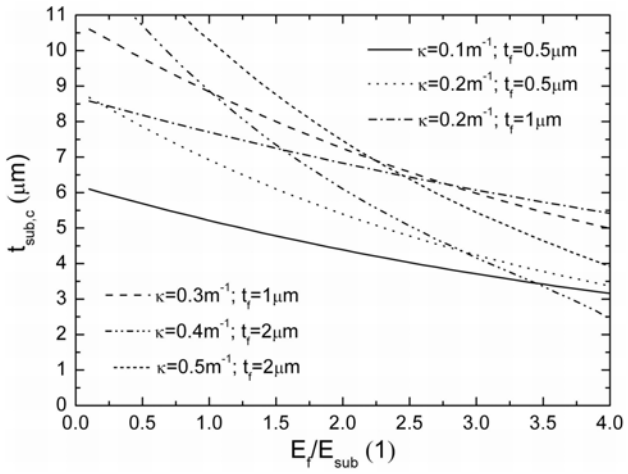

Figure B.6: Cantilever substrate thicknesses $t_{sub,c}$ that lead to initial deflections of $-3.5\mu m$ and final deflections of $-2.5\mu m$ as a function of the ratio E_f/E_{sub} for various combinations of curvature and film thickness of the initial system ($t_{sub,is} = 500\mu m$).

to calculate the curvature of an initial system with the same film stress as the actual initial system but a substrate thickness of $500\mu m$.

$$\kappa_{500\mu m} = \frac{\kappa_x \left(t_{sub,x}\right)^2}{\left(500\mu m\right)^2} \tag{B.2}$$

To estimate the tendency towards fracture and plastic deformation, the stresses in the curved cantilever as a function of film thickness should be analyzed. Nevertheless, it has to be kept in mind that this estimation is based on the assumed mean stress or stress distribution in the thin film of the initial system and that it can differ significantly from the real stress distribution, which would lead to different variation of the stresses during the experiment.

Another relevant point is the choice of the lengths of section A, from which the film is removed stepwise, and section B, the indicator that amplifies the curvature.

Generally, section B should be as long as possible to amplify the deflection changes of section A efficiently. This length does not influence the occurrence of plastic deformation or fracture, since the stresses in the cantilever only depend on the substrate thickness. However, large dimensions lead to long milling times, therefore lengths of section B between $50\mu m$ and $100\mu m$ have proven to be a good compromise between amplification of the curvature of section A and FIB milling time.

In principle, section A should be as large as possible to produce a pronounced change of curvature when a sublayer is removed, but it is not possible to remove curved sublayers with the FIB, especially when we take into account that the curvature changes during the removal of the film. Therefore, straight sublayers are removed and the length of section A has to be limited in order to neglect the curvature, which assures nearly constant film thickness in section A at each step and facilitates the calculation procedure. For a typical curvature of the cantilever of about $700m^{-1}$, a length of section A of approximately $15\mu m$ leads to useful curvature changes and well defined sublayer geometries.

The cantilever width does not influence the calculation of the stress distribution as

long as it is larger than the film thickness. Therefore, it does not contribute directly to the calculation of errors. The cantilever should not be wider than a few microns because imperfect parallel alignment of the ion beam and the film surface leads to wedge-shaped sublayers and the thickness of the sublayers cannot be measured correctly. The error in thickness measurement increases with increasing cantilever width. This relatively weak effect is not included explicitly in the following calculation of errors and can be considered in the input error for the thickness measurement.

B.4.2 Description of the Four Model Stress Distributions Used for the Error Analysis

Four model stress distributions in layered structures on thick substrates are compared to investigate the influence of the experimental parameters and the input errors on the stress profile determined by means of the ILR method. These depth profiles of residual stresses depicted in Fig.B.7 are chosen to show that the effect of the input errors on the calculated result depends significantly on the type of stress distributions investigated.

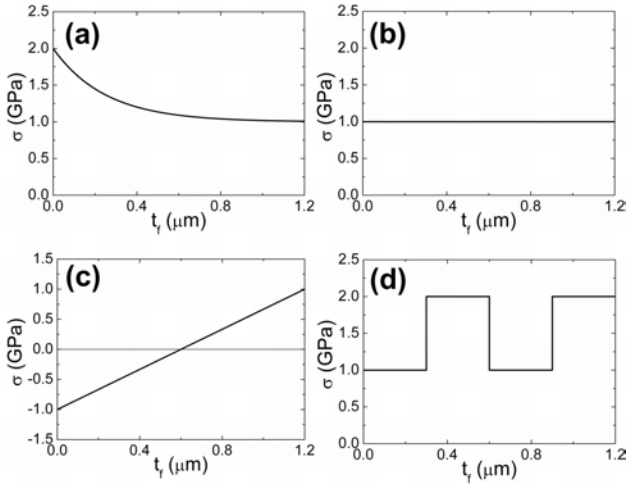

Figure B.7: Four model stress distributions in thin films on thick substrates represent basic types of stress profiles: (a) e function, (b) homogeneous, (c) gradient and (d) stress variation.

For simplification, all four layered structures are $1.2\mu m$ thick, the biaxial Young's moduli of the four films are $E_{b,f} = 400GPa$, and the biaxial moduli of the $500\mu m$ thick substrates are $E_{b,sub} = 200GPa$. Stress profile (a) called "e-function" represents a distribution where the tensile stresses grow exponentially from $1GPa$ at the surface to $2GPa$ at the interface. (b) is a simple homogeneous stress profile with $1GPa$ tensile stress. (c) describes a stress distribution with a constant gradient ranging from $-1GPa$ at the interface to $1GPa$ at the surface. (d) represents a square wave signal-type stress profile where the stress alternates between $1GPa$ and $2GPa$ with a "wavelength" of $600nm$. The average stresses in the initial systems lie between $0GPa$ in case of the stress profile with the constant gradient as depicted in Fig.B.7 (c) and $1.5GPa$ in case of the square wave signal-type stress distribution in Fig.B.7 (d).

B.4.3 Description of Error Analysis

The measured dimensions and deflections as well as the values for the Young's moduli are described by Gaussian or normal distributions. This is physically useful because the normal distribution describes the distribution of random observations for most experiments.[26] It furthermore serves as approximation for the literature values of the Young's moduli. Thus, the magnitude of the input errors is described by the corresponding standard deviations, provides useful data and allow the use of simple calculations to determine the propagation of errors. For example, if a deflection δ contains the error $\Delta\delta$, 68% of the repeatedly measured values of this deflection δ are within $\delta \pm \Delta\delta$.

The propagation of the input errors and the resulting error of the stress profile is described by Eq. (B.3), which describes the dependence of the error of the stress distribution $\Delta\sigma$ on the stress σ itself, the input variable x_i and the corresponding standard deviation Δx_i of the input variable. Eq. (B.3) considers the phenomenon that errors cancel each other out partially.[26]

$$\Delta\sigma = \sqrt{\sum_{i=1}^{n} \left(\frac{\partial\sigma}{\partial x_i} \Delta x_i \right)^2} \tag{B.3}$$

B.4.4 Influence of Sublayer Thickness, Deflection and Young's Modulus

In this section, the influence of the sublayer thickness and deflection measurement as well the Young's modulus of the film on the errors of the stresses determined is analyzed and discussed. Concerning the sublayer thickness measurement, we have to distinguish between two types of errors:

1. the quality of the reproduction of the real stress distribution

2. the effect of the sublayer thickness on the error of the stress distribution determined.

First, a high number of thin sublayers are required to approximate complicated stress distributions by the corresponding step function as detailed as possible. Thin sublayers are especially important when a jagged stress profile is expected. The correlation parameter C that quantifies the degree of approximation of the real stress distribution $f(t)$ and the approximated step function $g(t)$ is calculated from Eq. (B.4). A small correlation parameter corresponds to a good approximation and vice versa.

$$C = \frac{\sqrt{\int \left(f(t) - g(t) \right)^2 dt}}{\sqrt{\int f(t)^2 \, dt}} \tag{B.4}$$

The four model stress distributions, each approximated by two step functions with two and nine sublayers, respectively, are depicted in Fig.B.8. The dependence of the correlation parameter C on the number of sublayers i is demonstrated for each of these four model stress distributions in Fig.B.9. As expected, the approximation of (a) and (c) improves with a growing number of sublayers, whereas the homogeneous stress profile (b) is approximated well for any number of sublayers. In case of the stress variation profile

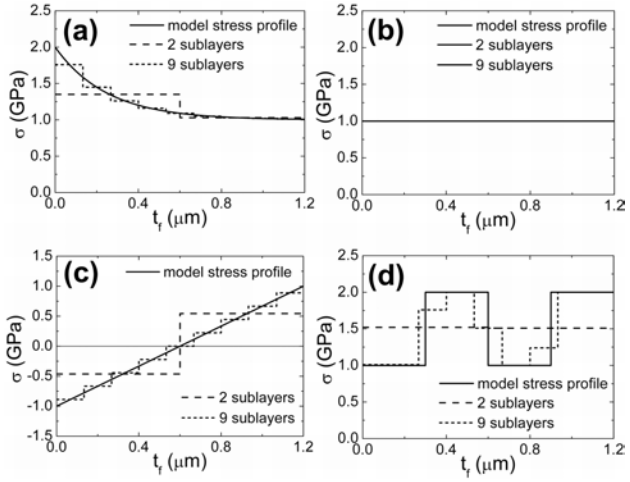

Figure B.8: Description of the four model stress distributions by means of the ILR method. Here, each thin film is divided into 2 and 9 sublayers, which leads to a more or less good approximation of the real depth profile of residual stresses.

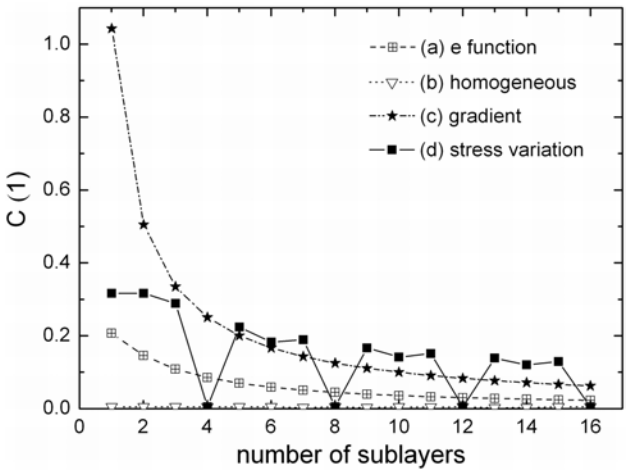

Figure B.9: Correlation parameter C as a function of the number of sublayers the films are divided in.

(d), the correlation is best when the number of sublayers is a multiple of the number of stress variations.

Secondly, an increase in the number of sublayers leads to a decrease in the mean sublayer thickness and therefore to larger relative errors in the thickness measurement. Therefore, an increase of the error of the calculated stresses is expected when the error of the thickness measurement increases.

A detailed error analysis of the homogeneous model stress distribution (the thin film in Fig.B.7 (b) is divided into 12 sublayers) is performed to investigate the influence of the error of the sublayer thickness measurement on the error of the resulting stress profile. The effect of the deflection measurement and the film's Young's modulus are examined. To ensure useful information, sublayer 1 (at the interface) and sublayer 12 (at the surface) are analyzed. Fig.B.10. shows that the influence of the three parameters ($\Delta\delta, \Delta t_f, \Delta E_f$) on the error of the stress distribution depends on the position of the investigated sublayer. While the accuracy of the measurement of the sublayer thickness is essential for small errors in sublayer 1, exact measurement of the deflection and a good choice of the film's Young's modulus ensure small errors in sublayer 12. This behaviour can be explained by analyzing the deflection as a function of film thickness for the homogeneous stress distribution and the influence of the three errors on this curve depicted in Fig.B.11. The influence of the three errors on the sublayer stress deviation depends on the position of the sublayer and the corresponding local gradient of the deflection function.

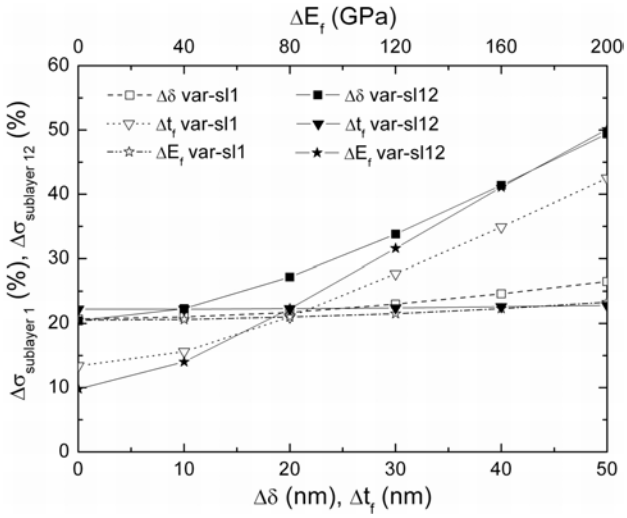

Figure B.10: The standard deviation $\Delta\sigma$ of the calculated stress in the undermost sublayer 1 (open symbols) and uppermost sublayer 12 (full symbols) of the stress profile depicted in Fig.B.7 (b). While one of the three parameters increases, the other two are kept constant at the values listed in table B.1.

The error in sublayer 1, which is located next to the substrate, depends mostly on the accuracy of the sublayer thickness measurement because a small variation of the sublayer thickness leads to large changes in the deflection due to the large gradient in the function. The deflection measurement leads to a moderate increase of the standard deviation of the stress calculated, which can also be explained by means of the strong gradient of the curve. The error in the Young's modulus of the film does not have a great influence

Table B.1: Input values and input errors used for the error analysis.

t_{sub} (μm)	t_f (μm)	$t_{sublayer}$ (nm)	$E_{sub,b}$ GPa	$E_{f,b}$ GPa	l_A μm	l_B μm
3	1.2	100	200	400	15	85

Δt_{sub} (nm)	Δt_f (nm)	$\Delta\delta$ (nm)	$\Delta E_{sub,b}$ (GPa)	$\Delta E_{f,b}$ (GPa)	Δl_A (nm)	Δl_B (nm)
150	20	10	20	80	200	300

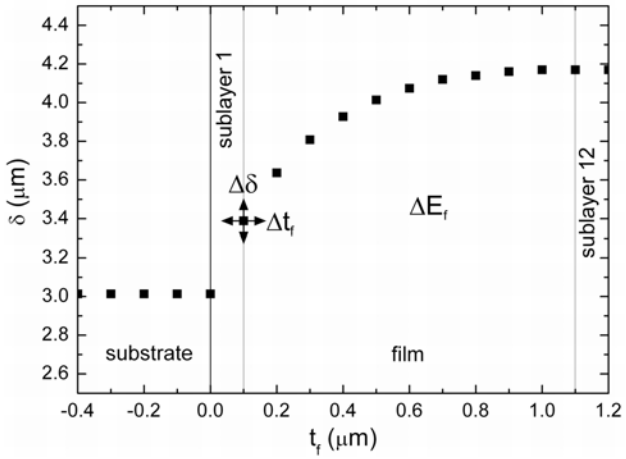

Figure B.11: Illustration of the errors $\Delta\delta, \Delta t_f, \Delta E_f$ in the measured deflection versus film thickness-function.

because the substrate thickness is large compared to the current film thickness.

The error in the uppermost sublayer, sublayer 12, shows a different behaviour: The accuracy of the sublayer thickness measurement does not lead to large errors because the weak gradient of the deflection function leads to hardly any change in the corresponding deflection. On the other hand, the deflection measurement itself is very important for small errors. A small error in the film's Young's modulus is essential because the error in the modulus influences the position of the neutral plane as well as the actual calculation procedure significantly. This effect is especially pronounced when only few sublayers of the film were removed and the film thickness is not thin compared to the cantilever substrate thickness.

B.5 Determination of Young's Moduli of Thin Films

As already mentioned, the ILR method needs the knowledge of the Young's moduli for the determination of the residual stress distribution. However, with some additional information, the ILR method can be used to calculate the Young's modulus of thin films when the mean stress in the film is known, for example, by means of the wafer curvature method. Therefore, first the mean stress in the thin film is determined from

the curvature of the sample by means of Stoney's equation,[27] which is independent of the Young's modulus of the thin film. Then, the stress profile in the thin film is calculated by means of the ILR method, which requires the thin film's modulus. The average stresses determined by means of the two methods are compared and the film's modulus of the ILR method is varied. The actual Young's modulus of the thin film is found when both mean stresses are equal.

Another possibility is the fabrication of cantilevers of significantly different substrate thicknesses. Then, the elastic modulus of the film can be determined by finding the Young's modulus that fits best the resulting variations in the displacements.

B.6 Final Remarks and Guidelines

Depending on the stress distribution, an appropriate choice of the number of sublayers can reduce the error of the correlation parameter C and therefore the total error of the ILR method dramatically. Especially for complex stress distributions, a large number of thin sublayers is a good choice because the details of rugged stress profiles can be reproduced well. In case of homogeneous stress distributions, a small number of thick sublayers can lead to more accurate results. However, a homogeneous stress distribution usually cannot be assumed prior to the experiment, therefore the division of the thin film into many thin sublayers is the most important measure for obtaining accurate results.

The cantilever dimensions -especially the substrate thicknesses- have to be adjusted to the estimated mean stresses to obtain useful deflections and to avoid plastic deformation or fracture during the experiment. Since the optimal substrate thickness depends on the film thickness, the materials involved and the stress distribution, general simple advice about the optimal thickness cannot be given. Therefore, the best way is to estimate the resulting changes of the deflection for an estimated stress distribution. The cantilever length is a compromise between short FIB milling times, pronounced deflections and homogenous film thicknesses in section A during the reduction of the film thickness. Lengths of section B around $90\mu m$ and of section A of about $15\mu m$ have proved to be a good choice.

The accuracy of the sublayer thickness and deflection measurement as well as the Young's modulus/moduli of the layered structure influence the errors in the stress profile calculated significantly. The analysis of the errors in individual sublayers of a homogeneous model stress distribution shows that the influence of these three parameters depends strongly on the position of the sublayers and the corresponding local gradient of the deflection as a function of film thickness.

B.7 Acknowledgements

The authors thank the Austrian Science Foundation FWF for supporting this work and I.C. Noyan, C. Brand, K.J. Martinschitz and M. Cordill for helpful discussions.

Bibliography to paper B

[1] Massl S, Keckes J, Pippan R, Acta Mater 2007;55:4835.

[2] Eiper E, Martinschitz KJ, Keckes J. Powder Diffr 2006;21:25.

[3] Resnik D, Aljancic U, Vrtacnik D, Mozek M, Amon S. Vacuum 2005;80:236.

[4] Dieing T, Usher BF. Phys Rev B 2003;67:054108.

[5] Noyan IC, Cohen JB. Residual Stress. New York: Springer;1987.

[6] Genzel C. Mater Sci Technol 2005;21:10

[7] Freund LB, Suresh S, Thin film materials, Cambridge: Cambridge University Press; 2003, p. 244.

[8] Mendibide C, Steyer P, Esnouf C, Goudenau P, Thiaudiere D, Gailhanou M, Fontane J. Surf Coat Technol 2005;200:165.

[9] Kitamura T, Hirakata H, Itsuji T. Eng Fract Mech 2003;70:2089.

[10] An J, Zhang QY. Surf Coat Technol 2005;200:2451.

[11] Barshilia HC, Deepthi B, Prabhu ASA, Rajam KS. Surf Coat Technol 2006;201:329.

[12] Bedell SW, Reznicek A, Fogel K, Ott J, Sadana DK. Mater Sci Semicon Proc 2006;9:423.

[13] Carlotti G, Doucet L, Dupeux M. Thin Solid Films 1997;296:102.

[14] Novotna Z, Kralova R, Novak R, Marek J. Surf Coat Technol 1999;116-119:424.

[15] Comins JD, Pang W, Every AG, Pietersen D. Refract Met Hard Mater 1998;16:389.

[16] Haider J, Rahman M, Corcoran B, Hashmi MSJ. Mater Proc Technol 2005;168:36.

[17] Bamber MJ, Cooke KE, Mann AB, Derby B. Thin Solid Films 2001;398-399:299.

[18] Kim SH. Mater Lett 2007;61:3589.

[19] Huang Z, Leighton G, Wright R, Duval F, Chung HC, Kirby P, Whatmore RW. Sens Actuators A 2007;135:660.

[20] Zhang J. J Mater Proc Technol 2002;123:329.

[21] Antunes JM, Fernandes JV, Sakharova NA, Oliveira MC, Menezes LF. Int J Solids Struct 2007;44:8313.

[22] Tran MD, Poublan J, Dautzenberg JH. Thin Solid Films 1997;308-309:310.

[23] Kim YR, Chen P, Aziz MJ, Branton D, Vlassak JJ. J Appl Phys 2006;100:104322.

[24] Kiener D, Motz C, Rester M, Jenko M, Dehm G. Mater Sci Eng A 2007;459:262.

[25] Ziegler JF, Biersack JP, Littmark U. The Stopping Range of Ions in Matter. New York: Pergamon Press;1985, p. 321.

[26] Devington PR. Data Reduction and Error Analysis for the Physical Sciences. New York: Mc Graw-Hill Book Company;1991.

[27] Nix WD. Metall Trans A 1989;20A:2217.

A New Cantilever Technique Reveals Spatial Distributions of Residual Stresses in Near-Surface Structures

S. Massl[a], J. Keckes[b] and R. Pippan[a]

[a] Erich Schmid Institute of Materials Science, Austrian Academy of Sciences, A–8700 Leoben, Austria
[b] Department Materials Physics, University of Leoben, A–8700 Leoben, Austria

Abstract

A focused ion beam technique that allows the characterization of spatial residual stresses in near-surface structures with a depth resolution on a nanoscale and a lateral resolution in the micron-range is introduced. It is based on the fabrication of a microcantilever and the gradual removal of the residually stressed material which leads to a change in the measured deflection. The method is presented by determining a spatial stress distribution around a scratch in a $840nm$ thin Ni film on Si.

C.1 Introduction

Residual stresses and their distributions are essential for the structural integrity and the performance of near-surface structures like optical thin films, hard coatings or metallic interconnects in microelectronic devices. In order to optimize the lifetime and stability of components, it is important to understand the distribution of the residual stresses at a micro- or nanoscale.

A number of methods has been developed to characterize stresses in thin films. Most techniques like the popular wafer curvature technique, for example, determine the average stresses in the layer from the curvature of the substrate, the elastic module of the substrate and the dimensions of the system by means of Stoney's Equation.[1] The mean stresses provide a useful guide value for some applications, but in many cases, the knowledge of the distribution of the residual stresses in the surface near area is an important information and helps to improve the lifetime of the component significantly. Such depth profiles and 3D stress distributions can be determined by means of conventional methods like X-ray diffraction methods[2–5] or Raman spectroscopy techniques.[6–9] Both techniques are non-destructive, provide depth resolution on a nanoscale and lateral resolution in the micron or submicron regime. However, X-ray methods can be used only for crystalline materials and Raman spectroscopy provides 3-D stress profiles only from Raman active materials. Furthermore, the evaluation procedures for both classes of techniques are not straightforward and usually involve several assumptions and/or simplifications.

Recently, the ion beam layer removal method (ILR method), which allows the determination of depth profiles of residual stresses on a nanoscale in crystalline, nanocrystalline or amorphous layered structures, was presented.[10] Although being destructive -even though on a small scale- this method combines the advantages of both techniques and requires only basic mechanical equations. Subsequently, the ILR method is presented briefly to introduce the basic ideas and procedures. Then, the 3D-ILR method for the determination of spatial stress profiles is illustrated.

C.2 Experimental

The basic ILR method is based on the fabrication of a microcantilever with a focused ion beam workstation (FIB) in the vicinity of the specimen edge. The cantilever consists of the stressed layer and the substrate material and curves owing to the intrinsic residual stresses, similar to a micro bimetal strip. This initial deflection is measured directly from a high magnification scanning electron microscope (SEM) image by tilting the specimen from the inclined ion beam cutting position into image recording position to obtain a front view of the cantilever as depicted in Fig.C.1(a). The corresponding curvature of the cantilever is correlated with the average stresses in the layer and the substrate by means of simple mechanical considerations. In order to obtain measurable deflections, useful cantilever dimensions can be estimated from the curvature, the dimensions and the elastic constants of the initial system.

Now, the cantilever is divided into section A, the fixed end, and section B, the free end. The stressed layer is removed step by step in section A by means of the ion beam aligned parallel to the specimen surface (Fig.C.1(b) and (c)). Section A is large compared to the thickness of the layer, but small enough to be considered straight despite being actually

curved, which assures constant layer thickness during the removal procedure. The individual material slices removed are denominated sublayers. This gradual reduction of the layer thickness affects the stress state and therefore the curvature of section A. Section B still has the initial curvature and acts as a curved indicator that amplifies the curvature of section A. The deflections measured are correlated with the actual curvatures in section A and the stresses that acted in the material slices removed.

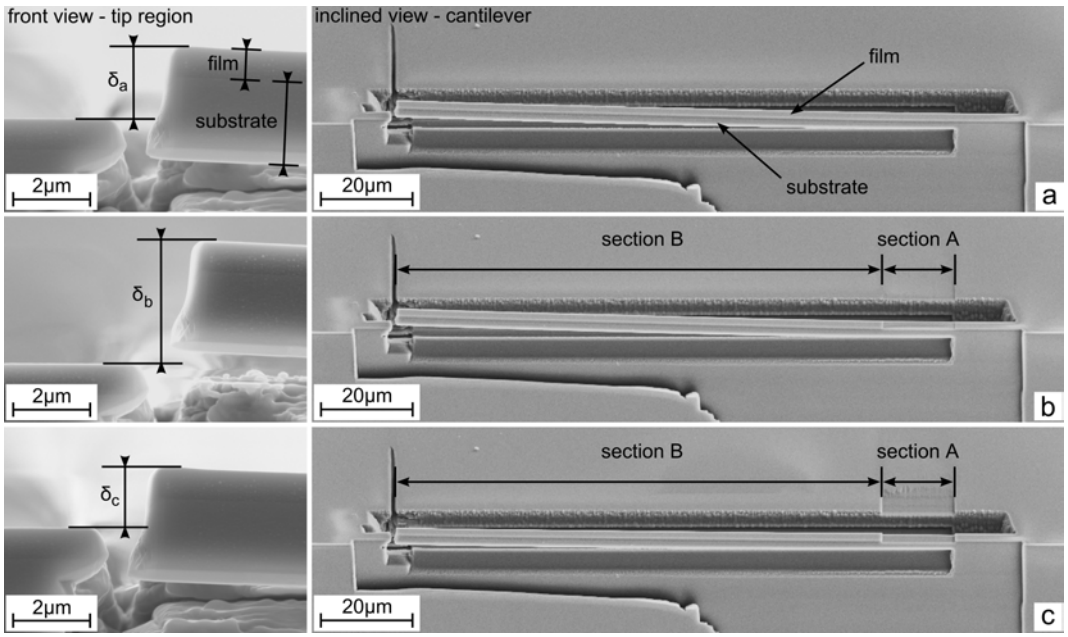

Figure C.1: Experimental procedure of the ILR method illustrated by means of an $800nm$ thin amorphous SiON on (100) Si system. Initially, the FIB-fabricated bimaterial cantilever deflects upwards owing to the tensile residual stresses in the layer (a). Then, the thin film is removed gradually in section A, which leads to a change in the stress state and the deflection. Here, only one of the steps is depicted (b). Finally, the whole film has been removed and the corresponding deflection is measured (c).

The stress profile in the cantilever is determined by superimposing the previously removed sublayers and establishing the force and moment balances to obtain the actual curvature for each step. A step function with step widths corresponding to the thickness of the individual sublayers describes the resulting stress distribution. As a good approximation, the calculated stress in a sublayer describes the average stress that acts in the volume defined by the thickness of this sublayer, the length of section A, and the width of the cantilever. Finally, the stress profile in the initial system is calculated from the stress distribution in the cantilever. The depth resolution depends on the sublayer thickness which can be reduced to values below $100nm$. The lateral resolution is determined by the length of section A and permits resolution in the micrometer regime.

The 3D-ILR method is a further development of the ILR method and allows the determination of three dimensional stress distributions by providing two dimensional stress profiles from a number of parallel cross sectional cuts through spatial stress profiles (Fig.C.2).

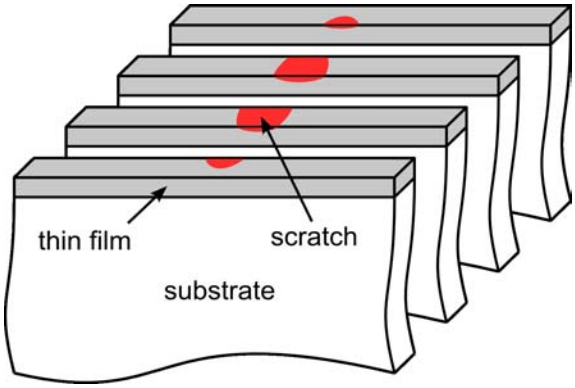

Figure C.2: Schematic view of two dimensional cuts of a thin film/substrate system scratched with a ball-shaped indenter.

In each experiment, the stress component along the cantilever fabricated parallel to the edge is determined. The stresses perpendicular to the cantilever relax partially, depending on the cantilever width. A determination of these stresses would require the fabrication of another cantilever perpendicular to the specimen edge. The experimental and calculation procedure for the two-dimensional stress profiles is similar to the procedure of the basic ILR method. Here, the 3D-ILR method is demonstrated by means of a spatial stress profile fabricated by scratching over a $840nm$ thin (111) Ni film deposited on a single crystalline (100) Si substrate with a ball-shaped indenter with a ball radius of $300\mu m$ and a defined normal force of $300mN$. There are various ways the two dimensional cuts through the spatial stress profile and the fabrication and calculation procedures can be performed; a simple one is presented here. First, a FIB cut is performed at the edge of the specimen to obtain a plane view on the cross section of the scratched system. This cross section is divided into a number of a few microns wide sections (B and A1 to A10) so that sections B and A1 should be located sufficiently far away from the centre of the scratch in order to minimize the influence of the plastic zone on the original depth profile of residual stresses. Sections A2 to A10 are situated alongside in such a way that section A10 is located near the estimated centre of the plastic zone (Fig.C.3).

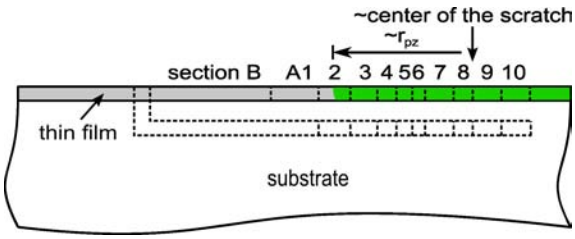

Figure C.3: Schematic view on the cross-sectional cut of the region around the scratch. The contour of the cantilever, the scratch and the expected size of the plastic zone are marked. In the presented example, the cross section is divided into section B and the sections A1 to A10.

Now, a cantilever consisting of section B -the indicator- and section A1 is fabricated from this cross section as described for the basic ILR method (Fig.C.4(a)). Then, the thin film is removed gradually in section A1 in order to determine the depth profile

of residual stresses in the thin film in this section until the whole thin film is removed (Fig.C.4(b)). In the presented example, the depth profile of residual stresses in section B, which is located far away from the scratch, is determined from a separate ILR experiment (Fig.C.5(B)).

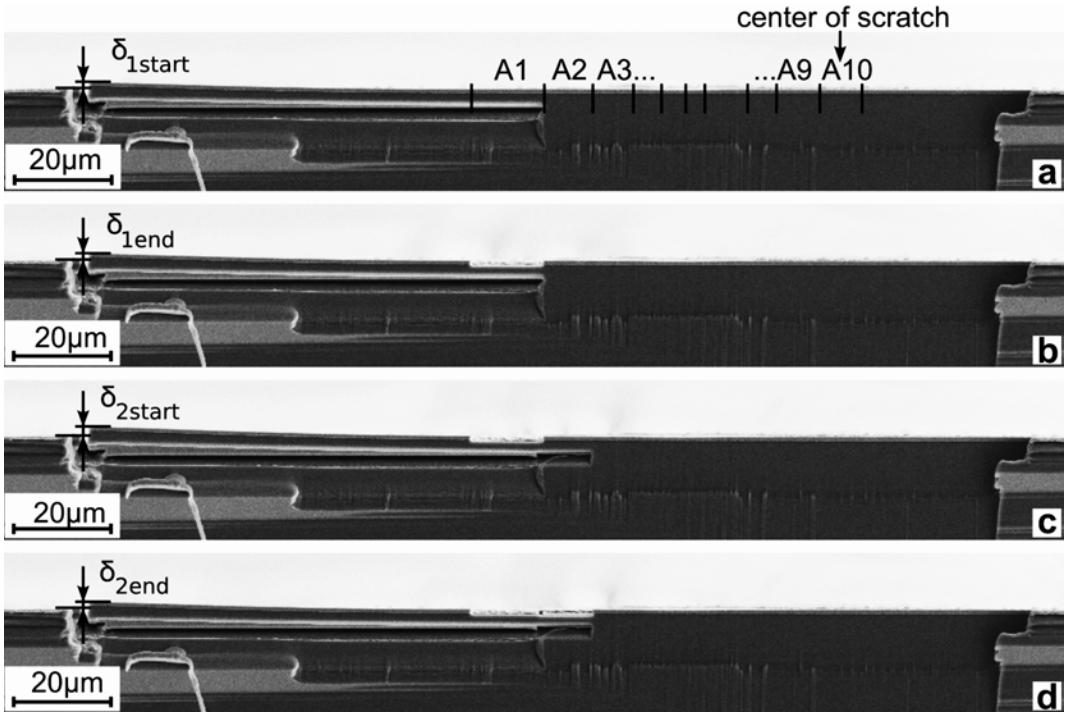

Figure C.4: SEM images of four steps of the experimental procedure of the 3D-ILR method. The initial curvature in section A1 is amplified by the free end of the cantilever (a). The thin film has been removed step by step and the corresponding deflections were measured. The uncoated and therefore straight section A1 leads to the deflection δ_{1end} (b). Lengthening the cantilever by removing the substrate in section A2 leads to the deflection δ_{2start} according to the contribution of the residual stresses in A2 (c). Removing the thin film step by step in section A2 leads to a gradual change in deflection and finally to δ_{2end} (d).

In the next step, the length of the cantilever is increased by the length of section A2 by removing substrate material. This extension leads to a change in the deflection according to the stress profile in section A2 as depicted in Fig.C.4(c). Then, the thin film is removed gradually in this section which leads to a change in curvature amplified by the indicator that now consists of the sections B and A1. The corresponding deflections as a function of film thickness in section A2 are measured for each step with the SEM and the depth profile of residual stresses is determined (Fig.C.4(d)).

This procedure of elongating the cantilever by the length of the actual section Ai, removing the thin film gradually and measuring the corresponding deflection is repeated until section A10 is reached and the cantilever is now $l_B + \sum l_{Ai}$ long. The calculated depth profiles of residual stresses as a function of the lateral position normal to the scratch are depicted in Fig.C.5.

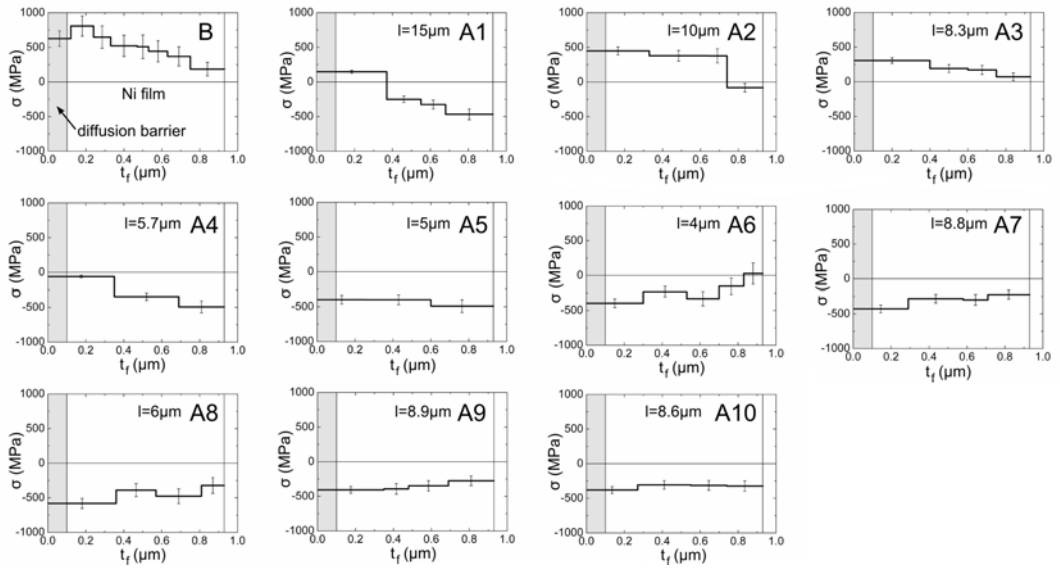

Figure C.5: Depth profiles of residual stresses in sections B and A1 to A10. The maximum of compressive stresses between A8 and A9 indicates the center of the scratch as it was suggested by SEM images. The stress distribution in section B, which is located far away from the scratch, was determined in a separate ILR experiment. The length of each section is written beside the denomination of the section.

C.3 Discussion and Concluding Remarks

The depth profiles of residual stresses in the vicinity of the scratched Ni film obtained with the 3D-ILR method show two main characteristics. First, the mean stress drops from initially $460 \pm 60 MPa$ in section B to a minimum value of $-478 \pm 91 MPa$ in section A8, which corresponds well to the SEM images that show the center of the scratch lying between sections A8 and A9. The radius of the plastic zone is therefore about 30 microns, considering the change from tensile to compressive stress between the sections A3 and A4. Secondly, the stress gradient vanishes towards the center of the scratch. The unexpected compressive stress determined in section A1, about 45 microns away from the center, could originate from the imperfect shape of the indenter, which would lead to a shallow imprint parallel to the scratch in this section. Owing to the indenter radius of 300 microns, micron size bumps on the indenter lead to peripheral contact, as it was also discovered in similar experiments. To assure that the compressive stress is limited to section A1, the thin film was removed in a few microns wide part of section B next to section A1. This resulted in a pronounced decrease in the deflection which leads to the conclusion that the thin film material removed on the left side of A1 was definitely subjected to tensile stresses.

The mean depth resolution of $200nm$ and the average lateral resolution of a few microns obtained in this experiment demonstrate the possibility for high spatial resolution. Further improvement can be achieved by removing thin sublayers with thicknesses below $100nm$[11] and designing the cantilever appropriately, which involves an adequate choice of the substrate thickness, the lengths of the sections Ai and the indicator section B. Another advantage of the 3D-ILR method is that information can be obtained directly

from the deflection versus film thickness-curve as depicted in Fig.C.6 for three examples. The characteristic of such a curve allows the estimation of the stress profile because the actual deflection correlates directly with the stresses in the sublayer removed. After having removed the thin film in a section, the deflection has a predictable value which comes solely from the curved indicator, because the substrate is stress free and straight. Since this deflection is equal for all sections, it gives further information about the accuracy of the experiment. The sign of the stress in the thin film removed can be estimated simply from the change of the deflection at the interface ($t_f = 0\mu m$). A drop indicates tensile stresses, whereas an increase of the deflection leads to the conclusion that the stress removed was compressive.

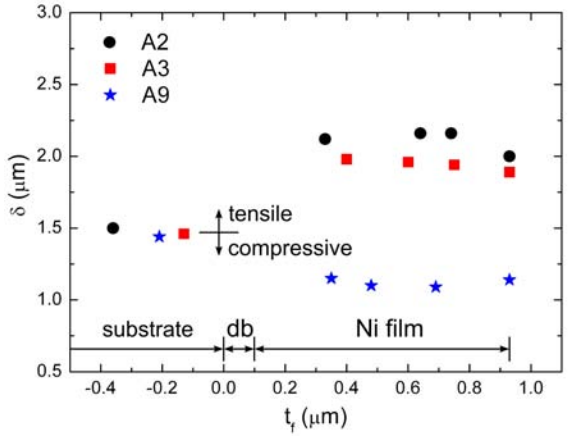

Figure C.6: Examples of measured deflections versus film thickness. The drops of the measured deflections after having removed the thin film and the diffusion barrier (db) completely in sections A2 and A3 indicate tensile film stresses. In section A9, the film was subjected to compressive stresses which leads to an increase of the deflection.

In summary, the presented 3D-ILR method is a powerful tool to determine two- and three-dimensional stress profiles in surface near layers. The direct approach and the simple calculation procedure make it a good choice for the evaluation of such stress distributions with a depth resolution on a nanoscale and a lateral resolution on a micron scale.

Bibliography to paper C

[1] Nix WD. Metall Trans A 1989;20A:2217.

[2] GenzelC. Mater Sci and Technol 2005;21:10.

[3] Marques MJ, Pina J, Dias AM, Lebrun JL, Feugeas J. Surf Coat Technol 2005;195:8.

[4] Ma CH, Huang JH, Chen H. Thin Solid Films 2002;418:73.

[5] Noyan IC, Cohen JB. Residual Stress. New York: Springer; 1987.

[6] Grabner L. J Appl Phys 1978;49:580.

[7] Dietrich B, Dombrowski KF. J Raman Spectr 1999;30:893.

[8] De Wolf I. J Raman Spectr 1999;30:877.

[9] Atkinson A, Jain SC. J Raman Spectr 1999;30:885.

[10] Massl S, Keckes J, Pippan R. Acta Mater 2007;55:4835.

[11] Massl S, Keckes J, Pippan R. Thin Solid Films, submitted.

D

Investigation of Fracture Properties of Magnetron-Sputtered TiN Films by Means of a New FIB-Based Cantilever Bending Technique

S. Massl[a], W. Thomma[a], J. Keckes[b] and R. Pippan[a]

[a] Erich Schmid Institute of Materials Science, Austrian Academy of Sciences, A–8700 Leoben, Austria

[b] Department Materials Physics, University of Leoben, A–8700 Leoben, Austria

Abstract

A cantilever bending technique for the determination of mode I fracture toughness and strength of thin films is presented. First, the depth profile of residual stresses in the film is determined in order to investigate the possible existence of pronounced stress gradients that could influence the crack initiation and propagation significantly. Then, cantilevers of about $70\mu m$ length consisting of the film and the substrate are fabricated by means of a focused ion beam workstation. The cantilever beams are loaded with an in-situ microindenter until fracture; the fracture toughness and the strength of the thin film are calculated straightforward from the load-deflection curve and the residual stresses determined. The fracture properties of a $1.1\mu m$ thick magnetron-sputtered TiN film on single crystalline Si are investigated. The fracture toughness and strength determined are $2.8\pm0.3MPa\sqrt{m}$ and $4.4\pm0.7GPa$, respectively. Finally, the influence of the compressive residual stresses on the structural integrity of such coated system and the role of the grain boundary strength are discussed.

D.1 Introduction

Strength and fracture toughness of thin ceramic films are important material parameters owing to their significant influence on the lifetime and the structural integrity of coated components. Such parameters are usually difficult to measure due to the small dimensions and the brittleness of the thin films.

Up to now, there is no commonly accepted standard testing procedure that allows a reliable, simple and reproducible determination of strength and fracture toughness of ceramic thin films. Techniques like micro- or nanoindentation[1–4] or the scratch test[5–7] are well-established, but the determination of fracture strength and fracture mechanical parameters is rather difficult owing to the complex stress fields induced in the material investigated during loading. Furthermore, the results obtained often quantify apparent fracture behaviour of a particular film-substrate system instead of the parameters of a specific material.[8] This problem was approached by recently developed methods like the four-point-bending method,[9] the microbridge method[10] or the micro-tensile fracture technique,[11] which feature defined sample and loading geometries and facilitate therefore the calculation of the actual fracture toughness and/or the strength of thin films.

The fracture behaviour of thin films on substrates is controlled by mechanical properties such as the strength of the film, the strength of the interface and the residual stress in the film. Independent evaluation of these parameters is important to understand the properties of coated systems and to ensure mechanical reliability.[8] In this paper, we want to focus on the fracture behaviour of the film material itself. As a model system, a $1.1\mu m$ thick TiN film deposited on single crystalline (100)Si by means of physical vapour deposition (PVD) is tested under mode I loading.

The strength and the fracture toughness of such films is strongly influenced by the structural morphology of the coating,[12] which usually exhibits a columnar structure.[1,3] The relative weakness of the grain boundaries compared to the TiN grains leads predominantly to intergranular fracture with the crack propagating perpendicular to the film/substrate-interface as discovered by nanoindentation[1–4] and scratch tests.[5] Some research groups suggested that the strength of the grain boundaries of PVD-deposited TiN films on steel substrates is so low that in fact the high compressive residual stresses might be the single most important factor for the mechanical stability of the film.[4,12,13]

The purpose of this paper is to present a new technique for the evaluation of strength and mode I fracture toughness of thin films based on the fabrication of micro-cantilevers by means of a focused ion beam workstation (FIB) and the subsequent testing of these cantilever beams in an in-situ microindenter mounted in a scanning electron microscope (SEM). The advantages as well as the limitations of the method presented and the measured strength and fracture toughness are investigated. Finally, the role of the grain boundary strength and the residual stresses for the mechanical integrity of the coated system are discussed for the presented example.

D.2 Experimental

The $1.1\mu m$ thick TiN film was deposited onto a $450\mu m$ thick silicon (100) substrates at $550°C$ by means of reactive sputtering from a Ti target in an $Ar + N_2$ atmosphere using a laboratory-scale unbalanced DC magnetron sputtering system. The total pressure and

the bias voltage was $0.25Pa$ and $-50V$, respectively. Finally, the thin film was subjected to a thermal cycle from $25°C$ to $700°C$ in vacuum at a maximum pressure of $10^{-3}Pa$ at a heating and cooling rate of $5Kmin^{-1}$.[14]

The depth profile of residual stresses in the TiN film is determined by means of the ion beam layer removal method (ILR method[15]), which is only described briefly here. The ILR method is based on the fabrication of a cantilever by means of a focused ion beam workstation (FIB) in the vicinity of the specimen edge. In the presented example, a Zeiss XB1540 Crossbeam FIB, which combines a Gallium-operated $30kV$ FIB and a high-resolution SEM equipped with a field emission gun, is used to fabricate the cantilever consisting of the $1.1\mu m$ thick film and the $5.3\mu m$ thick substrate. The cantilever bends owing to the residual stresses, similar to a bimetallic strip and the deflection of the free end is measured with the SEM at high magnification. Then, the thin film is removed gradually in section A, which leads to a change of the curvature in this section owing to the removal of the stressed material as depicted in Fig.D.1.

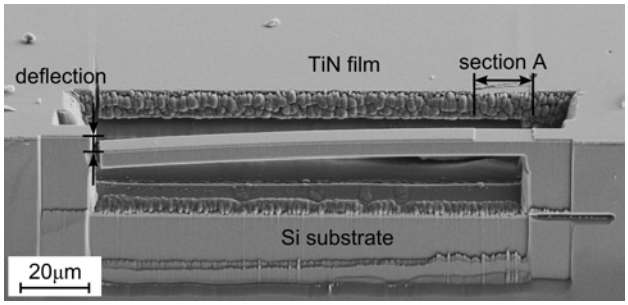

Figure D.1: SEM image of a micro cantilever fabricated with a FIB workstation for the determination of a depth profile of residual stresses in a thin film by means of the ILR method. Here, the thin film is removed gradually in section A, which affects the residual stresses and therefore the curvature. This change in curvature is amplified by section B that acts as a curved indicator. The deflections δ as a function of film thickness are the basis for the calculation procedure.

By considering the deflection versus film thickness curve, the dimensions of the cantilever and the elastic moduli of the materials involved, the depth profile of the residual stresses in the cantilever and finally in the initial system is determined. In the presented example, the Young's moduli and the Poisson's ratios necessary for the calculation of the biaxial Young's moduli are taken from literature ($E_{Si(100)} = 130GPa \pm 5\%$, $\nu_{Si} = 0.28 \pm 0.01\%$ and $E_{TiN} = 309Ga \pm 24\%$, $\nu_{TiN} = 0.27 \pm 14\%$).[16–31] The calculated depth profile of residual stresses in the TiN thin film of the initial system film is depicted in Fig.D.2. For comparison, the average film stress is determined by means of the well-known wafer curvature technique[32–34] showing good agreement of the results ($\overline{\sigma}_{WCM} = -1.2GPa$, $\overline{\sigma}_{ILR} = -1.5GPa$).

The eight cantilevers for the actual fracture experiments are fabricated along the Si $\langle 100 \rangle$ direction by means of the FIB from the same specimen where the stress distribution was determined. Four of the cantilevers are used for the determination of fracture stress in the TiN film; the remaining four are prepared to determine the fracture toughness of the film. The cantilever substrate thicknesses range from $2\mu m$ to $10\mu m$, which leads to different residual stress distributions in the microbeam and as a consequence to different

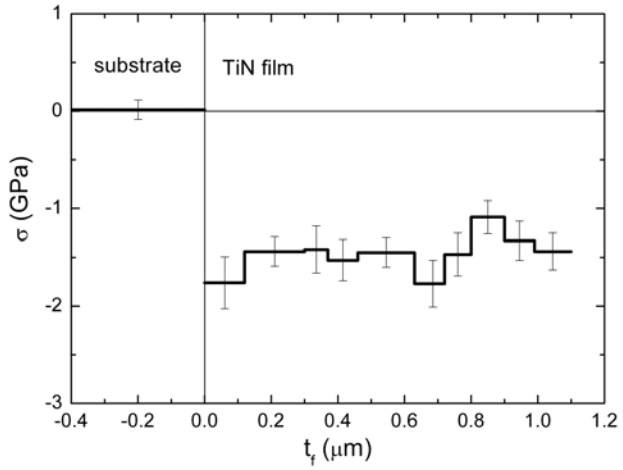

Figure D.2: Depth profile of residual stresses in the TiN film of the initial system determined by means of the ILR method. This film exhibits a homogeneously distributed compressive stress with an average value of $-1.5GPa$.

deflections as depicted in Fig.D.3 (a) and (b).

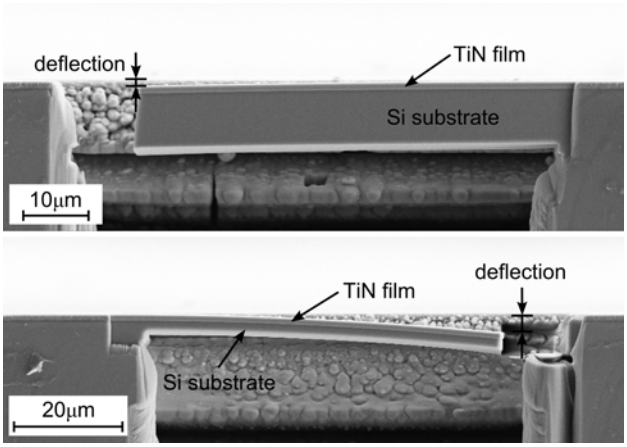

Figure D.3: SEM images of FIB-fabricated cantilevers used for the fracture experiments (front view). The cantilevers deflect owing to the intrinsic residual stresses, which depends among other things on the substrate thickness. Cantilever 1 depicted in (a) has a substrate thickness of $8.7\mu m$ and exhibits a deflection of $-0.74\mu m$, whereas the substrate of cantilever 8 (b) is only $2.2\mu m$ thick resulting in a deflection of $-3.2\mu m$.

For comparison, the deflection is calculated by means of simple mechanical considerations from the depth profile of residual stresses determined by means of the ILR method, the dimensions of the cantilevers as well as the biaxial Young's moduli of the materials involved. The experimentally determined and the calculated deflections are listed in Table D.1.

The advantage of fabricating a number of cantilevers of different thicknesses is that the substrate thickness is correlated with the film stresses allowing the investigation of the fracture properties for different stress distributions in the thin film. In other words,

Table D.1: The comparison of the cantilever deflections measured with the SEM and the deflections calculated from the film stress determined by means of the ILR method, the dimensions and the elastic moduli shows excellent correlation.

cantilever no.	t_{sub} μm	δ_{exp} μm	δ_{calc} μm
1	8.7	-0.74	-0.68
2	10	-0.74	-0.61
3	5.3	-1.4	-1.31
4	6.5	-1.0	-0.88
5	5	-2.0	-2.04
6	4.8	-1.9	-1.87
7	2	-3.4	-3.95
8	2.2	-3.2	-3.44

the cantilevers of different thicknesses fabricated from only one specimen are investigated instead of a number of cantilevers, each fabricated from a separate specimen with different depth profiles of residual stresses.

After fabricating the cantilevers and measuring the deflections, tungsten marks of about $2\mu m$ length, $500nm$ width and $500nm$ height are deposited on the thin film near the free ends in the mirror plane of the cantilevers as depicted in Fig.D.4 by means of the gas injection system attached to the FIB workstation. These marks facilitate the locating of the exact centre of the beam with the in-situ microindenter. Then, $200nm$ deep pre-cracks are introduced at the origin of the four cantilevers fabricated for the determination of the fracture toughness by means of the FIB with an ion current of $50pA$ to ensure a defined notch and to minimize the ion damage as shown in Fig.D.4 (b). The milling time was adjusted to the cantilever width to obtain pre-cracks of uniform depth.

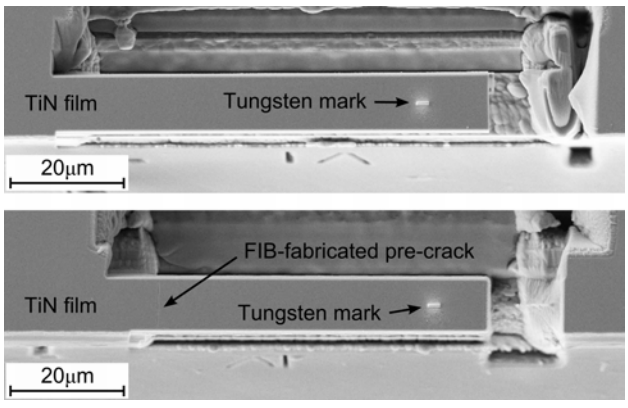

Figure D.4: SEM images of cantilevers for fracture experiments (top view). The cantilevers without pre-crack as depicted for cantilever 6 in (a), are used for the determination of the fracture strength, whereas the FIB-notched cantilever beams as shown in (b) for cantilever 4, allow the determination of the fracture toughness of the thin film. The bright spots near the free end of the cantilever are the FIB-deposited tungsten marks.

The dimensions of the cantilevers -substrate thickness, width, and length- are listed in

Table D.2.

Table D.2: Dimensions of the FIB-fabricated cantilevers used for the determination of the fracture strength and the fracture toughness. The notched cantilevers for the determination of the fracture toughness are marked with a *.

cantilever no.	t_{sub} μm	w μm	l μm
1	8.7	9.6	64.5
2*	10	10	68
3	5.3	10	64
4*	6.5	10	60
5*	5	10.8	77
6	4.8	10.5	72
7	2	9.8	67
8*	2.2	10.6	65

The actual fracture mechanical tests are performed by means of an ASMEC UNAT in-situ microindenter equiped with a cube corner tip mounted in a Zeiss 440 SEM. First, the cantilever to be tested is positioned in the vicinity of the indenter. The sample is mounted in the SEM in such a way that a front view on the cantilever is obtained, which allows only coarse positioning in z-direction. To position the indenter tip exactly in the mirror plane of the cantilever, the tip is lowered slowly onto the FIB-deposited tungsten mark. Only at the desired z-position, the tip touches the top of the mark and the measured force increases slightly; otherwise, the tip disappears behind the tungsten mark or vice versa and the z-position has to be adjusted. Now the stage is moved to position the indenter tip a few microns away from the free end of the cantilever for the actual experiment. On the one hand, a large distance between the origin of the cantilever and the tip is necessary to assure predominantly bending load at the origin and to minimize the shear stresses. On the other hand, the tip must be located at a safe distance from the free end of the cantilever to avoid shearing off the thin film. This is especially important in case of the thin cantilevers, where large deflections are obtained during the experiments. The distances between the loading point and the cantilever origin range beween $38\mu m$ for cantilevers 7 and 8 and $53\mu m$ for cantilever 5, which leads to convenient ratios between the maximum normal and the shear stresses. The cantilever is loaded displacement controlled with $2.5nm/s$ as depicted in Fig.D.5 and the load-deflection-curve is recorded. SEM images are recorded every 60 seconds to survey the experiment.

Additionally to the actual fracture experiments, the specimen is indented far away from the FIB-fabricated cantilevers with the same loading parameters. This allows the separation of the load-deflection-curve recorded during the cantilever fracture experiments into a contribution coming from the actual bending of the cantilever and contribution resulting from the indentation into the thin film. In other words, the corrected curve describes force necessary to deflect an impenetrable cantilever. The determination of the corrected load-deflection-curves is essential because especially in case of cantilevers with thick substrates, the deflection values of the as-recorded curves overestimate the actual deflection of the cantilever due to the formation of the imprint somewhat.

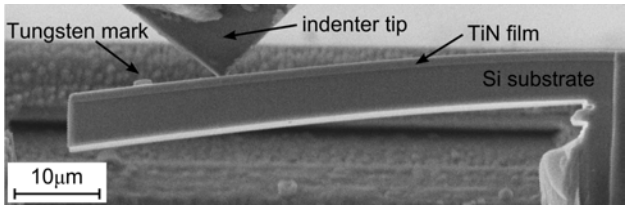

Figure D.5: SEM picture of the loading of cantilever 3 by means of the in-situ microindenter (front view). The bright hump $10\mu m$ left of the indenter tip is the FIB-deposited tungsten mark necessary for the exact positioning of the indenter in the mirror plane of the cantilever.

D.3 Results

The as-recorded as well as the corrected load-deflection-curves show perfect linear behaviour until fracture for all cantilevers tested as depicted in Fig.D.6 for cantilever 1 (without pre-crack), for example. Owing to the substrate thickness of $8.7\mu m$, this cantilever is relatively stiff, which leads to a significant penetration of the indenter tip and therefore to a remarkable difference between the two curves. The corrected load-deflection-curves of all eight cantilevers tested are depicted in Fig.D.7.

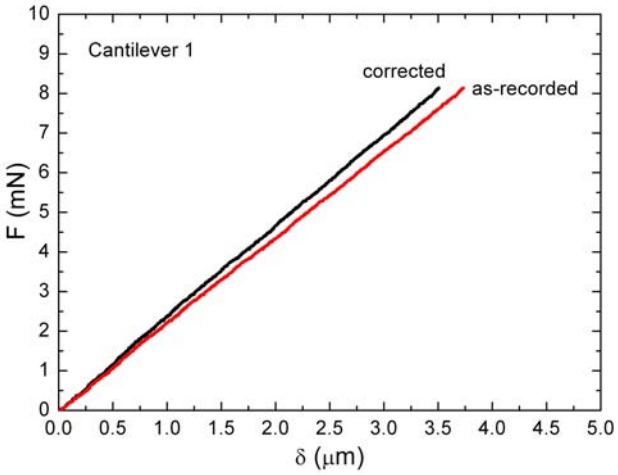

Figure D.6: As-recorded and corrected load-deflection-curve for cantilever 1. The corrected curve describes solely the force necessary to deflect the cantilever, whereas the as-recorded curve considers additionally the contribution of the penetration of the indenter tip into the thin film. This contribution can be neglected in case of cantilevers with thin substrates, where only small forces are necessary to produce a certain amount of bending, which leads to shallow indents.

The deflection resulting from loading, the load at fracture and the corresponding deflection as well as the loading distance between the indenter tip and the cantilever origin are listed in Table D.3.

The investigation of the fractured cantilevers shows that the notched cantilevers fractured exactly at the FIB-fabricated pre-crack, whereas the cantilevers without pre-crack fail in vicinity of the cantilever origin as depictured in Fig.D.8.

The fracture stress of the TiN film is determined from the cantilevers without notch by

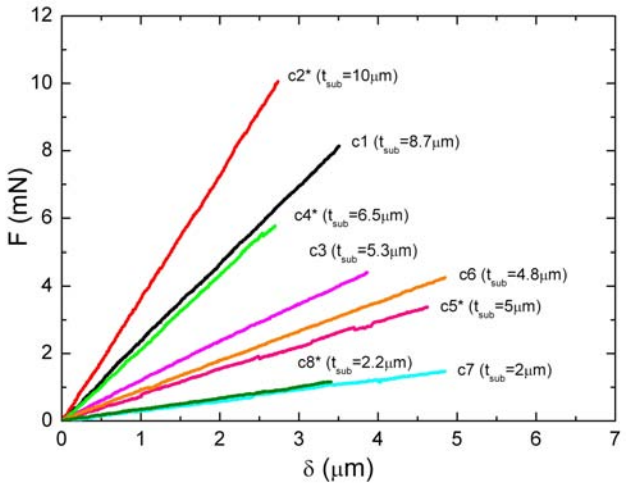

Figure D.7: Corrected load-deflection-curves of the cantilevers examined. Although general trends can be seen, it must be taken into account that the curves cannot be compared directly because of the differences in widths and loading distances. Nevertheless, all cantilevers tested show perfectly linear load-deflection-curves until fracture. The notched cantilevers are marked with a *.

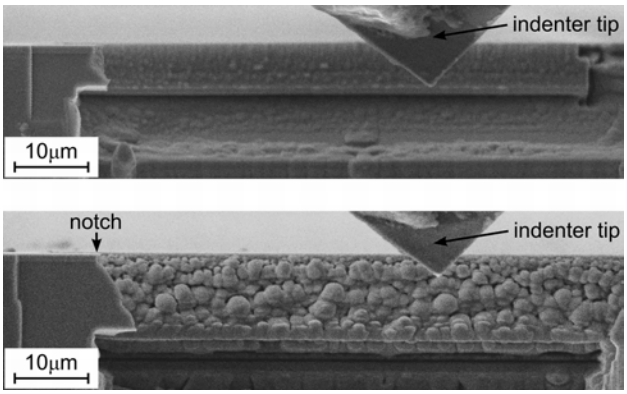

Figure D.8: SEM images of fractured cantilevers (front view). The notched cantilevers fracture exactly at the pre-crack as shown for cantilever 2 in (a), whereas the crack in the cantilevers without notch initiated and propagated in the vicinity, but not exactly at the origin of the beam as depicted in (b) for cantilever 6.

Table D.3: Deflection, load at fracture and loading distances for the cantilevers tested. The notched cantilevers for the determination of the fracture toughness are marked with a *.

cantilever no.	d_{frac} μm	F_{frac} μm	l_{load} μm
1	3.51	8.13	50.5
2*	2.73	10.05	48.3
3	3.86	4.41	42.7
4*	2.69	5.77	40.6
5*	4.62	3.38	53.8
6	4.85	4.26	48.6
7	4.85	1.47	38.8
8*	3.4	1.16	37.9

superimposing the residual stress profile of the cantilever that curves owing to the intrinsic stresses and the stresses at the origin of the cantilever induced by the loading. The crack is assumed to form at the surface where the tensile stresses are highest. Therefore, the fracture stress is simply the surface stress in length direction at its origin just before fracture.

The fracture toughness of the TiN film is determined from the experiments carried out with the notched cantilevers. As described above, first the intrinsic stresses and the stresses at the cantilever's origin owing to loading are superimposed. Then, the stresses in length direction $200nm$ below the surface, which is the exact location of the crack tip, are calculated. Since the stress profile at the origin of the cantilever is mainly a result of the external loading, the stresses in the vicinity of the crack tip are approximated well by a stress profile resulting from a bending moment applied at the tip of the cantilever. This moment is calculated in such a way that it produces the same stress $200nm$ below the surface as the combination of the residual stresses and the loading. The advantage of this simplification is the existing numerical solution for the calculation of the fracture toughness for a bimaterial notched beam subjected to a bending moment.[35] The fracture stresses and fracture toughnesses of the TiN film determined are depicted in Fig.D.9 as a function of the cantilever substrate thickness.

D.4 Discussion

The method presented allows a straightforward, local and reliable determination of fracture toughness and fracture stress of ceramic thin films owing to the defined stress state in the region of interest resulting from the sample and loading geometry. As a prerequisite, it is important to evaluate the depth profile of residual stresses in the coating prior to the actual fracture experiments either by means of the ILR method[15] like in this paper or by other techniques based on Raman spectroscopy[36–39] or grazing incidence X-ray diffraction.[40–43] In case of pronounced stress gradients, the simple determination of the average stresses could lead to an over- or underestimation of the stresses in the region of interest, which would result in wrong values for the strength or toughness calculated.

The method can be applied to a wide range of thin film/substrate material combina-

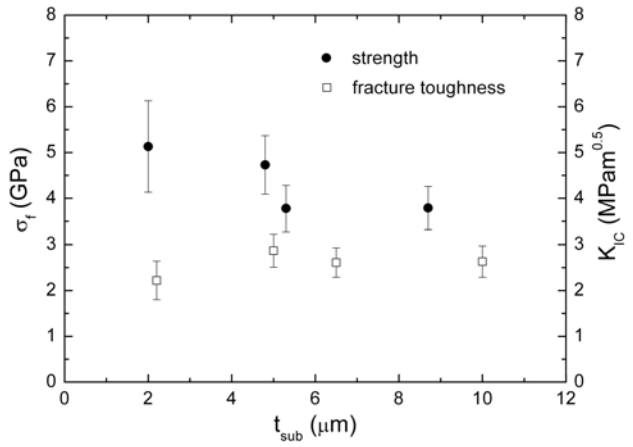

Figure D.9: Strength and fracture toughness of the TiN film as a function of substrate thickness.

tions, but it has to be taken into account that in case of plastic deformation occurring during the experiment, the determination of the fracture mechanical parameters will become more complex and may need to involve finite elements simulations. If possible, materials sensitive to ion damage should not be investigated with a FIB operated with an acceleration voltage of $30kV$ as presented here. Instead, the FIB ought to be operated with lower acceleration voltage or ion energies, respectively. The implantation depth of the accelerated ions can be estimated by performing a SRIM (the Stopping and Range of Ions in Matter[44]) simulation. Materials like Aluminium, for example, that exhibit pronounced Ga-induced grain boundary embrittlement, should not be investigated in a Ga-operated FIB.

The average fracture toughness and strength determined are $2.8 \pm 0.3MPa\sqrt{m}$ and $4.4 \pm 0.7GPa$, respectively. The uniformity of the results shows that the cantilever substrate thickness and therefore the depth profile of residual stresses in the curved cantilever does not influence these values. The stresses in the region of interest -at the surface or in front of the FIB-fabricated notch, respectively- depend solely on the superposition of the intrinsic stresses in the curved cantilever and the stresses induced by the loading, as it is expected according to basic mechanics. Furthermore, the cantilevers tested are located on the same specimen and exhibit therefore the same microstructure, which can influence the fracture behaviour significantly.[12] On one hand, the independence of the values determined on the stress distribution in the TiN film clearly indicates that the fracture properties of the film itself are not affected by the residual stresses, but rather by the strength and fracture toughness of the grains and the grain boundaries, which depends mainly on the deposition process and parameters. On the other hand, residual stresses are definitely important for the structural integrity of coated components because high compressive stresses hinder crack nucleation and propagation in the coating, even if the resistance against fracture of the thin film itself is low. Therefore, the most important task is to produce films which exhibit high compressive residual stresses, good fracture properties and sufficient adhesion to the substrate material in order to prevent failure.

A challenging task is the comparison with results obtained by other research groups because almost no report is found in literature to compare the fracture toughness and

strength with. Kamiya et al[8,45] investigated the fracture mechanical parameters of $4\mu m$ and $7\mu m$ thick PVD-deposited TiN films deposited on WC-Co cutting inserts by means of a combination of micro fracture tests and simulations. The critical energy release rates were between $21.2J/m^2$ for the $4\mu m$ and $16.4J/m^2$ for the $7\mu m$ thick film, which corresponds to critical stress intensity factors of $2.7MPa\sqrt{m}$ and $2.3MPa\sqrt{m}$, respectively, considering plane strain state in front of the crack tip, the Young's modulus of TiN used for the ILR method ($E_{TiN} = E_{TiN,biax}\,(1 - \nu_{TiN}) = 309GPa$) and Eq. (D.1).

$$K_c = \sqrt{\frac{E \cdot G_c}{1 - \nu^2}} \tag{D.1}$$

Although the experimental setup, the substrate material, and the deposition conditions were different, both values determined by Kamiya et al[45] correspond well to the mode I fracture toughness of $2.8 \pm 0.3MPa\sqrt{m}$ presented here.

Kamiya et al[8] furthermore evaluated the strengths of free standing thin film cantilevers of approximately $100\mu m$ length and $50\mu m$ width by bending the cantilever beams by means of a loading device and measuring the load at fracture. In case of bending the cantilever downwards, the crack initiates near the surface, similar to the experiment presented here. Nevertheless, the strength of the TiN film obtained by means of that method was $2.6GPa$, which is significantly lower than the result determined in this paper ($\sigma_f = 4.4 \pm 0.7GPa$). It has to be mentioned that Kamiya et al[8] analyzed the strength of the brittle film using the well known Weibull distribution in order to account for the cantilever size and the possibility of flaws of critical size being located in the cantilever beam owing to the deposition process. Qin et al[46] investigated the strength of $2\mu m$ thick multi-arc ion plated TiN films on steel by straining the substrate and calculating the film stress by means of X-ray diffraction. The fracture strength determined was $7.01GPa$, which is significantly higher than the result presented here of $4.4 \pm 0.7GPa$. The comparison of the strength of the ion-plated coatings[8,45,46] and the magnetron-sputtered TiN film investigated in this paper shows that the values scatter significantly, presumably as a result of the deposition techniques and parameters.

More information about the initiation and propagation of the cracks in the TiN film is obtained by analyzing the stresses in the cantilevers and the fracture surfaces. For this purpose, the cantilever beams without pre-cracks used for the determination of the film strength are investigated in detail because the stresses are more defined than in case of the notched specimens and the crack initiation process can be discussed. The first issue to be analyzed is whether the crack initiates at the surface of the cantilever, where the stresses are highest in the TiN film, or at the interface in the Si, where the tensile stresses in the substrate are highest. Another location of the starting point of the crack in the thin film is very unlikely owing to the pronounced stress gradient induced by the loading with the indenter. Anyway, the investigation of the stresses just before fracture shows that all cantilevers fail at similar film stresses at the surface ($\sigma_f = 4.4 \pm 0.7GPa$), which corresponds to different maximum substrate stresses ($\sigma_{Si,max} = 1.8GPa$, $\sigma_{Si,min} = 0.8GPa$) owing to the variation in cantilever substrate thicknesses ($t_{sub,max} = 8.7\mu m$, $t_{sub,min} = 2\mu m$) and leads to the conclusion that the cracks presumably origin at the surface. For comparison, the stress profiles of two loaded cantilevers of different substrate thicknesses are depicted in Fig.D.10.

A critical flaw size of $a_c = 108nm$, which is somewhat larger than the width of the

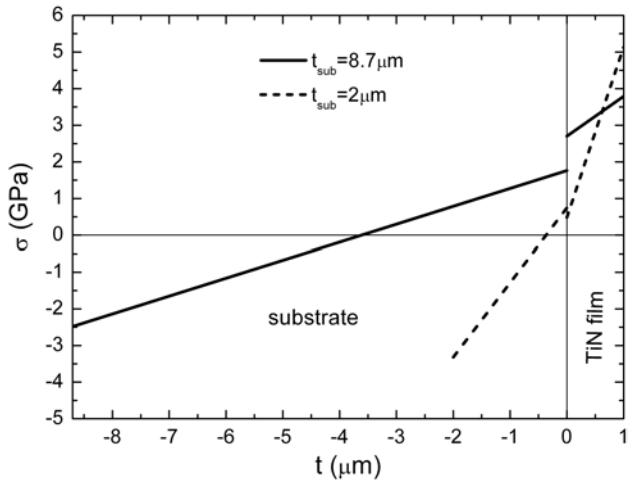

Figure D.10: Stress profiles just before fracture in two cantilevers (1 and 7) without pre-crack of different substrate thickness. These depth profiles develop by superimposing the intrinsic residual stresses and the stresses induced by the loading.

columnar grains, was roughly estimated by applying the well known Griffith's criterion (Eq.(D.2)) considering the mode I stress intensity factor and the strength of the TiN film determined in this paper.

$$a_c = \frac{1}{\pi}\left(\frac{K_{IC}}{\sigma_f}\right)^2 \tag{D.2}$$

The SEM images of the fracture surface show that intergranular cleavage is the dominant fracture mechanism of the film, which has also been reported for other TiN coatings by other research groups.[1–4,12] An example of the fracture surface of the TiN film investigated is depicted in Fig.D.11.

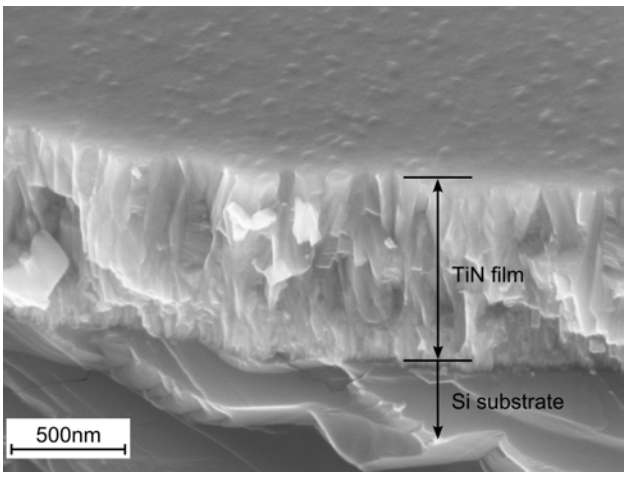

Figure D.11: SEM image of a fracture surface of the TiN film investigated shows mainly intergranular fracture (inclined view).

The results obtained demonstrate that the TiN thin film can sustain significant tensile

stresses, which disagrees with the assumption that the compressive stresses in the coating are the most important point to assure the integrity of the system.[4,12,13] Owing to the observed intergranular fracture, the strength measured is actually the strength of the grain boundaries. The combination of relatively high fracture toughness, high strength, compressive stresses in the TiN film on the substrate and sufficient adhesion is responsible for the good mechanical performance of the system investigated. However, it has to be taken into account that the quality (defect density, homogeneity, etc.) and the properties of a film depend strongly on the fabrication process and the deposition parameters and that therefore, it is difficult to draw conclusions about TiN films in general.

D.5 Conclusion

The results demonstrate that the method presented is a powerful tool for the determination of the mode I fracture toughness and the intrinsic strength of thin films. The defined stress state in the region of interest during loading and the straightforward calculation procedure lead to reliable and reproducible results as shown by means of the PVD-deposited TiN film on single crystalline Si. The fracture toughness of $2.8 \pm 0.3 MPa\sqrt{m}$ corresponds well to results obtained by Kamiya et al.[45] The strength of $\sigma_f = 4.4 \pm 0.7 GPa$ is surprisingly high, although values up to $7.01 GPa$ have been reported for PVD-deposited TiN films.[46] SEM images reveal that intergranular cleavage is the dominant fracture mechanism. These results lead to the conclusion that the structural integrity of the film results mainly from the high grain boundary strength rather than solely from high compressive stresses.

D.6 Acknowledgements

The authors thank the Austrian Science Foundation FWF for supporting this work and M. Swain, K.J. Martinschitz and H. Köstenbauer for helpful discussions.

Bibliography to paper D

[1] Weppelmann E, Swain MV. Thin Solid Films 1996;286:111.

[2] Ma LW, Cairney JM, Hoffman M, Munroe PR. Surf Coat Technol 2005;192:11.

[3] Bhowmick S, Xie ZH, Hoffman M, Jayaram V, Biswas SK. J Mater Res 2004;19:2616.

[4] Xie ZH, Hoffman M, Moon RJ, Munroe PR. J Mater Res 2006;21:437.

[5] Xie ZH, Hoffman M, Munroe P, Singh R, Benadavid A, Martin PJ. J Mater Res 2007;22:2312.

[6] Kim KH, Han D-S, Kim SK. Surf Coat Technol 2003;163-164:605.

[7] Ichimura H, Ishii Y. Surf Coat Technol 2003;165:1.

[8] Kamiya S, Hanyu H, Amaki S, Yanase H. Surf Coat Technol 2007;202:1154.

[9] Jaeger G, Endler I, Heilmaier M, Bartsch K, Leonhardt A. Thin Solid Films 2000;377-378;382.

[10] Zhang TY, Su YJ, Qian CF, Zhao MH, Chen LQ. Acta Mater 2000;48:2843.

[11] Jonnalagadda K, Cho SW, Chasiotis I, Friedmann T, Sullivan J. J Mech Phys Solids 2008;56:388.

[12] Bhowmick S, Jayaram V, Biswas Sk. Acta Mater 2005;53:2459.

[13] Jayaram V, Bhowmick S, Xie ZH, Math S, Hoffman M, Biswas SK. Mater Sci Eng A 2006;423:8.

[14] Kstenbauer H, Fontalvo GA, Kapp M, Keckes J, Mitterer C. Surf Coat Technol 2007;201:4777.

[15] Massl S, Keckes J, Pippan R. Acta Mater 2007;55:4835.

[16] Freund LB, Suresh S, Thin film materials, Cambridge: Cambridge University Press; 2003, p. 244.

[17] Mendibide C, Steyer P, Esnouf C, Goudenau P, Thiaudiere D, Gailhanou M, Fontane J. Surf Coat Technol 2005;200:165.

[18] Kitamura T, Hirakata H, Itsuji T. Eng Fract Mech 2003;70:2089.

[19] An J, Zhang QY. Surf Coat Technol 2005;200:2451.

[20] Barshilia HC, Deepthi B, Prabhu ASA, Rajam KS. Surf Coat Technol 2006;201:329.

[21] Bedell SW, Reznicek A, Fogel K, Ott J, Sadana DK. Mater Sci Semicon Proc 2006;9:423.

[22] Carlotti G, Doucet L, Dupeux M. Thin Solid Films 1997;296:102.

[23] Novotna Z, Kralova R, Novak R, Marek J. Surf Coat Technol 1999;116-119:424.

[24] Comins JD, Pang W, Every AG, Pietersen D. Refract Met Hard Mater 1998;16:389.

[25] Haider J, Rahman M, Corcoran B, Hashmi MSJ. Mater Proc Technol 2005;168:36.

[26] Bamber MJ, Cooke KE, Mann AB, Derby B. Thin Solid Films 2001;398-399:299.

[27] Kim SH. Mater Lett 2007;16:3589.

[28] Huang Z, Leighton G, Wright R, Duval F, Chung HC, Kirby P, Whatmore RW. Sens Actuators A 2007;135:660.

[29] Zhang J. J Mater Proc Technol 2002;123:329.

[30] Antunes JM, Fernandes JV, Sakharova NA, Oliveira MC, Menezes LF. Int J Solids Struct 2007;44:8313.

[31] Tran MD, Poublan J, Dautzenberg JH. Thin Solid Films 1997;308-309:310.

[32] Eiper E, Martinschitz KJ, Keckes J. Powder Diffr 2006;21:25.

[33] Resnik D, Aljancic U, Vrtacnik D, Mozek M, Amon S. Vacuum 2005;80:236.

[34] Dieing T, Usher BF. Phys Rev B 2003;67:054108.

[35] Murakami Y. Stress Intensity Factors Handbook Vol 4. Oxford: Pergamon Press; 2001. pp. 111.

[36] Grabner L. J Appl Phys 1978;49:580.

[37] Dietrich B, Dombrowski KF. J Raman Spectr 1999;30:893.

[38] De Wolf I. J Raman Spectr 1999;30:877.

[39] Atkinson A, Jain SC. J Raman Spectr 1999;30:885.

[40] Genzel C. Mater Sci and Technol 2005;21:10.

[41] Marques MJ, Pina J, Dias AM, Lebrun JL, Feugeas J. Surf Coat Technol 2005;195:8.

[42] Ma CH, Huang JH, Chen H. Thin Solid Films 2002;418:73.

[43] Noyan IC, Cohen JB. Residual Stress. New York: Springer; 1987.

[44] Ziegler JF, Biersack JP, Littmark U. The Stopping Range of Ions in Matter. New York: Pergamon Press;1985, pp. 321.

[45] Kamiya S, Nagasawa H, Yamanobe K, Saka M. Thin Solid Film 2005;473:123.

[46] Qin M, Ju DY, Wu YN, Sun C, Li JB. Mater Charact 2006;56:208.

E

Mechanics of Residually Stressed Coated Systems: Derivation of Basic Equations

S. Massl[a], J. Keckes[b] and R. Pippan[a]

[a] Erich Schmid Institute of Materials Science, Austrian Academy of Sciences, A–8700 Leoben, Austria
[b] Department Materials Physics, University of Leoben, A–8700 Leoben, Austria

Abstract

The basic mechanical equations necessary for the description of depth profiles of residual stresses in coated systems and for the calculation procedure of the ion beam layer removal method developed are derived. Here, the stresses are assumed to originate from the difference of the coefficients of thermal expansion of the substrate and the thin film subjected to a temperature difference $\Delta T \neq 0$. A sign convention is introduced in order to assure a uniform description of residually stressed systems. Finally, the stress profile of an arbitrary model system subjected to a temperature difference of $\Delta T = 300K$ is calculated and compared with Stoney's equation. The most important equations are highlighted.

E.1 The Basic Idea

For the derivations and calculations following assumptions are made:

- The stresses result from the difference of the thermal expansion coefficients,
- only the biaxial Young's moduli ($E_{biax} = E_{bulk}/(1-\nu)$) are used owing to the 2D calculation of a 3D problem,
- edge effects are not taken into account,
- the material is considered to be ideal elastic and
- the adhesion of the film on the substrate is perfect.

To calculate the stress in a bilayer with different coefficients of thermal expansion exposed to a temperature difference, a thought experiment is carried out (Fig.E.1):

1. The thin film and the substrate are separated. At $\Delta T = 0K$ they have the same length (Fig.E.1 (a)).
2. By applying a temperature difference $\Delta T > 0$, both materials expand. Owing to the different coefficients of thermal expansion α, they now have different lengths (Fig.E.1 (b)).
3. External normal forces F_1 and F_2, or tensions σ_1 and σ_1, respectively, act at the ends of the layer and the substrate to compensate for the difference in length (Fig.E.1 (c)).
4. Layer and substrate are joined and the external forces are removed, which leads to a certain curvature of the residually stressed system (Fig.E.1 (d)).

E.2 Sign Convention

A sign convention is introduced in order to obtain a uniform description of the system (Fig.E.2). According to this convention, the radius ρ can have a positive or negative sign, depending on the curvature. For the calculation, we assume that $\Delta T = 0$ and that the system is subjected to a bending moment.

Calculation of the perimeter p of a circle with radius ρ:

$$p = 2\rho\pi \tag{E.1}$$

Now the perimeter p_ϵ of an expanded or contracted circle with radius $\rho - y$ is calculated. In the bilayer curvature model, y is the distance of a point in the material from the neutral axis.

$$p_\epsilon = 2\,(\rho - y)\,\pi \tag{E.2}$$

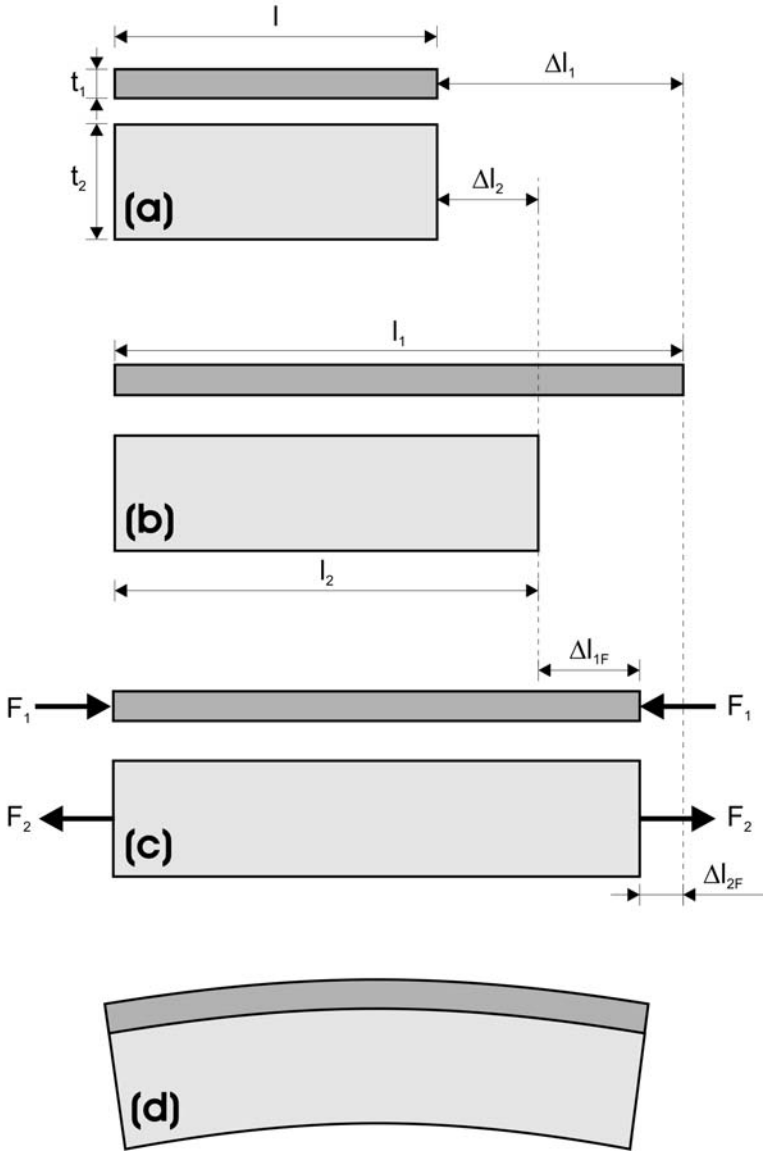

Figure E.1: Initially, the layer and substrate have the same length at $\Delta T = 0$ (a). When the temperature is raised, the separated parts expand owing to their coefficients of thermal expansion (b). Now, external forces F_1 and F_2 are applied to compensate for the difference in length (c). Finally, the film and the substrate are joined and the external forces are removed. The residually stressed system now exhibits a certain curvature (d).

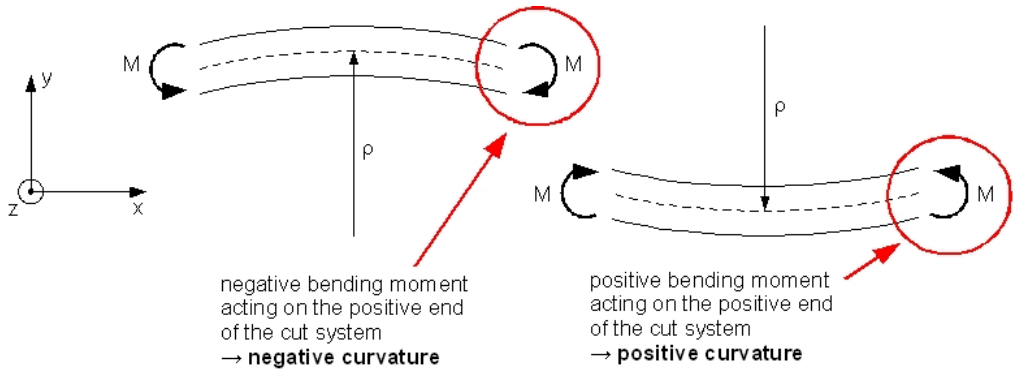

Figure E.2: Introduced sign convention: The end where the x-axis leaves the cut system (in this case the right end) is defined as positive. The end where the x-axis enters the system is defined as negative. A negative bending moment on the positive end creates a negative curvature (bending radius respectively), a positive bending moment on the positive end creates a positive curvature. A positive bending moment on the negative end creates a negative curvature, a negative bending moment on the negative end creates a positive curvature

With

$$\epsilon = \frac{\Delta l}{l} \tag{E.3}$$

the strain as a function of the curvature and the distance from the neutral plane is calculated:

$$\epsilon = \frac{p_\epsilon - p}{p} = \frac{2\left(\rho - y\right)\pi - 2\rho\pi}{2\rho\pi} = \frac{2\rho\pi - 2y\pi - 2\rho\pi}{2\rho\pi} = -\frac{2y\pi}{2\rho\pi} = -\frac{y}{\rho} = -\kappa y \tag{E.4}$$

$$\sigma = E\epsilon \tag{E.5}$$

With Eq. (E.4), Hookes Law (Eq. (E.5)) can be written as

$$\boxed{\sigma = -E\kappa y.} \tag{E.6}$$

E.3 Force Balance

Since the system is in a state of equilibrium, both forces F_1 and F_2 have the same magnitude but opposite signs (Fig.E.3). Otherwise, the system would drift in one direction.

$$F_1 + F_2 = 0 \tag{E.7}$$

$$F_2 = -F_1 = F \tag{E.8}$$

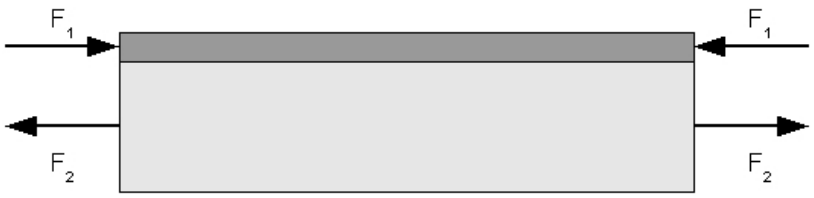

Figure E.3: Axial forces or the corresponding bending moments, respectively, establish the equilibrium of the system, compensate for the difference in length and straighten the system.

E.4 Calculation of the Normal Stresses in the Substrate and the Coating

The force $F = -F_1 = F_2$ compensates for the difference in length of the layer and the substrate. Calculation of the strains ϵ_1 and ϵ_2 owing to thermal expansion ΔT:

$$\epsilon_1 = \frac{\Delta l_1}{l} = \alpha_1 \Delta T \tag{E.9}$$

$$\epsilon_2 = \frac{\Delta l_2}{l} = \alpha_2 \Delta T \tag{E.10}$$

Calculation of the strains ϵ_{1F} and ϵ_{2F} owing to to the applied forces F_1 and F_2:

$$\epsilon_{1F} = \frac{\sigma_1}{E_1} = \frac{\Delta l_{1F}}{l + \Delta l_1} \tag{E.11}$$

$$\epsilon_{2F} = \frac{\sigma_2}{E_2} = \frac{\Delta l_{2F}}{l + \Delta l_2} \tag{E.12}$$

$$A_1 = bt_1 \tag{E.13}$$

$$A_2 = bt_2 \tag{E.14}$$

$$\sigma_1 = \frac{F_1}{A_1} = -\frac{F}{A_1} = -\frac{F}{t_1 b} \tag{E.15}$$

$$\sigma_2 = \frac{F_2}{A_2} = \frac{F}{A_2} = \frac{F}{t_2 b} \tag{E.16}$$

Calculation of the lengths l_1 and l_2 of the coating and the substrate subjected to ΔT:

$$l_1 = l + \Delta l_1 = l + \epsilon_1 \cdot l = l\,(1 + \epsilon_1) \tag{E.17}$$

$$l_2 = l + \Delta l_2 = l + \epsilon_2 \cdot l = l\,(1 + \epsilon_2) \tag{E.18}$$

Now the difference in length is compensated by applying F_1 and F_2 which leads to the strains ϵ_{1F} and ϵ_{2F}.

$$\Delta l_1 - \epsilon_{1F} \cdot l_1 = \Delta l_2 + \epsilon_{F2} \cdot l_2 \tag{E.19}$$

$$\alpha_1 \cdot \Delta T \cdot l + \frac{\sigma_1}{E_1} l_1 = \alpha_2 \cdot \Delta T \cdot l + \frac{\sigma_2}{E_2} l_2 \tag{E.20}$$

$$\alpha_1 \cdot \Delta T \cdot l - \frac{F}{A_1 E_1} l_1 = \alpha_2 \cdot \Delta T \cdot l + \frac{F}{A_2 E_2} l_2 \tag{E.21}$$

$$\alpha_1 \cdot \Delta T - \frac{F}{A_1 E_1} l\,(1 + \epsilon_1) = \alpha_2 \cdot \Delta T + \frac{F}{A_2 E_2} l\,(1 + \epsilon_2) \tag{E.22}$$

$$\alpha_1 \cdot \Delta T - \frac{F}{A_1 E_1} l\,(1 + \alpha_1 \cdot \Delta T) = \alpha_2 \cdot \Delta T + \frac{F}{A_2 E_2} l\,(1 + \alpha_2 \cdot \Delta T) \tag{E.23}$$

$$\Delta T\,(\alpha_1 - \alpha_2) = F \cdot \left(\frac{1 + \alpha_1 \Delta T}{A_1 E_1} + \frac{1 + \alpha_2 \Delta T}{A_2 E_2} \right) \tag{E.24}$$

The force F can be calculated from the temperature difference, the dimensions (thicknesses t_1 and t_2 and width b) of the specimen and the material parameters:

$$\boxed{F = \frac{\Delta T\,(\alpha_1 - \alpha_2)}{\left(\frac{1+\alpha_1 \Delta T}{b t_1 E_1} + \frac{1+\alpha_2 \Delta T}{b t_2 E_2} \right)}} \tag{E.25}$$

E.5 Determination of the Position of the Neutral Axis

The neutral axis passes through the cross-sectional area where the resulting stress from the bending moment is zero (Fig.E.4). When the coating is much thinner than the substrate and the Young's moduli are of the same order of magnitude, the neutral axis is located in the substrate.

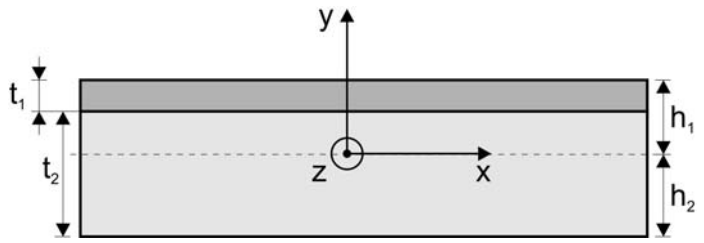

Figure E.4: Location of the neutral axis (dashed line) and the coordinate system.

To calculate the position of the neutral axis, we assume that $\Delta T = 0K$ and the system is bent by an external bending moment M_{curv}. At the neutral axis the force $F_{M_{curv}}$ and therefore the stress $\sigma_{M_{curv}}$ due to the bending moment M_{curv} is zero:

$$\boxed{\int \sigma_{M_{curv}} dA = 0} \tag{E.26}$$

For our system consisting of two materials we obtain the equation

$$\int_1 \sigma_{M_{curv}1} dA_1 + \int_2 \sigma_{M_{curv}2} dA_2 = 0. \tag{E.27}$$

With Eq. (E.6), Eq. (E.27) can be written as

$$-\int_1 E_1 \kappa y dA_1 - \int_2 E_2 \kappa y dA_2 = 0. \tag{E.28}$$

$$\boxed{E_1 \int_1 y dA_1 + E_2 \int_2 y dA_2 = 0} \tag{E.29}$$

Geometric condition for the position of the neutral axis:

$$h_1 + h_2 = t_1 + t_2 \tag{E.30}$$

$$h_2 = t_1 + t_2 - h_1 \tag{E.31}$$

Calculation of the first integral of Eq. (E.29):

$$E_1 \int_1 y dA_1 = E_1 \int_{y=h_1-t_1}^{h_1} \int_{z=0}^{b} y dy dz = E_1 \frac{b}{2} \left[h_1^2 - (h_1 - t_1)^2 \right] = \tag{E.32}$$

$$= E_1 \frac{b}{2} \left(h_1^2 - h_1^2 + 2t_1 h_1 - t_1^2 \right) = E_1 \frac{b}{2} \left(2t_1 h_1 - t_1^2 \right)$$

Calculation of the second integral of Eq. (E.29):

$$E_2 \int_2 y dA_2 = E_2 \int_{y=-h_2}^{h_1-t_1} \int_{z=0}^{b} y dy dz = E_2 \frac{b}{2} \left(h_1^2 - 2h_1 t_1 + t_1^2 - h_2^2 \right) \tag{E.33}$$

Substitution h_2 in the second integral of Eq. (E.29):

$$h_2^2 = (t_1 + t_2 - h_1)^2 = t_1^2 + 2t_1 t_2 - 2t_1 h_1 - 2t_2 h_1 + h_1^2 + t_2^2 \tag{E.34}$$

$$E_2 \int_2 y dA_2 = E_2 \frac{b}{2} \left(h_1^2 - 2h_1 t_1 + t_1^2 - t_1^2 - 2t_1 t_2 + 2t_1 h_1 + 2t_2 h_1 - h_1^2 - t_2^2 \right) = \tag{E.35}$$

$$= E_2 \frac{b}{2} \left(2t_2 h_1 - 2t_1 t_2 - t_2^2 \right)$$

Addition of the solutions for the two integrals of Eq. (E.29) allows the calculation of h_1:

$$E_1 \frac{b}{2}\left(2t_1h_1 - t_1^2\right) + E_2 \frac{b}{2}\left(2t_2h_1 - 2t_1t_2 - t_2^2\right) = 0 \tag{E.36}$$

$$2E_1t_1h_1 - E_1t_1^2 + 2E_2t_2h_1 - 2E_2t_1t_2 - E_2t_2^2 = 0 \tag{E.37}$$

$$h_1\left(2E_1t_1 + 2E_2t_2\right) = E_1t_1^2 + 2E_2t_1t_2 + E_2t_2^2 \tag{E.38}$$

$$\boxed{h_1 = \frac{E_1t_1^2 + 2E_2t_1t_2 + E_2t_2^2}{2E_1t_1 + 2E_2t_2}} \tag{E.39}$$

Now h_2 is calculated:

$$h_2 = \frac{t_1\left(2E_1t_1 + 2E_2t_2\right) + t_2\left(2E_1t_1 + 2E_2t_2\right) - E_1t_1^2 - 2E_2t_1t_2 - E_2t_2^2}{2E_1t_1 + 2E_2t_2} \tag{E.40}$$

$$\boxed{h_2 = \frac{E_1t_1^2 + 2E_1t_1t_2 + E_2t_2^2}{2E_1t_1 + 2E_2t_2}} \tag{E.41}$$

The expressions for h_1 and h_2 only depend on the material parameters and are therefore independent of the loading.

E.6 Moment Balance

Now we assume that the neutral axis is located in the substrate as it is usually the case in thin film/substrate systems. Anyway, the equations can be used for the calculation of the moment balance of any system. As depicted in Fig.E.5 the cross section of the system is divided into 3 parts:

1. The film which is located above the neutral axis (**af**),
2. the part of the substrate which is located above the neutral axis (**as**) and
3. the part of the substrate which is located below the neutral axis (**b**).

Part 2 (**as**) and 3 (**b**) can be calculated in one step, but the separate calculation below where the substrate is divided into 2 parts makes it easier to understand in which direction the single bending moments act.

According to the second equation of statics the moment resultant of the normal stresses acting over the cross section is equal to the bending moment M.

$$\boxed{M = -\int_A \sigma_x y dA} \tag{E.42}$$

Calculation of the bending moment **above** the neutral axis in the **film** M_{af}:

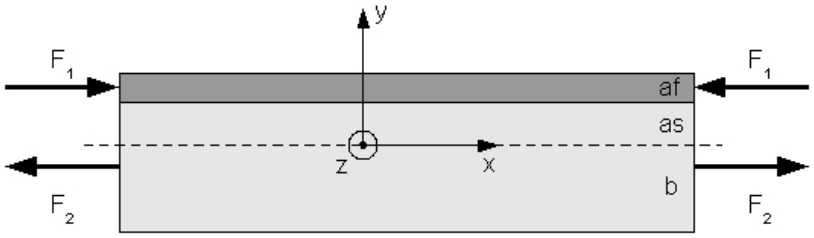

Figure E.5: Forces or the corresponding bending moments, respectively, act on the specimen due to thermal expansion to obtain an equilibrated straightened system. The dashed line represents the neutral axis.

$$M_{af} = -\int_{y=h_1-t1}^{h_1}\int_{z=0}^{b}\sigma_1 y dy dz = \int_{y=h_1-t1}^{h_1}\int_{z=0}^{b}\frac{F}{t_1 b}y dy dz = \tag{E.43}$$

$$= \frac{F}{t_1}\int_{y=h_1-t1}^{h_1} y dy = \frac{F}{t_1}\left(h_1 t_1 - \frac{t_1^2}{2}\right)$$

Calculation of the bending moment **above** the neutral axis in the **substrate** M_{as}:

$$M_{as} = -\int_{y=0}^{h_1-t1}\int_{z=0}^{b}\sigma_2 y dy dz = -\int_{y=0}^{h_1-t1}\int_{z=0}^{b}\frac{F}{(h_1-t_1)\,b}y dy dz = \tag{E.44}$$

$$= -\frac{F}{h_1-t_1}\int_{y=0}^{h_1-t_1} y dy = -\frac{1}{2}F\,(h_1-t_1)$$

Calculation of the resulting bending moment **above** the neutral axis M_a:

$$M_a = M_{af} + M_{as} = \frac{F}{t_1}\left(h_1 t_1 - \frac{t_1^2}{2}\right) - \frac{1}{2}F\,(h_1-t_1) = \tag{E.45}$$

$$= Fh_1 - \frac{1}{2}Ft_1 - \frac{1}{2}Fh_1 + \frac{1}{2}Ft_1 = \frac{1}{2}Fh_1$$

Calculation of the bending moment **below** the neutral axis in the substrate M_b:

$$M_b = -\int_{y=-h_2}^{0}\int_{z=0}^{b}\sigma_2 y dy dz = -\int_{y=-h_2}^{0}\int_{z=0}^{b}\frac{F}{h_2 b}y dy dz = \tag{E.46}$$

$$= -\frac{F}{h_2}\int_{y=-h_2}^{0} y dy = \frac{1}{2}Fh_2$$

Calculation of the resulting bending moment M due to the forces F_1 and F_2:

$$M = M_a + M_b = \frac{1}{2}Fh_1 + \frac{1}{2}Fh_2 = \frac{1}{2}F\,(h_1+h_2) \tag{E.47}$$

With Eq. (E.30), the result of Eq. (E.47) can be written as

$$\boxed{M = \frac{1}{2} F \left(t_1 + t_2\right).} \tag{E.48}$$

The calculated bending moment M is applied in order to straighten the residually stressed system. Since it depends on the axial force F, it also depends on the temperature difference ΔT. When the bending moment M is removed, the system relaxes and exhibits a certain curvature. The same curvature can be obtained if a bending moment $M_{curv} = -M$ is added to the bending moment M.

$$\boxed{M_{curv} = -\frac{1}{2} F \left(t_1 + t_2\right)} \tag{E.49}$$

E

E.7 Calculating the Curvature of a Bimaterial System Subjected to a Temperature Difference ΔT

The curvature as a function of the temperature difference, the dimensions, the elastic constants and the coefficients of thermal expansion is calculated as follows:

$$M_{curv} = -\int_A \sigma_x y dA = \int_{A_{af}} \sigma_{x1} y dA_{af} - \int_{A_{as}} \sigma_{x2} y dA_{as} - \int_{A_b} \sigma_{x2} y dA_b = \tag{E.50}$$

With Eq. (E.6), Eq. (E.50) can be written as:

$$= \kappa E_1 \int_{A_{af}} y^2 dA_{af} + \kappa E_2 \int_{A_{as}} y^2 dA_{as} + \kappa E_2 \int_{A_b} y^2 dA_b =$$

$$= \kappa E_1 \int_{y=h_1-t1}^{h_1} \int_{z=0}^{b} y^2 dy dz + \kappa E_2 \int_{y=0}^{h_1-t_1} \int_{z=0}^{b} y^2 dy dz + \kappa E_2 \int_{y=-h_2}^{0} \int_{z=0}^{b} y^2 dy dz =$$

$$= \kappa b E_1 \int_{y=h_1-t1}^{h_1} y^2 dy dz + \kappa b E_2 \int_{y=0}^{h_1-t_1} y^2 dy dz + \kappa b E_2 \int_{y=-h_2}^{0} y^2 dy dz =$$

$$= \frac{1}{3} \kappa b E_1 t_1 \left(3h_1^2 - 3h_1 t_1 - t_1^2\right) + \frac{1}{3} \kappa b E_2 \left(h_1 - t_1\right)^3 + \frac{1}{3} \kappa b E_2 h2^3 =$$

$$= \frac{1}{3} \kappa b \left[E_1 t_1 \left(3h_1^2 - 3h_1 t_1 + t_1^2\right) + E_2 \left(h_1 - t_1\right)^3 + E_2 \left(t_1 + t_2 - h_1\right)^3\right] \tag{E.51}$$

$$M_{curv} = -\frac{1}{2} F \left(t_1 + t_2\right) = \tag{E.52}$$

$$= \frac{1}{3} \kappa b \left[E_1 t_1 \left(3h_1^2 - 3h_1 t_1 + t_1^2\right) + E_2 \left(h_1 - t_1\right)^3 + E_2 \left(t_1 + t_2 - h_1\right)^3\right]$$

The curvature radius depends on the force F:

$$\rho = -\frac{\frac{2}{3}b\left[E_1 t_1\left(3h_1^2 - 3h_1 t_1 + t_1^2\right) + E_2\left(h_1 - t_1\right)^3 + E_2\left(t_1 + t_2 - h_1\right)^3\right]}{F\left(t_1 + t_2\right)} \tag{E.53}$$

$$\rho = -\frac{2b\left[E_1 t_1\left(3h_1^2 - 3h_1 t_1 + t_1^2\right) + E_2\left(h_1 - t_1\right)^3 + E_2\left(t_1 + t_2 - h_1\right)^3\right]}{3\Delta T\left(\alpha_1 - \alpha_2\right)\left(t_1 + t_2\right)} \cdot \cdot \left(\frac{1 + \alpha_1 \Delta T}{A_1 E_1} + \frac{1 + \alpha_2 \Delta T}{A_2 E_2}\right) \tag{E.54}$$

The curvature radius is given as

$$\rho = -\frac{2\left[E_1 t_1\left(3h_1^2 - 3h_1 t_1 + t_1^2\right) + E_2\left(h_1 - t_1\right)^3 + E_2\left(t_1 + t_2 - h_1\right)^3\right]}{3\Delta T\left(\alpha_1 - \alpha_2\right)\left(t_1 + t_2\right)} \cdot \cdot \left(\frac{1 + \alpha_1 \Delta T}{t_1 E_1} + \frac{1 + \alpha_2 \Delta T}{t_2 E_2}\right) \tag{E.55}$$

E.8 Correlation of the Stresses in the Straightened and the Relaxed System

Stresses which arise from different coefficients of thermal expansion in the substrate and coating consist of two parts:

- stresses due to the normal forces F_1 and F_2 and
- stresses due to the bending moment M.

The stresses which arise from the normal forces F_1 and F_2 – necessary to compensate for the difference in length of the coating and the substrate – are calculated as follows. The stress distribution is depicted in Fig.E.6.

$$\sigma_{F1} = \frac{F_1}{b \cdot t1} = -\frac{F}{b \cdot t1} \tag{E.56}$$

$$\sigma_{F2} = \frac{F_2}{b \cdot t2} = \frac{F}{b \cdot t2} \tag{E.57}$$

The bending moment responsible for the curvature M_{curv} also creates a stress distribution in the material (Fig.E.7). It can be calculated from the equation

$$\sigma_{M_{curv}} = -E\kappa y$$

of from

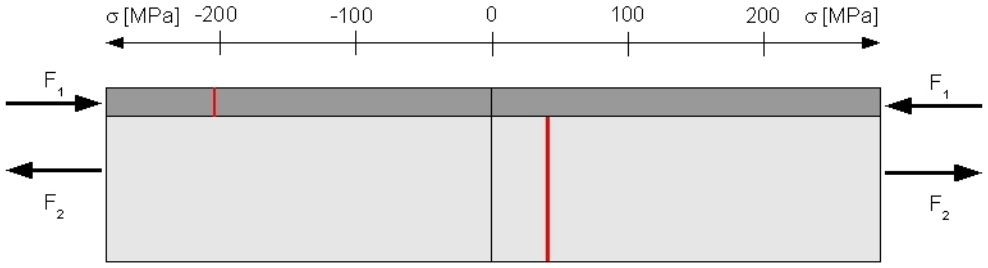

Figure E.6: Distribution of the stresses coming from the axial forces F_1 and F_2.

$$\sigma_{M_{curv}} = -E\frac{y}{\rho} \tag{E.58}$$

respectively. It has to be taken into account that $y = 0$ in the neutral axis.

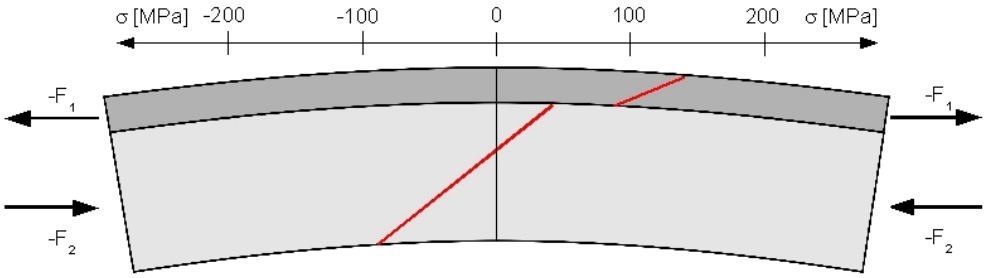

Figure E.7: Stress distribution at $\Delta T = 0$ resulting from the external stresses $-F_1$ and $-F_2$ or the bending moment M_{curv}, respectively.

For the calculation of the total stress distribution in the system the two contributing parts of the stress – σ due to F and σ due to M_{curv}– have to be added:

$$\sigma_{total,relaxed} = \sigma_F + \sigma_{M_{curv}} \tag{E.59}$$

For better understanding, we assume that the system is curved due to a certain ΔT. In the equilibrium (relaxed) state there are no external forces or bending moments acting on the system. The curvature is only produced by the temperature difference ΔT which leads to an extension or contraction of the two joined materials with different thermal expansion coefficients. If now the bending moment M is applied the system will straighten. In this straight state the stress distribution in the system must be the same as if the disjoined parts – coating and substrate – were compressed or expanded by axial forces F or stresses σ_F respectively (Fig.E.6). When the straightening bending moment M is removed or alternatively the bending moment $M_{curv} = -M$ is added, the system will obtain its equilibrium curvature. The equilibrium stress distribution $\sigma = \sigma_F - \sigma_M$ or $\sigma = \sigma_F + \sigma_{M_{curv}}$ respectively is depicted in Fig.E.8.

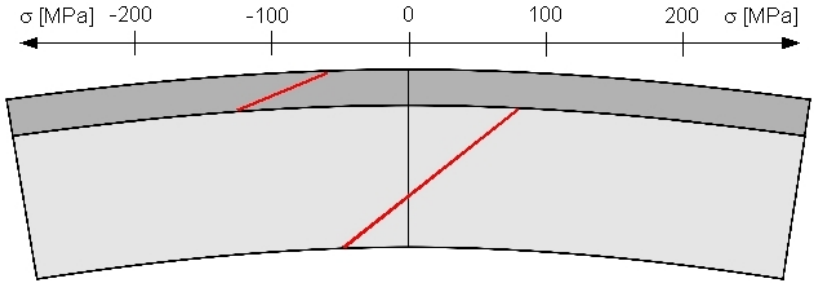

Figure E.8: Equilibrium stress distribution of the relaxed model system.

E.9 An Example: Depth Profile of Residual Stresses in an Arbitrary Model System

The values listed in table E.1 are used for the calculation of the stress distribution of the model system.

$$\begin{aligned} \alpha_1 &= 9.4 \cdot 10^{-6} K^{-1} \\ \alpha_2 &= 2.6 \cdot 10^{-6} K^{-1} \\ E_{b1} &= 800 GPa \\ E_{b2} &= 67.14 GPa \\ t_1 &= 1 \mu m \\ t_2 &= 300 \mu m \\ \Delta T &= 300 K \end{aligned}$$

Table E.1: Values used for the calculation of the stress distribution in the coating (1) and the substrate (2). E_{b1} and E_{b2} are the biaxial Youngs Moduli of the coating and the substrate.

The calculated curvature (Eq. (E.55)) is $-71.5cm$. The stress distribution (not scaled) is depicted in Fig.E.9.

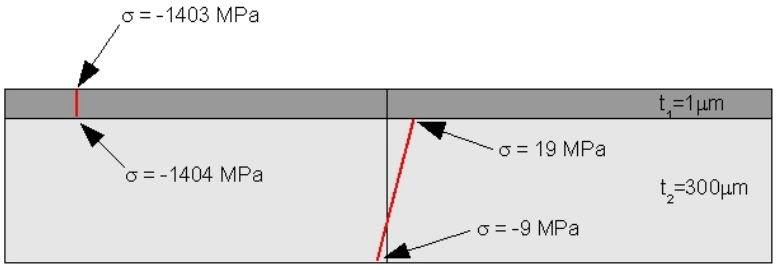

Figure E.9: Equilibrium stress distribution in the relaxed model system (not scaled). The system exhibits only very small curvature owing to the thick substrate.

E.10 Comparison of the Stresses Obtained with Stoney's Equation

Stoney's equation (Eq. (E.60)) is widely used to calculate the mean stress in the coating of a bilayer material. Nevertheless, it is only valid if the substrate is much thicker than the coating and cannot be applied to cantilevers as used in for the ILR method.

$$\boxed{\sigma_1 = \frac{\kappa E_{b2} t_2^2}{6 t_1}} \tag{E.60}$$

Finally, the mean film stress in the arbitrary model system obtained by the calculation procedure presented is compared with the film stress determined by means of Stoney's equation and listed in table E.2.

$$\begin{aligned} \kappa = &\quad -0,001398 mm^{-1} \\ \sigma_{1-derived} = &\quad -1403.46 MPa \\ \sigma_{1-Stoney} = &\quad -1407.09 MPa \end{aligned}$$

Table E.2: Comparison of the results for the films stress obtained from Stoney's equation and the equations derived in this paper.